DISSERTATION

EVALUATING L-BAND RADAR FOR THE FUTURE OF SNOW REMOTE SENSING

Submitted by

Randall Bonnell

Department of Geosciences

In partial fulfillment of the requirements

For the Degree of Doctor of Philosophy

Colorado State University

Fort Collins, Colorado

Summer 2024

Doctoral Committee:

Advisor: Daniel McGrath

Steven Fassnacht
Stephanie Kampf
Hans-Peter Marshall
Michael Ronayne

ABSTRACT

EVALUATING L-BAND RADAR FOR THE FUTURE OF SNOW REMOTE SENSING

Snowpack monitoring is essential because seasonal snowpacks provide water for billions of people, support streamflow and ecosystems, and are a fundamental component of the Earth's energy system. However, no current snowpack monitoring system is capable of measuring snow water equivalent (SWE), the most important snowpack hydrologic variable, accurately and at high spatiotemporal (<500 m, <weekly) resolutions. The primary goal of this dissertation is to evaluate a method for deriving snow density using a ground-based radar and a method for retrieving SWE from an airborne platform. In Chapter 2, I study the spatial variability of snow density by deriving relative permittivity, and thereby bulk density, from combined ground-penetrating radar (GPR) and lidar measurements of the snowpack. In Chapters 3–4, I evaluate the L-band InSAR technique for SWE retrievals, which has been considered to be a promising method for SWE retrievals for more than a decade, but has seen limited testing. I evaluate the technique using repeat InSAR acquisitions from the airborne NASA UAVSAR instrument in meadow and burned environments at Cameron Pass, Colorado (Chapter 3) and in the montane forest environment of Fraser Experimental Forest, Colorado (Chapter 4).

Snow density is a critical input variable for the retrieval of SWE from most SWE remote sensing methods. However, density is time consuming to measure in the field and is thus often measured sparsely, preventing extensive analysis of snow density models, a primary source of estimated densities for remote sensing methods. In Chapter 2, I derived >20 km of nearly continuous relative permittivity estimates, and thereby bulk density, from combined near-

coincident measurements of GPR two-way travel times and lidar snow depths at three different field sites and in both dry and wet snow conditions. Variogram analyses were conducted and revealed a 19 m median correlation length for relative permittivity and density in dry snow. For wet snow, the correlation length increased to >30 m. I then leveraged the derived densities to evaluate six snow density models to better understand the limitations of these models within lidar and radar remote sensing methods. Two models yielded densities that estimated SWE within ±10% when SWE exceeded 400 mm, but model uncertainty increased to >20% when SWE was less than 300 mm. Thus, the refinement of these density models and the development of future density models is a high priority to fully realize the potential of SWE remote sensing methods.

The L-band (1–2 GHz) InSAR technique for measuring changes in SWE (ΔSWE) is a promising method for SWE retrievals because the longer wavelength (~0.25 m) has minimal interaction with the snowpack microstructure and has increased canopy penetrative capabilities. In Chapter 3, I evaluated 10 L-band InSAR pairs collected by NASA UAVSAR near Cameron Pass, Colorado with GPR and terrestrial lidar measurements of ΔSWE in open meadows and burned forests. For single InSAR pairs, UAVSAR ΔSWE retrievals yielded an overall Pearson's correlation coefficient of 0.72–0.79, with a RMSE of 19–22 mm. I expanded the analysis beyond the locations of GPR and lidar surveys to evaluate the time series of UAVSAR SWE retrievals by including measurements of SWE from seven automated stations and found a RMSE of 42 mm. These findings support the use of this technique in unforested areas with dry snow conditions for the upcoming L-band NISAR satellite mission

Given the findings of Chapter 3 and the canopy penetration capabilities of L-band radar, I designed Chapter 4 to evaluate the influence of forest cover on the UAVSAR signal. In Chapter 4, I evaluated eight L-band InSAR pairs collected by UAVSAR over the montane forests of

Fraser Experimental Forest, Colorado with manually surveyed snow depths and snow pits and a pair of airborne lidar surveys. Compared with in situ measurements, I found that forest cover fractions <40% yielded RMSEs of ~15 mm, whereas RMSE more than doubled for forest cover fractions >50%. Further, normalized cumulative UAVSAR SWE and normalized lidar snow depths yielded identical statistical distributions for forest cover fractions <50% across the full study area, but these distributions diverged as forest cover fraction increased. Thus, forest cover fraction is a significant source of uncertainty for L-band InSAR retrievals of SWE, but this technique may be the first space-borne technique capable of retrieving SWE below non-dense forest canopy without any a priori information.

ACKNOWLEDGEMENTS

This dissertation is the culmination of two years of field work and four years of research which began during the Covid-19 pandemic. In stark contrast to the isolation caused by the pandemic, so many folks were willing to spend time encouraging me, assisting me in research, or helping me learn the subject of radar remote sensing. I am grateful and indebted to you all.

To Dan McGrath, I will never forget the day you delivered the news that we had received the NASA FINESST grant. I was incredibly shocked! Throughout our many years of working together, you have profoundly influenced the scientist I have become. You have given countless hours to my support and development, from your open-door policy to the many, many nights of grueling manuscript reviews. Beyond our professional relationship, your support of my fatherhood during this time has meant the world to me. Thank you for taking a chance on me.

Each of my committee members, HP Marshall, Steven Fassnacht, Mike Ronayne, and Stephanie Kampf, have provided valuable and insightful feedback on this dissertation. HP, thank you for your involvement, this dissertation has been significantly improved through your contributions to my radar knowledge and the opportunities for field work that you helped facilitate. Steven, thank you for providing the coursework that formed the backbone of this thesis and for our many chats over the years about snow hydrology and field observation strategies. Mike, your work with me on variograms significantly improved the quality of Chapter 2 – thank you for taking so much time to review results with me. Stephanie, thank you for providing an additional dataset for Chapter 3 and for providing substantial feedback on it.

To my many, many co-authors, thank you for your contributions, both large and small, that helped shape the chapters of this dissertation. Notably, I want to acknowledge the efforts of

Andrew Hedrick, Ernesto Trujillo, Keith Williams, Graham Sexstone, John Fulton, Jack Tarricone, and Kelly Elder. Andrew Hedrick and Ernesto Trujillo spent numerous days working with me on density modeling and provided the final iSnobal density model results for Chapter 2. Keith Williams and his team at UNAVCO Inc. collected and processed the terrestrial lidar surveys that were used in Chapters 2 and 3. John Fulton and Graham Sexstone organized the USGS campaign at Ranch Creek that was the focus of a portion of Chapter 2. Jack Tarricone was a substantial sounding board and collaborator for Chapter 3. Kelly Elder collected and provided the in situ data that made Chapter 4 possible. Frequent discussions with him over the last year have improved my understanding of snow hydrology and have helped shape my views as a scientist.

During my time here at CSU, I have had the opportunity to work alongside many graduate students that have comprised Dan's research group, affectionately termed, the CryoCrew. In particular, thank you to Bri Rick and Lucas Zeller – I am grateful for the expertise and camaraderie that you brought to my life. Thank you to Wyatt Reis, Ally Detre, Ash Khatiwada, and Holly Proulx – although our time together was relatively short, you brought much needed warmth and community to our office space.

Thank you to the L-band InSAR Working Group, which started shortly after the NASA SnowEx 2020 campaign. Your passion for radar remote sensing is contagious and you were instrumental in developing my radar background.

During the NASA SnowEx 2020 and 2021 campaigns, many scientists helped collect measurements at Cameron Pass, including Lucas Zeller, Alex Olsen-Mikitowicz, Ella Bump, Rosie Duncan, Wyatt Reis, Coleman Kane, Christoph Suhr, Brendan Auer, John Nelson, and Katie Snelling. Because of your efforts, Chapters 2 and 3 were made possible.

To my family, thank you for your support during this time. Grace, your love and support throughout my PhD program was critical – thank you for putting up with my bizarre hours and near-constant stress-induced state. Florence, you napped on my lap for the first eight months of your life while I frantically worked on Chapters 2 and 3 – I am so proud of the curious person that you are becoming. To my mom, Donna, and dad, Carl, thank you for your support and visits during the last four years, but, perhaps more importantly, thank you for encouraging my curiosity and scientific endeavors from such a young age. To my in-laws, Todd and Debbie, thank you for your support of my endeavors, from watching Florence so I could attend conferences to providing clothing that kept me warm in the field.

Of the six years that I have attended CSU (4 years for PhD), I was an assistant instructor for five of those years at either Colorado State University's or the University of Missouri's Geology Field Camp. This time away from Fort Collins was a much-needed reprieve from the office and helped to shape my core values as a teacher. Thank you to John Singleton, Miriam Barquero-Molina, and Dan McGrath for providing these opportunities.

Finally, I am grateful to NASA FINESST award 80NSSC20k1624 for providing the funding that made this research possible and thank you to the SnowEx leadership team for organizing the SnowEx 2017, 2020, and 2021 Time Series Campaigns, which were the subjects of this dissertation.

TABLE OF CONTENTS

LIST OF TABLES

LIST OF FIGURES

1. INTRODUCTION

Seasonal snowpacks provide water for >1.2 billion people (Barnett et al., 2005), and snowmelt comprises a significant fraction of annual streamflow in arid to semi-arid environments, as shown in the western US (>70%; Li et al., 2017). Snow is an important constituent of the Earth system because snow alters the Earth's surface energy balance by increasing the surface albedo (Warren, 1982), snowpacks provide winter habitat for animals (Slayter et al., 2021), and both snowpacks and subsequent runoff are important for recreation (e.g., skiing, rafting; Scott et al., 2007). Thus, snowpack monitoring is essential to numerous disciplines: from water resource management and drought forecasting (Livneh & Badger, 2020), to predicting animal migrations (Pedersen et al., 2021) and monitoring forest health (Gleason et al., 2021). However, seasonal snowpacks are declining in volume, shifting poleward and upward in elevation, and are melting earlier in response to warming temperatures, effectively changing the historical baseline for streamflow dynamics and groundwater recharge (Hale et al., 2023; Klos et al., 2014; Mote et al., 2018; Siirila-Woodburn et al., 2021). Despite the clear importance of this resource and the recent changes affecting it, no current snowpack monitoring systems (e.g., in situ monitoring stations, data assimilation systems, or remote sensing methods) have sufficient accuracy and spatial representation to monitor snow at high spatiotemporal resolution (<500 m, <weekly) in mountain regions (Dozier et al., 2016; Largeron et al., 2020). Yet, several satellite remote sensing methods for retrievals of snow depth and snow water equivalent (SWE), the height of liquid water represented by the snowpack, have developed in the last decade (e.g., Lievens et al., 2019; Shean et al., 2016; Tsang et al., 2022), and dedicated snow campaigns have prioritized the development, evaluation, and refinement of such techniques (e.g., NASA SnowEx, ESA CoReH2O; Durand et al., 2018; Rott et al., 2008).

1.1 A changing snowpack

The challenge of snowpack monitoring is being compounded by widespread and significant changes to seasonal snowpacks around the globe. Arctic and high elevation regions are warming at faster rates than equatorial and low elevation regions (Pepin et al., 2015). Across the globe in the last ~50 years, the number of regions with declining snow covered area is twice the number of regions with increased snow covered area (Jia et al., 2023). Warming-driven changes to precipitation regimes and snow climatology is projected to cause snowpacks to decline in mountain regions. In the Swiss Alps, increased interannual variability in snow depth is projected over the next fifty years (Willibald et al., 2020), while the greater European Alps are projected to see a 50% reduction in snowmelt runoff by 2100 (Moraga et al., 2021). If the warmest climate scenarios are enacted, snowfall declines of 30–70% are projected for the Himalayas by 2100 (Viste & Sorteberg, 2015). These trends have been documented in North America as well (e.g., Mote et al., 2018), whereas snowpack projections in the South American Andes are highly uncertain because the snowpacks are limited to high elevation glacierized basins that present difficulties for access and infrastructure installation (Fang et al., 2023; Saavedra et al., 2018).

In western North America, >25% of mountain regions saw increased runoff resulting from rainfall compared to snowfall in the spring season from 1950–2013 (Hale et al., 2023), while SWE losses of 15–30% have been observed over the last 70 years in the western US (Mote et al., 2018). An additional 25% of western US present day SWE is expected to be lost by 2050 (Siirila-Woodburn et al., 2021). In the upper Colorado River basin, simulations for warmer conditions found that the date of peak SWE could shift by 17–23 days with decreased snowmelt-derived streamflow across all elevations (Hammond et al., 2023). The rain-snow transition zone

has increased in elevation, with a projected reduction of 24–53% of land area that falls within a wintertime snowfall regime (Klos et al., 2014). In some mountain regions, compared to historical melt seasons, the timing of snowmelt has seen a 2–3 week earlier initiation of snowmelt (e.g., Colorado; Clow, 2010; Hale et al., 2023). Because of the documented changes to snowpacks and the pressing need for better monitoring for water resource management, the National Academies of Sciences, Engineering, and Medicine emphasized high spatiotemporal retrievals of SWE as a high priority in the recent Decadal Survey (National Academies of Sciences, Engineering, & Medicine, 2017).

1.2 Current state of snowpack monitoring

The USDA Natural Resources Conservation Service operates the SNOTEL network across the western US and Alaska (>900 automated stations) and executes monthly snow depth and SWE surveys along 300 m transects at selected mountain basins. This network of stations, with many stations operating since the 1960s, enables long-term climate studies (e.g., Fassnacht et al., 2018; Mote et al., 2018) and is a primary input for leading snow models (e.g., the Snow Data Assimilation system (SNODAS)). However, the network is sparsely populated because of the infrastructure expenditure and the difficulty of accessing remote mountain basins. Additionally, sites are typically within a narrow elevational range and in small forest openings that are nearly flat. Thus, the network fails to capture the inherent spatial variability of snow (Dozier et al., 2016).

To better capture the spatial variability and improve snowmelt forecasting, several models that assimilate a range of meteorological variables have been developed. SNODAS, developed by the National Oceanic and Atmospheric Organization, provides daily snow depth and SWE estimates at 1 km spatial resolution that are based on assimilated in situ observations

from automated station networks and modeled meteorological data within a physics-based model. Studies that have evaluated SNODAS have shown that it has decreased SWE accuracy for alpine regions in Colorado (Clow et al., 2012) and tends to underestimate snow depths in deeper snow areas (Hedrick et al., 2015). A data assimilation system developed by the University of Arizona assimilates PRISM precipitation output (4 km horizontal resolution; Daly et al., 1994) to estimate daily SWE/snow depth (4 km spatial resolution; Broxton et al., 2024). Finally, the WRF regional climate model has been implemented for higher resolution (<1 km) modeling to better understand the dynamics of snow distribution (e.g., Wrzessien et al., 2018). Despite the uncertainties and coarser spatial resolution of such models, these models outperform global land data assimilation systems, which have very coarse resolutions (>30 km spatial resolution) and can underestimate SWE by 51–72% (Broxton et al., 2016).

Airborne lidar measurements of snow depth have high accuracy in complex mountain environments (RMSE = 8–14 cm; McGrath et al., 2019; Painter et al., 2016) and can be coupled with density estimates from a physics-based model to operationally estimate SWE with RMSE as low as 8 mm (e.g., Airborne Snow Observatory; Painter et al., 2016). Thus, this method is highly sought for basin-wide mapping of snow depth and SWE. Typically, lidar is flown once or twice during the snow accumulation season to estimate peak SWE for targeted basins of interest. A primary limitation of this method is the estimation of SWE based on the modeled snow density (Rayleigh & Small, 2017) because physics-based models (e.g., iSnobal) are inherently limited by the accuracy of the forcing data (Meyer et al., 2023). The method is also limited by flight costs, flight time, and cloud cover, and thus airborne lidar is an unlikely candidate for global SWE mapping. However, airborne lidar is drawing investment from water managers and increased

competition to meet lidar demands are decreasing lidar costs, potentially leading to this technique being flown more often and in more basins.

1.3 Space-age technologies for measuring mountain snow

The previous decade has seen significant advancement towards accurate satellite-borne snow depth and SWE remote sensing methods. Given the impetus for snow depth and SWE retrievals at high spatiotemporal resolution, snow depth/SWE remote sensing method development and evaluation in mountain regions has primarily emphasized depth-based and radar-based methods that have high spatial resolutions, rather than the coarser passive microwave methods. Here, we define depth-based methods as those that measure the elevations of surfaces (e.g., lidar and photogrammetry), whereas radar-based methods rely on a radar signal that is transmitted through the snowpack (e.g., SAR, FMCW). Both depth-based and radar-based methods were prioritized and tasked during the NASA SnowEx campaigns.

Lidar (e.g., Painter et al., 2016), photogrammetry (e.g., Marti et al., 2016; Shean et al., 2016), and single-pass Ka-band InSAR applied in wet snow conditions (e.g., Moller et al., 2017) are defined here as depth-based methods. These methods derive surface elevations from a snow-free and a snow-on acquisition, and subsequently calculate snow depth by subtracting the surface elevations of the snow-free survey from the elevations of the snow-on survey (Deems et al., 2013). Applicable satellite platforms include ICESat-2 for lidar and stereo/tri-stereo imagery for photogrammetry. Recent ICESat-2 studies have found that the technique is capable of measuring snow depth in mountain terrain and in both non-forested and forested environments (RMSE = 0.18–0.33 m; Besso et al., 2024), but uncertainty increases with increasing surface slope and results in larger errors (Enderlin et al., 2022). Although photogrammetry from stereo/tri-stereo imagery is not capable of measuring snow depths below canopy cover or cloud cover, the

technique has more continuous spatial coverage than ICESat-2 and a much higher revisit frequency. For example, ICESat-2 acquisitions were designed to have an exact repeat every 91 days in polar regions and the ESA Pléiades stereo satellite constellation has a repeat orbit every 26 days. Stereo/tri-stereo satellite photogrammetry yielded high spatial resolution (<2 m) snow depths with RMSE of 0.23–0.48 m over the relatively flat Grand Mesa, CO (Hu et al., 2023; McGrath et al., 2019) and 0.80 m over the topographically complex Tuolumne River Basin, CA (Deschamps-Berger et al., 2020). Importantly, the technique can be applied globally and has led to increased understanding of the seasonal snowpack development in the data-sparse Andes (Shaw et al., 2020). A final consideration for depth-based techniques is that SWE, the most important hydrologic variable, is calculated from snow depth multiplied by snow density, which must either be measured in the field or modeled. Field measurements of snow density are sparse and modeled snow density has been shown as a leading source of uncertainty for airborne lidar-derived SWE (Raleigh & Small, 2017).

Radar-based methods for the retrieval of snow depth and SWE have been implemented through ground-based instruments for more than two decades (e.g., Hardy et al., 2008; Lundberg et al., 2006; Marshall et al., 2004). Common ground-based radars include ground-penetrating radar (GPR; McGrath et al., 2019) and frequency-modulated continuous-wave radar (FMCW; Marshall et al., 2004). These radars record the time-of-flight from signal transmission to return, and thus record the two-way travel time of the transmitted radar wave through the snowpack, which can be converted to snow depth and SWE. More recently, synthetic aperture radar (SAR), which is capable of high spatial resolution <100 m) has been studied as a potential method for snow depth/SWE retrievals from satellite platforms. SAR signals are polarized and typically transmitted in horizontal (H) or vertical (V) orientation. Signal returns are recorded in a co-

polarized channel (e.g., H-transmit, H-receive) and/or a cross-polarized channel (e.g., H-transmit, V-receive). SAR is capable of canopy penetration, particularly at lower frequencies (e.g., L-band, 1–2 GHz, ~25 cm wavelength). SAR records the amplitude and phase of the returned signal and thus SAR techniques for snow depth/SWE retrievals are divided into backscatter methods and SAR interferometry (InSAR) methods.

SAR backscatter methods for snow depth or SWE retrievals have been primarily implemented for frequency bands of C (4–8 GHz), X (8–12 GHz), and Ku (12–18 GHz). As frequency increases, wavelength decreases and the signal interaction with the snowpack microstructure increases. High frequency (i.e., X-, Ku-bands) SAR was tested as part of the NASA SnowEx campaigns with the SWESARR (SnowEx 2020 & 2023) and SnowSAR (SnowEx 2017) instruments. The technique appears promising for retrieving SWE up to 800 mm (Borah et al., 2023) and it is capable of measuring SWE below forest cover if the backscattering properties of the forest can be effectively modeled (Tsang et al., 2022), but the technique notably breaks down when the snowpack is wet. A recent development with the Sentinel-1 (C-band SAR) constellation has shown that snow volume scattering occurs at C-band as well and can be used to retrieve snow depth (Brangers et al., 2023; Lievens et al., 2019, 2022), but the technique has higher uncertainties below forest cover, in wet snowpacks, and at lower snow depths (Broxton et al., 2024; Lievens et al., 2022).

InSAR for SWE retrievals was first implemented by Guneriussen et al. (2001), who determined that snow accumulation could cause phase deformation within InSAR pairs of the ERS 1/2 satellites (C-band). Guneriussen et al. (2001) used a pair of snow-free/snow-on SAR acquisitions, but subsequent research has shown that the method is particularly powerful when applied to repeat SAR acquisitions (temporal baseline <1 month), which preserves temporal

coherence and can map changes in SWE by assuming that snow accumulation or ablation at the snow surface is the primary contributor of the phase change (Deeb et al., 2011; Leinss et al., 2015). Subsequent satellite studies from Sentinel-1 in the boreal forests of Norway (Conde et al., 2019) and the mountains of Idaho, USA (Oveisgharan et al., 2023) have shown that the technique is viable from a C-band SAR satellite platform with a 6-day temporal baseline (RMSE = 8 mm, Oveisgharan et al., 2023). The technique is particularly promising at L-band due to its longer wavelength which allows temporal coherence to be maintained for longer periods of time. With the upcoming launch of the L-band NISAR satellite in mind, the NASA Uninhabited Aerial Vehicle SAR (UAVSAR) was tasked to acquire airborne L-band SAR imagery during the SnowEx 2020 and 2021 Time Series Campaigns in the western. Subsequent studies from the Campaigns have shown that the technique compares well with changes in SWE mapped from lidar over a flat and unforested section of Grand Mesa, Colorado (RMSE = 8 mm; Marshall et al., 2021), and the technique held coherence during the early melt season in the Jemez Mountains of New Mexico in 2020, where InSAR-measured SWE losses yielded good agreement with losses in fractional snow covered area (Tarricone et al., 2023). Still, several uncertainties remain, including atmospheric corrections, radar signal over wet snowpacks, steep topography and incidence angles, and, in particular, the influence of forest cover.

1.4 Evaluating and developing methods for L-band radar to improve snow remote sensing

Current snow survey protocols measure bulk snow density at sparse intervals that likely fail to capture the spatial variability of snow density (Meehan et al., 2023). Snow density is a primary input for the retrieval of SWE from depth-based methods, time-of-flight radar methods, SAR backscatter methods, and InSAR acquisitions over wet snow. Despite the importance of snow density for SWE retrievals, leading snow models can yield a wide range of densities for

any given date, indicating that density modeling is a primary source of uncertainty for depth-based methods (Rayleigh & Small, 2017), although radar-based methods tend to be less sensitive to the input snow density (e.g., Hoppinen et al., 2023). In Chapter 2, I implemented a technique for estimating spatially distributed snow relative permittivities and densities from combined lidar-measured snow depths and snowpack time-of-flights from L-band ground-penetrating radar (GPR). Combining these two spatially distributed measurements enables the estimation of density with unprecedented spatial coverage (McGrath et al., 2022; Meehan et al., 2023). After deriving snow densities and relative permittivities, we evaluated the spatial variability of both parameters and compared our results with modeled snow densities to better understand the applications and limitations of various density models.

SWE retrievals are a promising application for the upcoming L-band NISAR satellite (planned launch April 2024). To better understand this technique, NASA SnowEx implemented the SnowEx 2020 Time Series Campaign which involved ~weekly NASA UAVSAR acquisitions at 13 field sites during the winter in the mountains of the western United States (Marshall et al., 2019). Due to the Covid-19 pandemic, the campaign was cut short in March 2020 and subsequently restarted at six mountain field sites and one prairie field site in 2021 (Marshall et al., 2020). I participated in the campaigns at Cameron Pass, Colorado and helped collect weekly surveys, coinciding with UAVSAR acquisitions, of GPR to estimate distributed SWE across 1.6 km of transects in 2020 and 2.4 km of transects in 2021. Additionally, terrestrial lidar surveys were conducted, coinciding with two InSAR pairs. In Chapter 3, I evaluated SWE retrievals from 10 UAVSAR pairs using the GPR and terrestrial lidar surveys to constrain the accuracy of the technique in relatively flat, mostly non-forested, sub-alpine terrain. Further, interferometric coherence was explored as a potential metric for ΔSWE retrieval error.

In Chapter 4, I evaluated the uncertainty of L-band InSAR SWE retrievals below forest cover using 2021 UAVSAR acquisitions over Fraser Experimental Forest, Colorado and in situ measurements of snow depth and SWE. Fraser Experimental forest has a large elevation gradient (~1000 m) and is primarily forested by old growth forests, although selected forest plots were clear cut within the last century as part of an experimental management plan (Alexander et al., 1985). In total, I evaluated SWE retrievals from eight UAVSAR pairs using in situ measurements collected for the SnowEx 2021 Campaign by the experimental forest director and a team of field scientists, as well as a set of airborne lidar surveys. Results contextualize the applicability of the L-band InSAR approach for SWE retrievals within forested watersheds.

2. SNOWPACK RELATIVE PERMITTIVITY AND DENSITY DERIVED FROM NEAR-COINCIDENT LIDAR AND GROUND-PENETRATING RADAR[1]

2.1 INTRODUCTION

Seasonal snow covers up to 60 % of the Northern Hemisphere land area (Hammond et al., 2018; Kim, 2018) and serves as a vital water resource for ecosystems spanning prairies, mountains, tundra, and boreal forests (Sturm et al., 1995). Mountains tend to accumulate deep snowpacks that provide water resources for one sixth of the world's population (Barnett et al., 2005; Mankin et al., 2015). In North America, mountains comprise 25 % of the land area but store 60 % of the total snow water equivalent (SWE; Wrzesien et al., 2018). Warming in the mountainous western United States (U.S.) has caused SWE losses of 15–30 % over the last 70 years (Mote et al., 2018), while a further 25 % loss in SWE is predicted by 2050 (Siirila-Woodburn et al., 2021). These changes, compounded with human dependence upon snow water resources, make the pursuit of global SWE estimates a highly prioritized, trillion-dollar endeavor (National Academies of Sciences, Engineering, and Medicine, 2018; Sturm, 2015). Currently, no single method or ensemble of methods has proven capable of measuring SWE to the high standard of accuracy established for global monitoring (Dozier et al., 2016). Recent campaigns, such as the U.S.-based National Aeronautics and Space Agency (NASA) Snow Experiment (SnowEx; Durand et al., 2018) and the Europe-based NoSREx and APRESS (Tsang et al., 2022), evaluated a suite of remote sensing approaches (e.g., lidar, radar) for SWE-mapping applications. At the watershed scale, light detection and ranging (lidar) operations, such as the Airborne Snow

[1] Chapter published as Bonnell, R., McGrath, D., Hedrick, A. R., Trujillo, E., Meehan, T. G., Williams, K., Marshall, H. P., Sexstone, G., Fulton, J., Ronayne, M. J., Fassnacht, S. R., Webb, R. W., & Hale, K. E. (2023). Snowpack relative permittivity and density derived from near-coincident lidar and ground-penetrating radar. *Hydrological Processes, 37*(10), e14996. https://doi.org/10.1002/hyp.14996

Observatory (ASO), have demonstrated operational feasibility (Deems et al., 2013; Painter et al., 2016), but can be cost prohibitive. Satellite remote sensing methods for SWE-mapping have been under development for decades (Dietz et al., 2012; Nolin, 2010; Shi et al., 2016) and see continued interest, particularly in data assimilation applications, wherein derived snow products are integrated within physically based snow models (Largeron et al., 2020). For simplification, we discuss two major approaches of snow remote sensing: depth-based and radar-based methods. Both approaches have high spatial resolution and accuracy and are thus forerunners in the development of satellite-based SWE retrievals in mountains (Dozier et al., 2016).

Measuring SWE from depth-based remote sensing approaches relies on differencing repeat surface elevation measurements (i.e., snow-free from snow-on elevation surfaces) to derive snow depth (Currier et al., 2019; Deems et al., 2013). For this approach, SWE is the product of the derived snow depth (d_s) and snow density (ρ_s):

$$SWE_{depth-based} = d_s \times \rho_s \quad \text{Equation 2.1.}$$

Depth-based methods are primarily limited to the optical to near infrared portion of the electromagnetic spectrum, where atmospheric transmission is high, and wavelengths are significantly smaller than snow grains. Depth-based methods, including photogrammetry and lidar, have demonstrated potential for satellite platforms (Enderlin et al., 2022; Shean et al., 2016).

Radar-based methods further require an estimate of relative permittivity (ε_s) to characterize the electromagnetic wave velocity of the snowpack to derive snow depth, and thereby SWE, from the signal path length (l_p; e.g., two-way travel time; Marshall et al., 2005). Thus, radar-based SWE is generally expressed as a function,

$$SWE_{radar-based} = f(l_p, \varepsilon_s(\rho_s, \theta_{LWC})) \quad \text{Equation 2.2,}$$

where the relative permittivity, a measure of the ability of a material to store charge relative to free-space (Daniels, 2004), is controlled by the snow density and volumetric liquid water content (LWC; θ_{LWC}). In dry snow, dielectric permittivity is primarily determined by snow density. However, wet snow permittivity exhibits a large dependence on LWC because the relative permittivity of water is ~60 times that of snow (Bonnell et al., 2021). LWC induces the imaginary component of relative permittivity and acts as a frequency-dependent attenuator of signal strength (Koch et al., 2014), an attribute which was leveraged by Bradford et al. (2009) as the first study to derive spatially distributed LWC along a ground-penetrating radar (GPR) transect. At least six equations have been published for the relative permittivity of wet snow, whereas there are >19 published equations relating the relative permittivity of dry snow to its density, effectively increasing the uncertainty of radar-based SWE retrievals due to a large range in permittivity for a given snow density (Di Paolo et al., 2020). Not all radar SWE retrieval approaches utilize the signal path length through the snow. Some approaches, such as the Ka-band interferometry for wet snow conditions (Moller et al., 2017), may be better described as depth-based approaches, whereas Synthetic Aperture Radar (SAR) backscatter approaches rely on empirical models that are at least partly dependent on the snowpack relative permittivity (Tsang et al., 2022).

Density, a required input for both SWE approaches, can be either modeled or measured in snow pits, along snow courses, or by automated weather stations with a depth sensor co-located above a snow pillow. Density varies at the hillslope scale (Alford, 1967) due to differences in overburden pressure, radiation inputs, and wind and precipitation patterns (Winkler et al., 2021). However, density tends to vary less than snow depth, and because manual measurements are time-consuming, studies generally assume limited spatial snow density variability (López-

Moreno et al., 2013; Shook & Gray, 1996; Sturm et al., 2010). Thus, current density sampling approaches may acquire measurements too sparsely to capture its inherent spatial variability (Meehan, 2022), making snow density models an appealing alternative for remote sensing approaches.

Selecting an appropriate density model can be difficult. There are three broad categories: empirical models (Avanzi & De Michele, 2015), physically based models (e.g., Havens et al., 2020; Lehning et al., 2002a, 2002b; Marks et al., 1999), and data assimilation systems (Largeron et al., 2020), and within each category, numerous models exist. Additionally, evaluation efforts outside of the original publications are limited. Empirical models are developed using a statistical relation between snow density, a time parameter (e.g., month), and, in more complicated equations, snow depth and geographic metrics. Physically based models can be powerful predictive tools but tend to be computationally expensive, require extensive meteorological forcing datasets, and often use simplified densification formulas (Hedrick et al., 2018). Empirical models can be simpler to implement and produce statistically robust estimates at the interannual scale, however few accurately capture short-term variability in snow density (McCreight & Small, 2014). Empirical models requiring snow depth as an input cannot be directly inserted into radar SWE retrieval equations because radar methods cannot estimate depth independently from density. Some of these models have been intercompared to assess sensitivity and bias (e.g., McCreight & Small, 2014; Avanzi & De Michele, 2015; Raleigh & Small, 2017), but comparisons have been limited by the scope of available in situ snow density measurements. Density estimates from data assimilation methods are a third option, though measurements are coarse in resolution (>1 km; Largeron et al., 2020). Recent published density models include a semi-empirical model that balances computational efficiency by implementing a simplified

physically based snow compaction equation within an empirical framework (Winkler et al., 2021), and empirical models that estimate snow density from a suite of lidar-derived parameters (Bisset et al., 2022; Meehan, 2022). Both model types are optimized for depth-based remote sensing methods: the semi-empirical model ingests repeat-measured snow depths acquired with low temporal baselines (≤ 7 days) and may be implemented for any given year/location, whereas lidar-derived models are designed and implemented for a single lidar survey (Meehan et al., 2022).

GPR measures the two-way travel time (*twt*) of the radar wave through the snowpack, which can be combined with lidar-measured snow depths to estimate radar velocity and relative permittivity. Several studies have established this method and converted relative permittivity to LWC by constraining snow density using snow pit measurements (Bonnell et al., 2021; Heilig et al., 2015; Webb et al., 2018, 2020a). More recent studies have used this technique to derive snow density by coupling uncrewed aerial vehicle (UAV) Structure from Motion (SfM) measurements of snow depth with GPR-measured *twt* and identified spatial variabilities that were larger than variabilities mapped by previous in situ studies (McGrath et al., 2022; Yildiz et al., 2021). We expanded on previous work by leveraging a time series of GPR and lidar datasets from Grand Mesa and Cameron Pass, Colorado, and a one-off survey conducted at Ranch Creek, Colorado. We combined lidar-measured snow depths with GPR-measured *twt* of the snowpack thickness to derive spatially distributed relative permittivity in both dry and wet conditions. For dry-snow surveys only, relative permittivity is converted to density using three different equations to illustrate the variability in published equations. We then compared the derived densities with in situ measurements and selected the most representative equation. Given the upcoming launches of L-band (1–2 GHz) SAR satellites (e.g., ALOS-4, NISAR, ROSE-L, and TanDEM-L) and their

potential for global SWE-monitoring (Deeb et al., 2011; Guneriussen et al., 2001; Marshall et al., 2021; Tarricone et al., 2023), we estimated the spatial variability of derived relative permittivity and snow density at the approximate scale of SAR satellite platforms by conducting a variogram analysis. Derived densities were then used to evaluate modeled densities from four empirical models, the Snow Data Assimilation System (SNODAS; Barrett, 2003), and iSnobal (Lehning et al., 2002a, 2002b), with particular attention given to model performance within depth-based and radar-based SWE remote sensing methods.

2.2 FIELD SITES

We used 1.0 and 1.6 GHz center-frequency (L-band) GPR *twt* measurements of the snowpack thickness, lidar-measured snow depths, and snow pit-measured densities collected during the NASA SnowEx 2017 Grand Mesa Campaign, the NASA SnowEx 2020–21 Time Series Campaigns at Cameron Pass, and a single survey led by the U.S. Geological Survey (USGS) at Ranch Creek in 2021 (Figure 2.1). An overview of the dates and technical aspects of the instrumentation used at each field site is shown in Table 2.1.

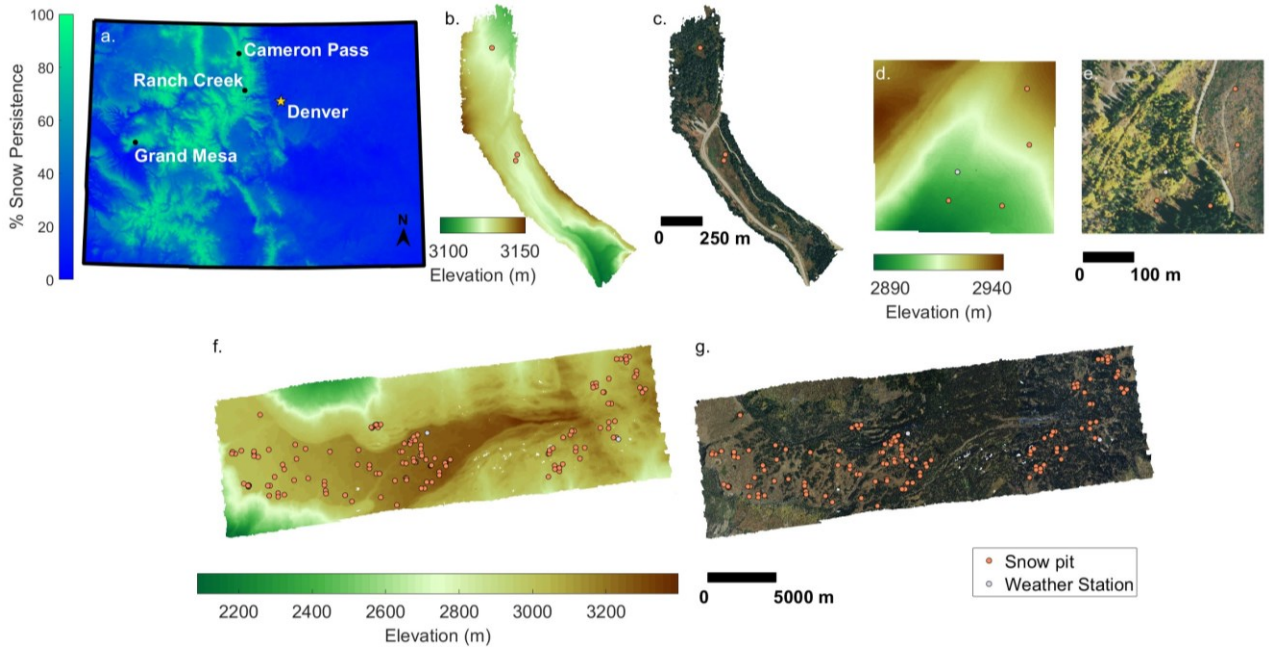

Figure 2.1: (a) Location of field sites within Colorado and 1 January to 1 July snow persistence (Moore et al., 2015). (b) Digital elevation model (DEM; Painter & Bormann, 2020) and (c) National Agriculture Imagery Program (NAIP) imagery of Cameron Pass, with snow pit locations. (d) DEM and (e) NAIP imagery of Ranch Creek, with weather station and snow pit locations. (f) DEM and (g) NAIP imagery of Grand Mesa, with locations of SNOTEL stations and snow pits. Figure scales and color ramps differ by field site. The vertical datums are the WGS84 Ellipsoid for Grand Mesa and the NAVD88 Geoid 18 for Cameron Pass and Ranch Creek. NAIP imagery acquired from USGS Earth Explorer (https://earthexplorer.usgs.gov/, accessed 10 October 2022).

Table 2.1: Technical details of the instrumentation and datasets for each of the field sites in Colorado. Water Year is abbreviated to WY. Grand Mesa vegetation summary sourced from Webb et al. (2020b). Cameron Pass and Ranch Creek vegetation notes were taken in the field and verified with Huckaby & Moir (1998) and Fassnacht et al. (2018).

Study Site	Grand Mesa	Cameron Pass	Ranch Creek
Date Range	*WY 2017*: 8 – 25 Feb	*WY 2020*: 18 Dec – 12 Mar *WY 2021*: 10 Feb – 27 May	*WY 2021*: 7 Apr
Lidar Platform	Airborne Riegl Q1560	Terrestrial Riegl VZ-2000/6000 UAV Yellowscan VX20	UAV Yellowscan VX20
GPR System	MALA ProEx 1.6 GHz	Sensors & Software PulseEkko 1.0 GHz	Sensors & Software PulseEkko 1.0 GHz
Study Site Area	500 km^2	0.10 km^2	0.10 km^2
Data Boundaries	*Latitude*: 38.941, 39.152 *Longitude*: –108.259, –107.820	*Latitude*: 40.512, 40.527 *Longitude*: –105.896, –105.884	*Latitude*: 39.912, 39.916 *Longitude*: –105.763, –105.757
Coordinate Systems	*Horizontal*: WGS84/UTM Zone 13N *Vertical*: WGS84 Ellipsoid	*Horizontal*: NAD83 (2011)/UTM Zone 13N *Vertical*: NAVD88/GEOID 18	*Horizontal*: NAD83 (2011)/UTM Zone 13N *Vertical*: NAVD88/GEOID 18
Vegetation Summary	*Open*: Grasses and Shrubs *Forest*: Lodgepole, Spruce, Fir, Aspen	*Open*: Mixed Willows and Grasses	*Open*: Mixed Willows *Forest*: Lodgepole and Aspen

SnowEx 2017 was conducted from 6–25 February of water year (WY) 2017 at Grand Mesa (Figure 2.1f–g). The campaign consisted of three (8, 16, and 25 February) airborne lidar surveys, collected and processed by ASO (Painter, 2018). Surface-coupled, common-offset GPR (Webb et al., 2019) was collected daily on a sled pulled behind either a skier/snowshoer or

snowmobile along transects and small grids. Two adjacent SNOTEL stations, Park Reservoir and Mesa Lakes SNOTELs, recorded negligible net changes in snow depth (+0.00–0.03 m) for 8–16 February and modest net increases (+0.03–0.08 m) for 16–25 February (Figure A1a,d). For the 8 and 16 February flights, we selected only GPR collected ±2 days around the ASO flight date to limit the uncertainty of snow deposition that occurred on 11–12 February, resulting in 4.8 km of GPR data for the 8 February flight and 8.8 km for the 16 February flight. GPR efforts during the third week of the campaign were focused on small-scale (<500 m) variability. Because limited snow accumulation (<5 mm SWE) occurred after 20 February, the 2.6 km of GPR collected from 21–25 February were included.

The Cameron Pass and Ranch Creek field sites (Figure 2.1b–e; <0.5 km^2) are much smaller than Grand Mesa (46 km^2). However, Cameron Pass was one of several sites observed during the NASA SnowEx 2020–21 Time Series Campaigns (Marshall et al., 2019) and thus offers a longer time series that spans two accumulation seasons and one ablation season. Ranch Creek was also surveyed during the ablation season and adds information to the distribution of relative permittivity in wet snowpacks. At Cameron Pass, terrestrial lidar scans (TLS) were collected on 18 December, 26 February, and 12 March during WY 2020 and on 10, 24 February, 22 March, and 27 May during WY 2021 (Williams, 2021). This site included repeat 0.5 km GPR transects in 2020 and repeat 0.9 km transects in 2021 (Bonnell et al., 2022; McGrath et al., 2021). The nearby Joe Wright SNOTEL station (Figure A1b,e) recorded snow depth changes of +0.97 m (+280 mm SWE) and –0.17 m (+40 mm SWE) between the three WY 2020 surveys, and +0.10 m (+59 mm SWE), +0.41 m (+119 mm SWE), and –0.84 m (–104 mm SWE) between the four surveys conducted in WY 2021. Ranch Creek was surveyed on 7 April 2021 using a lidar system borne by a UAV (Bauer et al., 2023), while 2.9 km of GPR data were collected in a

spiral survey design (Bonnell & McGrath, 2023). The Ranch Creek survey was conducted 10 days after peak SWE was observed by the nearby USGS weather station (29 March; Figure A1c,f), which had lost 0.31 m snow depth (135 mm SWE) over that same time period.

2.3 METHODS

2.3.1 Calculating relative permittivity and snow density

Lidar-measured snow depths were collected from one of three platforms: airborne (Grand Mesa), terrestrial (Cameron Pass), and UAV-borne (Ranch Creek). GPR radargrams were collected as common-offset surveys via a sled coupled to the snow surface and utilized L-band center-frequency. Processing of lidar point clouds collected by terrestrial and UAV platforms generally followed the workflow outlined by Currier et al. (2019), whereas radargram processing and picking of snowpack *twt* thickness followed McGrath et al. (2019). Appendix Text A.1 provides further details of the data processing.

A common practice of GPR in snow applications is to convert the *twt* of the snowpack thickness to snow depth (d_s; e.g., Lundberg et al., 2006; Marshall et al., 2005), using an estimate of the snowpack radar velocity (v_s; Daniels, 2004):

$$d_s = \frac{twt}{2} \times v_s \qquad \text{Equation 2.3.}$$

Radar velocity is estimated from the relative permittivity of the snowpack,

$$v_s = \frac{c}{\sqrt{\varepsilon_s}} \qquad \text{Equation 2.4,}$$

where c is the velocity of electromagnetic radiation in a vacuum. Here, we constrain the snow depth using lidar and directly estimate relative permittivity:

$$\varepsilon_s = \left(\frac{c \times twt}{2 d_s}\right)^2 \qquad \text{Equation 2.5.}$$

In dry snow, snow density can be estimated directly from a relative permittivity equation. Because the choice of an equation is not straightforward (Di Paolo et al., 2020), we calculated snow density from three permittivity equations. Of the published equations and for a given relative permittivity, the Kovacs et al. (1995) equation (Equation 6) estimates the median density, the Kuroiwa (1954) equation (Equation 7) estimates the minimum density, and the Webb et al. (2021) equation (Equation 8) estimates the maximum density (Di Paolo et al., 2020). The three equations are:

$$\varepsilon_s = \left(1 + 0.845\frac{\rho_s}{1000}\right)^2 \quad \text{Equation 2.6,}$$

$$\varepsilon_s = 1 + 2.3\frac{\rho_s}{1000} \quad \text{Equation 2.7,}$$

$$\varepsilon_s = 1 + 1.4 \times 10^{-3}\rho_s + 2 \times 10^{-7}{\rho_s}^2 \quad \text{Equation 2.8.}$$

The equations are written such that units for density (ρ_s; kg m^{-3}) are consistent.

Measurements of twt were binned within lidar grid cells (3 m x 3 m) by calculating the median twt value per cell. Grid cells that did not meet a minimum threshold of 15 *twt* measurements within the cell were removed from the analysis. Relative permittivity was calculated from coincident snow depth and twt cells (Equation 5). Previous studies have established a large randomly distributed error in the relative permittivity estimates that results from uncertainties in snow depths and *twt*, but with sufficient sampling and filtering, a robust estimate can be established (Bonnell et al., 2021; McGrath et al., 2022; Meehan et al., 2022). Erroneous relative permittivity values (e.g., ε_s <1) were reduced by removing all values outside of the inter-quartile range. Uncertainties were further reduced by smoothing the remaining relative permittivity estimates with a 21 m x 21 m moving window median filter. A filter of this size was chosen to retain spatial variability along the transect-oriented surveys. We categorized surveys as dry or wet based on the presence of any LWC noted in snow pits and corroborated by

pit temperatures (Appendix Text A.2; Figure A2). Relative permittivity estimates obtained in dry-snow conditions (all surveys, except the 7 April and 27 May 2021 surveys) were then converted to density using the Kovacs et al. (1995), Kuroiwa (1954), and Webb et al. (2021) equations and compared to in situ density measurements to calculate the RMSE and Pearson correlation coefficient to determine the most representative equation.

2.3.2 Uncertainty analysis

We estimated the uncertainty in relative permittivities through Monte Carlo simulations for each survey date. The mean snow depth and *twt* were calculated from the 3 m rasters. Grand Mesa lidar snow depth uncertainty was estimated from the extensive comparisons between the Grand Mesa airborne lidar and snow depth probes established by Currier et al. (2019). For Cameron Pass, the lidar snow depth uncertainty was estimated using the standard deviation of elevational differences between the bare-earth and snow-on DEMs along the CO-14 highway surface. The Ranch Creek lidar snow depth uncertainty was estimated from comparison with surveyed ground control points (Bauer et al., 2023). Uncertainties in *twt* were estimated from the mean within-pixel *twt* standard deviation for each survey date. Then, Monte Carlo simulations with 100,000 realizations from Equations 4–5 were performed using a random normal distribution, where the uncertainty estimates were considered representative of the standard deviation around the mean snow depth and *twt*. This established estimates for the mean and standard deviations of derived relative permittivity and snow density for each survey date, which is estimated as the uncertainty range in our derived relative permittivity and snow density datasets. All Monte Carlo simulation parameters and estimates are listed in Table A1.

2.3.3 Variogram analysis

We conducted a variogram analysis using a lag spacing of 10 m, which approximates the spatial resolution of SAR satellites. Variance at the lag spacing, *γ(h)*, for experimental variograms is given as,

$$\gamma(h) = \left(\frac{1}{2N(h)}\right) * \sum_{i=1}^{N(h)} (x_i - x_{i+h})^2 \quad \text{Equation 2.9,}$$

where *N(h)* is the number of point-pairs at the given lag spacing and x is the variable of interest (Anderson et al., 2014; Schwangart, 2022a; Webster & Oliver, 2001). Omni-directional experimental variograms were computed from the datasets for snow depth, *twt*, relative permittivity, snow density, and SWE (achieved by multiplying the derived snow density by its corresponding snow depth). Experimental variograms were computed using the same grid cells across all variables for the given survey date. Based on the shape of calculated experimental variograms, we identified the exponential model as the most representative variogram model for each of the variables. The exponential variogram model with a nugget effect is given as

$$\gamma(h) = s_0 + s * (1 - e^{-\frac{h}{a}}) \quad \text{Equation 2.10,}$$

where *a* is the correlation distance, s_0 is the nugget effect, and *s* is the exponential model contribution to the sill (Isaaks & Srivastava, 1989). Variogram model parameters were estimated by least-squares fitting (Schwanghart, 2022b). For the Grand Mesa datasets, sufficient GPR observations were collected in forests to enable variogram analyses of snowpacks in both forests and open environments. Following McGrath et al. (2019), we chose a 2 m vegetation height metric and used the ASO vegetation heights dataset collected in Fall 2016 (Painter & Bormann, 2020) to generate a binary forest/open mask. Variograms were not calculated for snow density or SWE when LWC was present in the snowpack (i.e., 7 April and 27 May 2021).

2.3.4 Modeling snow density

We tested density estimates from four empirical models, SNODAS, and iSnobal against our derived density dataset. Evaluated empirical models include Mizukami & Perica (2008; $M\&P_{08}$), Jonas et al. (2009; J_{09}), Sturm et al. (2010; St_{10}), and Sexstone & Fassnacht (2014; $S\&F_{14}$). Of these, St_{10} and J_{09} have global applications and were previously implemented in a lidar SWE-retrieval study (Raleigh & Small, 2017). We included $S\&F_{14}$, developed for the watershed adjacent to Cameron Pass, to evaluate whether a locally derived model offers any advantage over global models. $M\&P_{08}$ is a simpler model, designed to ingest only the day-of-year (DOY) and a snow climate parameter, but Pistocchi (2016) suggests such models can be statistically robust, and it is one of the few empirical models which can be ingested into a radar-based remote sensing method. SNODAS was chosen to represent data assimilation methods, given its use as a benchmark for evaluating larger scaled models (Broxton et al., 2016) and history of validation efforts (Clow et al., 2012; Hedrick et al., 2015; Lv et al., 2019). The iSnobal model (Havens et al., 2020; Marks et al., 1999) was chosen because of its incorporation into lidar SWE products geared toward operational water supply applications (Painter et al., 2016). iSnobal was run over Cameron Pass for both unscaled (iSn_{un}) and rescaled (iSn_{re}; e.g., Hale et al., 2023; Kiewiet et al., 2022; Vögeli et al., 2016) precipitation scenarios because the chosen atmospheric model used for meteorological forcing within iSnobal, the High Resolution Rapid Refresh (HRRR) model, has been shown to underreport SWE by up to 25% (Meyer et al., 2023). Only surveys with dry snow conditions were modeled. An overview of the model parameters is given in Table A2 and further details regarding model runs are provided in Appendix Text A.3.

All modeled densities were compared with derived densities and the average of the in situ measurements. Modeled densities were incorporated with lidar snow depths and GPR *twt* to calculate depth-based SWE and radar-based SWE. In situ measurements were averaged for each

date and used to calculate depth-based SWE from the lidar snow depths and radar-based SWE from *twt* to evaluate the efficacy of snow models compared to the "gold standard." The RMSE was then calculated for modeled vs. derived densities, modeled and in situ vs. derived depth-based SWE, and modeled and in situ vs. derived radar-based SWE.

2.4 RESULTS

2.4.1 Overview of the derived relative permittivity and snow density datasets

We evaluated the lidar-GPR derived snow densities from the three relative permittivity equations using 40 snow pits from Grand Mesa (median = 322 kg m^{-3}, range = 93 kg m^{-3}) and six snow pits from Cameron Pass (median = 255 kg m^{-3}, range = 92 kg m^{-3}). Ranch Creek was excluded from this analysis because of wet snow conditions. Grand Mesa snow pits had an average of 19 derived snow densities within 30 m of each pit, whereas Cameron Pass averaged 11. When compared to snow pit measurements, the Kovacs et al. (1995), Kuroiwa (1954), and Webb et al. (2021) equations derived densities yielded overall RMSEs of 54 kg m^{-3} (r = 0.09), 97 kg m^{-3} (r = 0.07), and 83 kg m^{-3} (r = 0.08), respectively (Figure 2.2; Table A3). Both the Kovacs et al. (1995) and Kuroiwa (1954) equations yielded densities with an overall negative bias, whereas the Webb et al. (2021) equation yielded densities with a positive bias (Table A3). However, the mean residual for the Kuroiwa (1954) derived densities was three times the mean residual of the Kovacs et al. (1995) derived densities. At Cameron Pass, the Kuroiwa (1954) RMSE was 25% lower than Kovacs et al. (1995; Table A3), but frequently yielded physically unrealistic snow densities (e.g., <50 kg m^{-3} on 10 February 2021). Therefore, we selected the Kovacs et al. (1995) equation to use at both Grand Mesa and Cameron Pass because of its overall lower RMSE and more physically realistic snow densities.

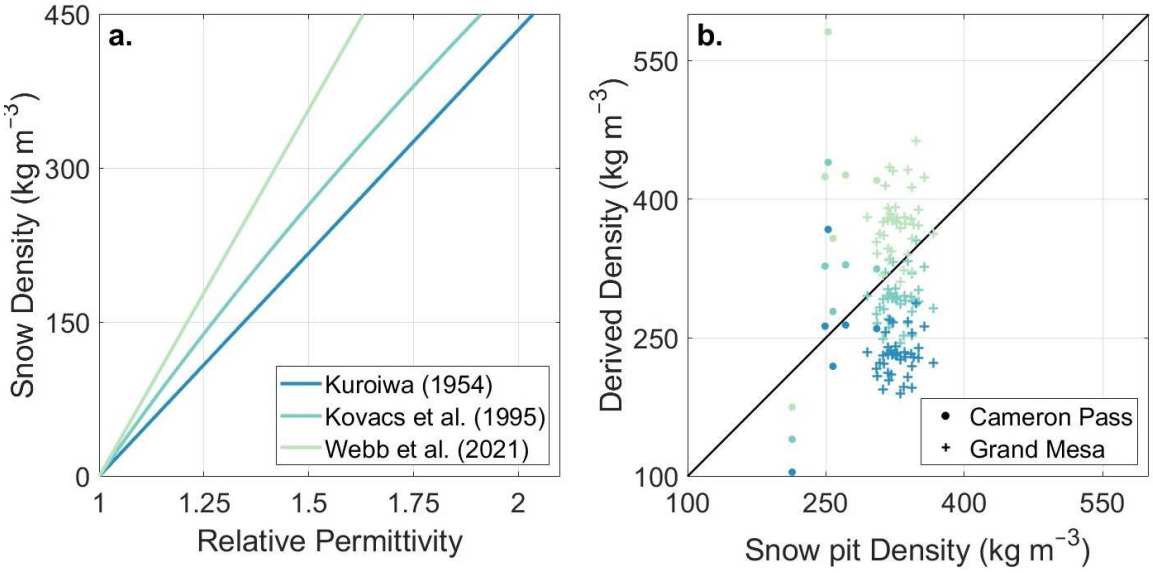

Figure 2.2: (a) Relative permittivity equations from Kuroiwa (1954), Kovacs et al. (1995), and Webb et al. (2021). (b) Median derived snow density (considering all values within 30 m of the snow pit) versus measured snow density. Snow densities were derived using the three relations (Equations 2.6–2.8) presented in panel (a).

We established survey-dependent uncertainty ranges for the derived relative permittivity and snow density datasets (Table A1) and found that the uncertainties in derived relative permittivity are more sensitive to snow depth *twt*. At lower mean snow depths (<1 m), the effect of the snow depth uncertainty is increased, and large relative permittivity uncertainties result, leading to unrealistic estimates (e.g., ε_s <1 and ε_s >88). The average uncertainty for densities derived from TLS (196 kg m^{-3}) is approximately twice the average for those derived from airborne lidar (88 kg m^{-3}). This is primarily due to the lower average snow depths observed at Cameron Pass and the larger snow depth uncertainty range for the TLS platform. Differences between GPR systems did not have a substantial effect on estimated *twt* uncertainty, likely because of the similar vertical resolutions (calculated as one fourth of the wavelength; Daniels, 2004) of the 1.6 GHz (~0.04 m) and 1.0 GHz (~0.06 m) systems.

A subset of lidar snow depths, *twt*, derived relative permittivities, and derived snow densities are shown for Grand Mesa, Cameron Pass, and Ranch Creek in Figure 2.3. Although

the full spatial extent of lidar and *twt* datasets are displayed, only snow depths that were used to derive relative permittivity values are discussed. All snow depth, *twt*, derived relative permittivity, and derived density datasets are plotted in Figures A3–A6. Results for Cameron Pass 2020 and 2021 are discussed as a time series. Although the Grand Mesa lidar was collected in sequential dates, Grand Mesa results are not treated as a time series because each week had a different region of interest for GPR surveys. An overview of the mean and standard deviations for each of the datasets can be found in Table A4.

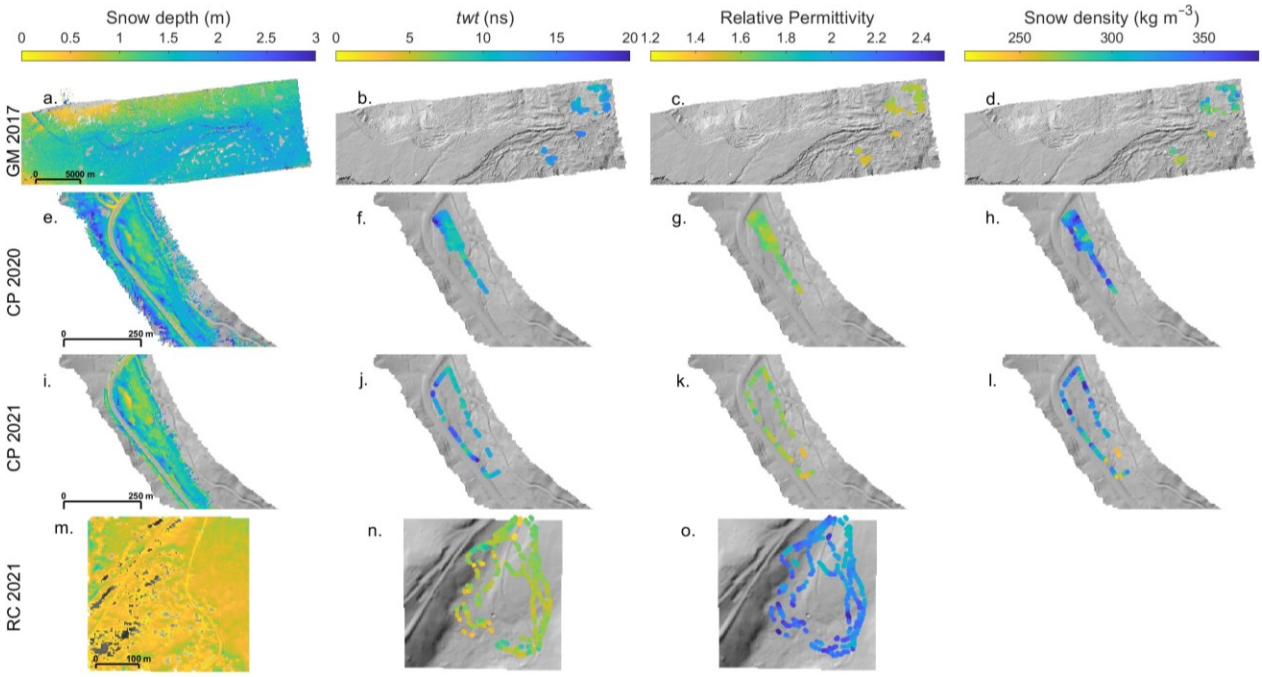

Figure 2.3: Examples from each field site and study year of the datasets used in this study. Rows are organized by field site, with (a–d) the 16 February 2017 Grand Mesa survey (GM 2017), (e–h) the 12 March 2020 Cameron Pass survey (CP 2020), (i–l) the 22 March 2021 Cameron Pass survey (CP 2021), and (m–o) the 7 April 2021 Ranch Creek survey (RC 2021). Columns are organized from left to right as snow depth, *twt*, relative permittivity, and snow density.

The lowest mean snow depth/*twt* at Grand Mesa was observed on forested transects on 8 February (1.19 m, 9.90 ns; Table A4), whereas the largest mean depth/*twt* was observed on open transects on 25 February (1.65 m, 13.55 ns). Forests exhibited lower mean snow depths and *twt*

(–0.16 m, –1.37 ns) compared with open environments, resulting in a negligible, but consistently lower average snow density (mean difference = –5 kg m^{-3}) in forested environments. Although this contrast is within the uncertainty range of our method, two-sample t-tests suggest a statistically significant difference between the mean snow densities in forests and open environments during 16 and 25 February ($p < 0.005$). Further, snow pit-measured bulk densities (n = 193; Elder et al., 2018) corroborate the contrast but reveal a somewhat lower average snow density for forests (mean difference = –11 kg m^{-3}). Forested and open relative permittivity and density standard deviations showed negligible differences for each survey date (±0.006, ±3 kg m^{-3}).

Mean snow depths at Cameron Pass for WY 2020 increased from 0.66 to 1.34 m, while mean *twt* increased from 5.42 to 11.39 ns (Table A4. The mean snow depth did not change between 26 February and 12 March, however, the mean derived relative permittivity increased from 1.539 to 1.632, corresponding to an increase in density from 284 to 328 kg m^{-3}. As snow depths and SWE increased, standard deviations for derived relative permittivity and snow density decreased, relative to the 18 December 2019 survey, by 37 % for the 26 February 2020 survey and by 56 % for the 12 March 2020 survey. During WY 2021, mean snow depths showed a more varied trend. From 10 to 24 February, the mean snow depth and *twt* exhibited negligible change (–0.06 m, +0.08 ns), but derived density increased by +89 kg m^{-3}. During this interval, snow pit depth declined by –0.14 m and bulk snow density increased by +40 kg m^{-3} and, on 24 February, snow pit observations noted a surface wind crust (~1 cm in height). These observations indicate that wind was a driving factor in the observed densification. Mean snow depths and *twt* increased between 24 February and 22 March (+0.34 m, +2.67 ns), but snow density decreased (–40 kg m^{-3}). This study year included a wet snow survey (27 May), where the mean snow depth

declined by 53 % relative to the 22 March survey. The mean and standard deviation of the 27 May relative permittivity (mean = 2.163, standard deviation = 0.444) were 1.3 and 2.5 times higher than the highest relative permittivity mean and standard deviation of the dry snow surveys (24 February 2021 mean = 1.695; 10 February 2021 standard deviation = 0.180).

The Ranch Creek survey explored the viability of UAV-borne lidar for snow depth retrieval in a shallower snowpack with both open and mixed conifer/deciduous forest cover. Derived relative permittivity uncertainty (0.418; Table A1) was within the range of relative permittivity uncertainties estimated for Cameron Pass surveys, despite having the lowest mean snow depth (0.62 m; Table A4). The mean relative permittivity value is only 0.043 less than the mean for the 27 May 2021 Cameron Pass survey, indicating similar mean LWC values for the two surveys, however, the standard deviation is much lower, indicating that LWC was more uniform in its distribution for the 7 April survey.

2.4.2 Spatial variability of derived snow density and relative permittivity

Exponential variogram models (Figure 2.4) and corresponding experimental variograms (Figures A7–A10), indicate that nugget effects, or variability at scales smaller than the first lag distance, are absent from the snow depth, *twt*, and relative permittivity variogram models. A minor nugget effect (<1 % of the overall variability) was estimated for the density variogram models, and a larger nugget effect (ranging from 2–7 % of the total variability) was estimated for the SWE variogram models. Absent or very low nuggets indicate relatively low spatial variability (<10 %) at the <10 m scale for these variables. Sills and correlation lengths are given for each of the variogram models in Table A5.

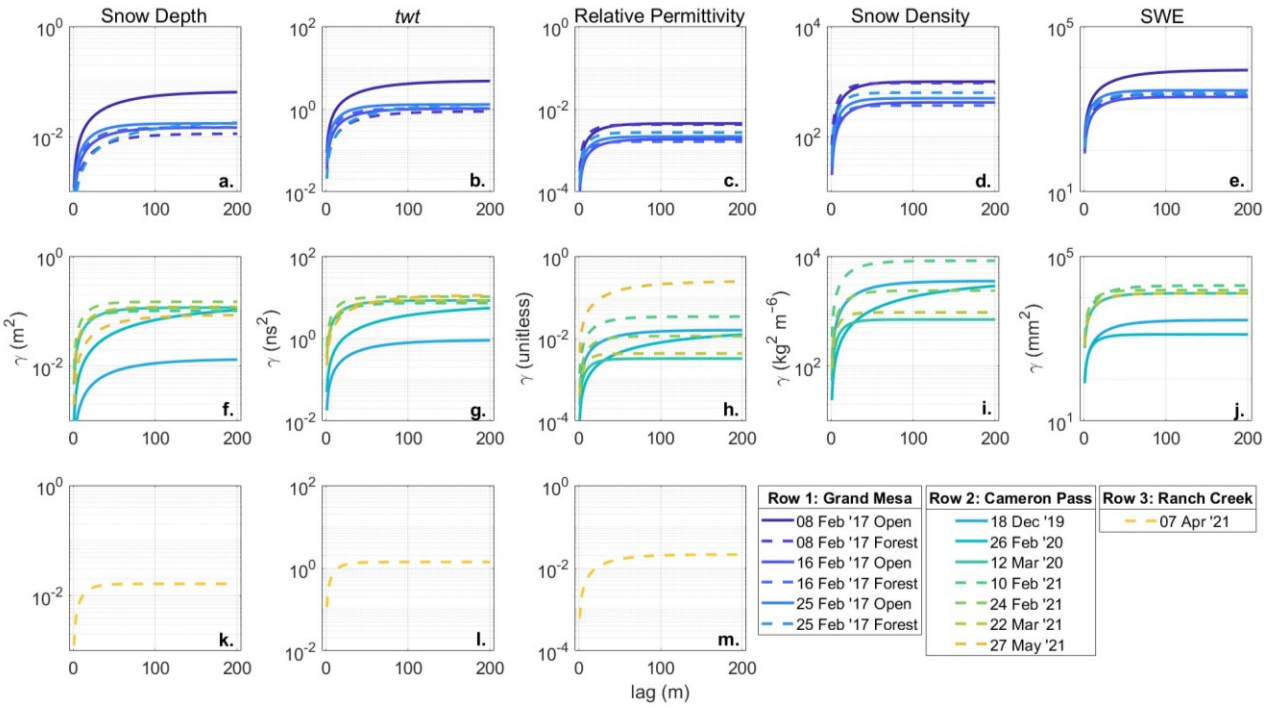

Figure 2.4: Exponential variogram models calculated from the best fit of the experimental variograms. Rows represent different field sites and are organized from top to bottom as (a–e) Grand Mesa, (f–j) Cameron Pass, and (k–m) Ranch Creek. Columns represent different variables and are organized from left to right as snow depth, *twt*, relative permittivity, snow density, and SWE.

Variogram analysis reveals longer correlation lengths for snow depth and *twt* at Grand Mesa in the forests than in the open, with forests having a median difference of +6 m for snow depth and +11 m for *twt* (Figure 2.4a–e; Table A5). However, relative permittivity, snow density, and SWE have longer correlation lengths in the open than in the forests, with open environments having a median difference of +7 m for relative permittivity and snow density and +3 m for SWE. At Cameron Pass, no parameters revealed an obvious relation with time for WY 2020, but relative permittivity and snow density correlation lengths for WY 2021 decreased from 24 m on 10 February to 10 m on 22 March. Subsequently, the correlation length for relative permittivity increased substantially to 55 m during the wet snow survey on 27 May. A longer correlation length was also observed for relative permittivity on 7 April at Ranch Creek (34 m). These are

two of the longest relative permittivity correlation lengths found in the study, indicating that wet snow may have longer correlation lengths for relative permittivity than dry snow.

2.4.3 Evaluation of density models

Spatially distributed snow densities at Grand Mesa and Cameron Pass enable an evaluation of snow density models across a range of dates and snow conditions (Figure 2.5a–c). Here, we use the derived densities as a benchmark for comparison with modeled densities. A comparison between modeled densities and in situ densities is available in Text A.4. Of the empirical models, J_{09} yielded the lowest RMSE at both Grand Mesa (RMSE = 16 kg m^{-3}) and Cameron Pass (RMSE = 43 kg m^{-3}), whereas M&P_{08} yielded large RMSEs at Cameron Pass (RMSE = 87 kg m^{-3}) and Grand Mesa (RMSE = 71 kg m^{-3}), and systematically underestimated snow density (mean difference = –75 kg m^{-3}). St_{10} consistently overestimated snow density (mean difference = +37 kg m^{-3}). S&F_{14} performed comparably to J_{09} at Cameron Pass. We found that the variability from empirically estimated snow densities was more limited compared to derived (Figure 2.5a), and that empirical model accuracy decreased in lower snow depth conditions. SNODAS densities at Grand Mesa yielded an RMSE (20 kg m^{-3}) that was comparable to J_{09}, whereas SNODAS densities yielded the lowest RMSE (32 kg m^{-3}) at Cameron Pass. Unscaled iSnobal densities for Cameron Pass in WY 2020 yielded the highest RMSE (119 kg m^{-3}), whereas rescaled iSnobal densities improved the RMSE by 20 kg m^{-3}. iSnobal density accuracy improved for the March surveys, where RMSEs were 20–60 % lower than the overall RMSE. For both unscaled and rescaled iSnobal densities, estimates exhibited a substantial negative bias (mean residuals: iSn_{un} = –85 kg m^{-3}, iSn_{re} = –67 kg m^{-3}).

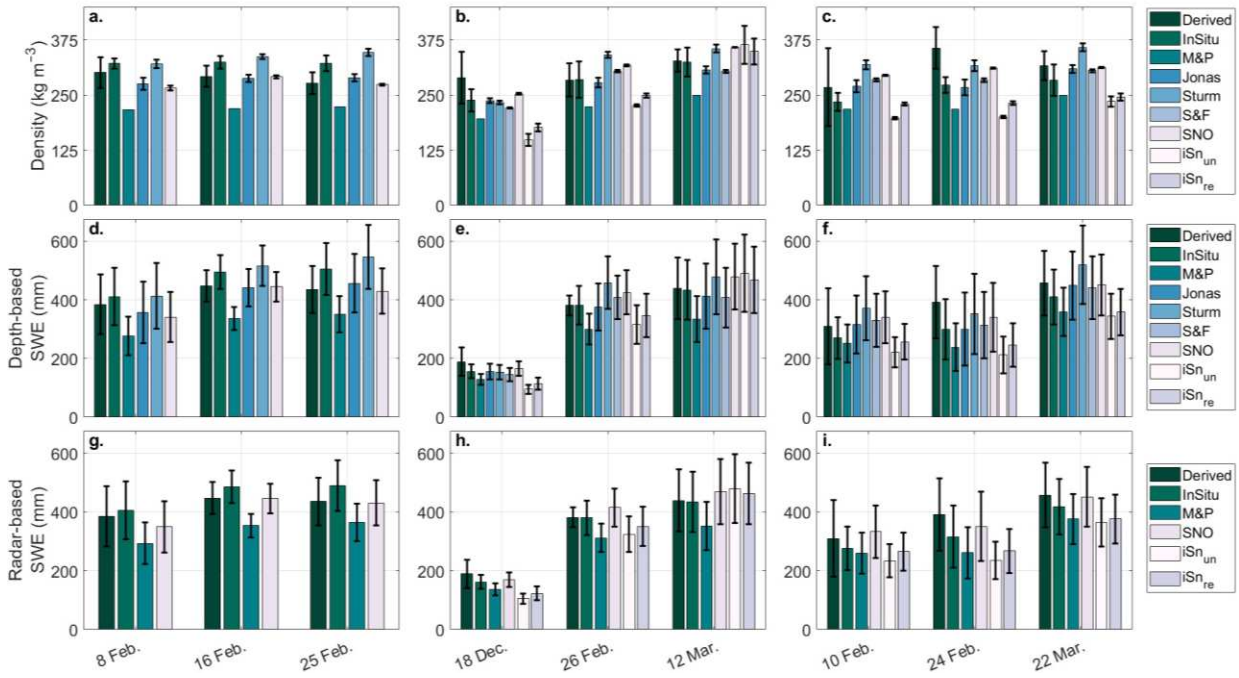

Figure 2.5: (a–c) Comparison between mean snow densities, (d–f) depth-based SWE, and (g–i) radar-based SWE estimated from the derived, in situ, and modeled densities. Depth-based SWE was calculated using lidar snow depths, whereas radar-based SWE was calculated using *twt*. Columns are organized by field site, from left to right: Grand Mesa surveys from WY 2017, Cameron Pass surveys from WY 2020, and Cameron Pass surveys from WY 2021. Error bars show ±1 standard deviation. Depth-based empirical density models cannot be incorporated into radar-based SWE calculations and are thus absent in g–i.

We then used the derived, modeled, and the mean of in situ densities to calculate depth-based SWE from the lidar-measured snow depths (Figure 2.5d–f) and radar-based SWE from the GPR-measured *twt* (Figure 2.5g–i). We considered the SWE calculated from derived densities as the benchmark for this analysis. J_{09} yielded the best performance for depth-based SWE estimates, estimating SWE within 10 % for seven of nine surveys, whereas unscaled iSnobal yielded the largest errors, estimating depth-based and radar-based SWE within 20% for only two surveys. $M\&P_{08}$ and rescaled iSnobal performed comparably: $M\&P_{08}$ yielded two depth-based SWE surveys within 20% and five radar-based surveys within 20%, whereas rescaled iSnobal estimated depth-based and radar-based SWE within 20 % for four surveys. $M\&P_{08}$ did not produce SWE estimates within 10% for any survey, but rescaled iSnobal improved density

estimates by an average of 7 % and estimated depth-based and radar-based SWE within 10% for two surveys. St_{10} estimated depth-based SWE within 10 % for three of nine surveys, but yielded estimates within 20 % for an additional five surveys. $S\&F_{14}$ performed comparably to J_{09} at Cameron Pass and estimated depth-based SWE within 10 % for four surveys. SNODAS yielded the best overall performance for radar-based SWE, estimating SWE within 10 % for eight of nine surveys, although its performance for depth-based SWE was reduced to four surveys within 10 %. We found that the average in situ density measurement yielded SWE within 10% for four of nine depth-based surveys and five of nine radar-based surveys.

2.5 DISCUSSION

2.5.1 Considerations for lidar-GPR surveys deriving relative permittivity and snow density

The combination of GPR and lidar for the derivation of snow densities or LWC is a promising method that could be employed to supplement in situ methods for both operational surveys and large-scale snow campaigns (e.g., NASA SnowEx). From our study, we can compare the combination of different lidar platforms with different GPR survey designs (e.g., TLS with a transect GPR survey) to suggest "best practices" for future studies. Combined lidar-GPR surveys for deriving relative permittivity need to consider the large uncertainty ranges that result from low snow depths (<1 m) and high snow depth uncertainty (>0.10 m; McGrath et al., 2022). We found that a spatial filter reduced the uncertainty range and yielded physically realistic densities, particularly when surveys were performed as grids or spirals. Spiral and grid surveys have the added potential of spatial modeling to estimate relatively complete maps of relative permittivity and snow density in the surveyed region (e.g., Meehan, 2022). Airborne lidar platforms yielded lower snow depth uncertainties (±0.05 to ±0.08 m; Table A1) than the TLS (±0.07 to ±0.22 m), but the TLS snow depth uncertainty could be reduced substantially by surveying from a stable

surface, rather than from a potentially shifting platform on the snow surface. Regardless of platform, we recommend that surveyors take careful notes regarding the GPR sled compression and the timing of the lidar collection relative to GPR surveys.

2.5.2 Comparison with previous studies

The local-scale spatial variability of snow density is time consuming to measure using traditional in situ sampling methods (López-Moreno et al., 2020). Therefore, snow density measurements tend to be sparser than other snow metrics, such as depth (Sturm et al., 2010), and thus density's spatial variability has seen few in situ studies. We found that the average range in derived densities at Grand Mesa (135 kg m^{-3}) and Cameron Pass (179 kg m^{-3}; Figure 2.3, S3–5) compare favorably to the ranges in snow densities measured by in situ studies conducted in the Spanish Pyrenees, where snow depths had a similar range to those measured in our study, but warmer temperatures led to rainfall during the winter of one study year (Fassnacht et al., 2010; López-Moreno et al, 2013). Density ranges up to 300 kg m^{-3} were observed from four snow density measurement campaigns conducted during accumulation (February 2010 and 2011) and around peak SWE (April 2010 and 2011) across three different locations ranging in elevation from 1517–3015 m (López-Moreno et al., 2013). Along a 5.4 km section of the Rio Esera in the Spanish Pyrenees, densities ranged from 350–450 kg m^{-3} in January 2009 (Fassnacht et al., 2010). The ranges reported by López-Moreno et al. (2013) fully encompass the maximum range observed in our derived density datasets, whereas Fassnacht et al. (2010) observed ranges more comparable to those we derived at Grand Mesa. It can be noted that, depending on the dominant processes, snowpack density can vary spatially at the 0.10 m scale (Fassnacht, 2021).

Several GPR-based methodologies have been developed to better understand the spatial distribution of snow densities and have increased the number of density estimates by two to three

orders of magnitude compared to in situ studies. However, GPR-based methodologies have generated snow density ranges that are physically unrealistic, especially when compared to in situ measurements. Velocity migration analysis has derived densities with a large range (100–500 kg m^{-3}) along relatively short (~100 m) transects in Wyoming's Medicine Bow Mountains (St. Clair & Holbrook, 2017), whereas multi-antenna pair GPR systems have derived densities as low as 150 kg m^{-3} during the melt season near Davos, Switzerland (Griessinger et al., 2018). Still, the multi-antenna pair methodology is promising; densities tended to range <80 kg m^{-3} for single ~100 m transects for Griessinger et al. (2018), whereas another multi-antenna pair GPR system was used to derive a narrow range (370–420 kg m^{-3}) along a 78 km transect across the Greenland Ice Sheet (Meehan et al., 2021). Our approach differs in that it integrates independently measured snow depths with *twt* to derive permittivity and density, similar to Yildiz et al. (2021), who derived densities by combining UAV SfM snow depths with GPR in the Ilgaz Mountains, Turkey, and McGrath et al. (2022), who conducted a time series of UAV SfM snow depth/GPR surveys along a 150 m transect at a field site adjacent to Cameron Pass during the 2021 study year. However, our use of a spatial filter reduced the derived snow density standard deviation (21–88 kg m^{-3}; Table A4) by a factor of two, relative to Yildiz et al. (2021) and McGrath et al. (2022). Although the overall RMSE for our study is still high, the RMSE at Grand Mesa (45 kg m^{-3}) is lower than either of the UAV SfM/GPR studies (68–74 kg m^{-3}) and derived density ranges are physically realistic. Thus, as this method is further developed and tested, it may be used to provide unprecedented detail on the spatiotemporal distribution of snow densities.

2.5.3 Spatial variability of snowpack parameters

Previous studies have shown that increases in average LWC are associated with larger LWC spatial variability and that radar-based methods for measuring SWE will have increased

uncertainty when LWC is present in the snowpack (Bonnell et al., 2021; Webb et al., 2022). Although we do not estimate LWC, we identify a large shift between dry and wet relative permittivity sills (Table A5), indicating that relative permittivity variance is higher for wet snow surveys. However, we found increased correlation lengths during wet snow surveys, which seems counterintuitive, given the complicated spatial and temporal variability of LWC. However, the increased correlation length indicates that modeling bulk volumetric LWC may be possible for field sites that have little topographic complexity, such as Cameron Pass, and could reduce the uncertainty of SWE retrievals from radar-based methods.

Median correlation lengths were nearly identical for *twt* (27 m) and snow depth (30 m) and were lower than probed snow depth correlation lengths measured by Anderson et al. (2014) in southwest Idaho (median correlation length = 46 m). At Grand Mesa, median correlation lengths for snow depth and *twt* were longer in the forests than in the open, corroborating the findings of McGrath et al. (2019), who also found longer correlation lengths for probed depths and GPR-derived snow depths in the forest, but our mean correlation lengths in the open were nearly four times longer. Snow density and relative permittivity variograms yielded a median correlation length of 19 m, which is about twice that observed by Yildiz et al. (2021) but is much smaller than what López-Moreno et al. (2013) observed (<150 m). Experimental variograms of derived densities in Grand Mesa forests exhibited cyclicity at the sill level (Figure A7), possibly due to the snow accumulation dynamics in the forest islands of Grand Mesa (Webb et al., 2020b). Sills for derived relative permittivity and density at Cameron Pass (Figure 2.4, S8–S9) tended to be high in December and February and decrease with accumulation, where higher sills may result from snowpack variability induced by topography and vegetation before the features are blanketed by snow.

2.5.4 Model performance and selection

Of the empirical models, J_{09} estimated densities and depth-based SWE with the lowest overall RMSE. St_{10} showed a consistent, positive bias (Figure 2.5), which was also noted by McCreight & Small (2014), largely due to the DOY parameter, which is less sensitive to short-term fluctuations in snow density than the month parameter used by J_{09}. We found that the DOY-based $M\&P_{08}$ systematically underestimated snow density and SWE at our sites, which could be improved for sites where calibration is an option (Pistocchi, 2016). J_{09} estimated depth-based SWE within 10 % for seven of the nine surveys and may represent a viable option for depth-based SWE remote sensing methods. Of the more complex models, SNODAS had a small negative bias across all surveys at Grand Mesa (overall mean residual = –14 kg m^{-3}) but exhibited no consistent bias for the Cameron Pass surveys, whereas unscaled and rescaled iSnobal densities were negatively biased for all Cameron Pass surveys (Figure 2.5). However, rescaling precipitation yielded improved iSnobal density estimates that exhibited lower RMSE (<50 kg m^{-3}) for WY 2020 surveys with deeper snowpacks (>1.30 m). Of all models, SNODAS yielded the most consistently accurate radar-based SWE (eight of nine surveys within 10 %) and the second most consistently accurate depth-based SWE (nine of nine surveys within 15 %), thus SNODAS may offer a suitable solution for snow density estimates in North America for both depth-based and radar-based methods.

Each evaluated model has known uncertainties. Empirical models are limited to a narrow, unrealistic range of density estimates (Raleigh & Small, 2017) and have been shown to decrease in accuracy with increased elevation (Avanzi & De Michele, 2015). Evaluations of SNODAS indicate that modeled SWE and snow depth have lower errors in subalpine regions (Clow et al., 2012; Dozier et al., 2016), but SNODAS tends to underestimate accumulation in deeper

snowpacks (Hedrick et al., 2015) and may be unsuitable in alpine regions, where snow deposition and redistribution processes are more complex (Dozier et al., 2016). Accurate forcing data are necessary for robust iSnobal model output, but the HRRR precipitation forcing data used in our study was consistently lower than Joe Wright SNOTEL SWE for WY 2020 and 2021 (Figure A11). For WY 2021, HRRR precipitation underestimated SWE by >50 %, which is a larger error than what Meyer et al. (2023) reported, and caused the substantially negative bias observed for estimated densities. Rescaling HRRR precipitation based on the 19 March 2021 Cameron Pass airborne lidar survey yielded more realistic spatial patterns for snow deposition but failed to generate accurate precipitation values at our field site, hence our introduced rescaling factor. Despite the higher RMSE values and biases, iSnobal remains a promising model for estimating snow densities, particularly where weather station coverage is sufficient or where HRRR precipitation is either accurate or can be corrected. As a final note, we found that lower SWE conditions (<300 mm) resulted in larger percent errors from models, increasing the J_{09} and SNODAS SWE errors to 18 % and 13 %, respectively. St_{10} and $S\&F_{14}$ yielded SWE errors as high as 23 %, whereas rescaled iSnobal SWE errors exceeded 30 %. Thus, further evaluation of modeled densities in lower snow conditions is warranted.

2.6 CONCLUSION

By combining GPR-measured *twt* with lidar-measured snow depths, we derived relative permittivity and snow density estimates along GPR transects at three sites during 11 surveys. For dry-snow surveys, this method yielded a mean RMSE of 54 kg m^{-3} (RMSE minimum = 45 kg m^{-3}, maximum = 92 kg m^{-3}, mean nRMSE = 0.18) compared with nearby in situ density measurements. At Grand Mesa, we observed that median correlation lengths for relative permittivity and density were 6 m longer in the open than in the forests, whereas at Cameron

Pass, correlation lengths decreased by 10 m over the span of 1.5 months. We observed that relative permittivity has a higher variance in wet snow than in dry snow, but correlation lengths were longer for the wet snow surveys. We compared derived densities with densities estimated from four empirical models, SNODAS, and iSnobal and found that J_{09} was the most accurate density model for depth-based SWE retrievals (±10 % for seven of nine surveys), whereas SNODAS densities yielded the most accurate SWE retrievals for radar-based methods (±10 % for eight of nine surveys). However, for lower SWE environments (<300 mm) uncertainty increased to >20 % for all models, which points to a potential issue in density modeling. Regardless, selecting an appropriate density model is difficult, and new models continue to be developed (e.g., Bisset et al., 2022; Meehan, 2022; Winkler et al., 2021). Empirical models evaluated in this study are directly applicable for depth-based SWE remote sensing methods and the Sentinel-1 co/cross-polarization backscatter method (Lievens et al., 2019, 2022), but site-specific calibration in both open and forested environments may improve results. Physically based models may be particularly powerful for InSAR methods of SWE retrieval, which can be applied over expansive regions (e.g., Oveisgharan et al., 2023) and require a surface density estimate to derive a change in SWE (Marshall et al., 2021), but these models are inherently limited by the chosen forcing data. With the increased availability of depth-based and radar-based remote sensing datasets, accurate density estimates are required to advance SWE remote sensing techniques. The accuracy and spatial coverage capabilities of the lidar-GPR snow density method makes it a promising avenue for model evaluation, training, and development.

3. EVALUATING L-BAND INSAR SNOW WATER EQUIVALENT RETRIEVALS WITH REPEAT GROUND-PENETRATING RADAR AND TERRESTRIAL LIDAR SURVEYS IN NORTHERN COLORADO[2]

3.1 INTRODUCTION

In snow-dominated watersheds, melt from seasonal snow drives streamflow and groundwater recharge (Li et al., 2017; Lorenzi et al., 2024). Globally, snowmelt supplies water resources for more than one-sixth of the population (Barnett et al., 2005). However, warming temperatures are decreasing the probability of snowfall in historically snow-dominated watersheds (Klos et al., 2014; McCrystall et al., 2021), shifting snowpacks to higher elevations and more poleward latitudes, and effectively decreasing the predictability of streamflow in these basins (Siirila-Woodburn et al., 2021). Mountains store a disproportionately large amount of snow despite comprising a small fraction of the global land surface (Wrzesien et al., 2019). Yet, in the mountains of the western United States, climate change has driven a 15–30% decline in snow water equivalent (SWE), the defining snowpack hydrologic variable, and SWE is expected to decline by an additional 25% by 2050 (Mote et al., 2018; Siirila-Woodburn et al., 2021). The projected changes are acute globally; by 2100, snowmelt is projected to decline in the European Alps by 50% (Moraga et al., 2021), while basins in the Himalayas may see snowfall declines of 30–70% for the warmest climate scenarios (Viste & Sorteberg, 2015). Although snowpack monitoring via automated stations exists in some countries (e.g., SNOTEL stations in the United States; Fleming et al., 2023), location bias, limited elevational range, and large spatial variability in snow over short length scales results in an incomplete characterization of this resource (Dozier

[2] Chapter under review and available as a preprint: Bonnell, R., McGrath, D., Tarricone, J., Marshall, H. P., Bump, E., Duncan, C., & Zheng, Y. (2024). Evaluating L-band InSAR Snow Water Equivalent Retrievals with Repeat Ground-Penetrating Radar and Terrestrial Lidar Surveys in Northern Colorado. *EGUsphere* [preprint], 1–33. https://doi.org/10.5194/egusphere-2024-236.

et al., 2016). Thus, satellite remote sensing methods for snowpack monitoring at high resolution (<500 m, <weekly) have been set as a high priority for study and development by the National Academies of Sciences, Engineering, and Medicine (National Academies of Sciences, Engineering, & Medicine, 2018).

The remote sensing of SWE is challenged by environmental factors (i.e., topography, vegetation) and by the spatiotemporally varying physical parameters of the snowpack (i.e., SWE, density, liquid water content, snow grain size). The NASA SnowEx Campaigns were conducted from 2017–2023 in the western United States to evaluate and develop remote sensing methods for snowpack monitoring, with the retrieval of SWE set as a primary goal (Durand et al., 2018). SWE is calculated as the product of snow depth and snow density, and there are two primary groups of techniques for remote sensing of SWE at high spatial resolutions (<500 m): i) depth-based optical-infrared methods and ii) radar-based methods. Depth-based optical-infrared methods (e.g., stereo satellite imagery, lidar) require cloud-free conditions and derive snow depths by differencing a snow-off digital elevation model (DEM) from a snow-on DEM (Currier et al., 2019; Hu et al., 2023). Snow density model estimates or in situ measurements are required to convert the snow depths to SWE (e.g., Hedrick et al., 2018), which adds to the uncertainty of this technique (Raleigh & Small, 2017). Both satellite lidar (e.g., Besso et al., 2024) and very-high resolution stereo satellite imagery (e.g., Hu et al., 2023) are being explored as depth-based methods for the remote sensing of SWE. Radar approaches are distinct from depth-based approaches because the radar signal penetrates the snowpack. Satellite radar approaches for snow depth and SWE retrievals are implemented from synthetic aperture radar (SAR) platforms and the techniques for snow depth and SWE remote sensing are primarily grouped into backscatter approaches, which use the amplitude component of the radar signal to derive snow depth and/or

SWE, and time-of-flight approaches, which derive SWE from the signal path length and includes SAR interferometry (InSAR). A third approach, which uses the co-polar phase difference, has also been tested. Readers interested in the co-polar phase difference methodology are referred to Leinss et al. (2014) and Patil et al. (2020).

Unlike optical-infrared methods, SAR approaches for snow remote sensing are not limited by cloud cover, primarily due to low atmospheric absorption at radar frequencies (Woodhouse, 2017). For SAR backscatter approaches, the radar signal is transmitted through the snowpack, and the signal is backscattered to the sensor via volume scattering from snow grains and rough scattering from the snow-ground interface (Tsang et al., 2022). Early backscatter work found that combined X- (8–12 GHz, ~3 cm wavelength) and C-band (4–8 GHz, ~5 cm wavelength) SAR was capable of measuring snow depths from 0.5–2.5 m (RMSE = 0.34 m; Shi & Dozier, 2000). More recent efforts have emphasized combined X- and Ku-band (12–18 GHz, ~1.8 cm wavelength) SAR; these backscatter approaches are promising methods for measuring SWE in shallow snowpacks (<150 mm; Tsang et al., 2022), with the potential for retrieving SWE in deeper conditions (Borah et al., 2023). C-band backscatter approaches are capable of measuring snow depths in deeper snowpacks (>1 m), albeit with higher uncertainty (Lievens et al., 2019, 2022). Backscatter approaches have known uncertainties in wet snow conditions, at large incidence angles, and in forests (Lievens et al., 2022; Tsang et al., 2022). InSAR is a unique method for retrieving SWE because the interferometric phase change has a near linear relation to SWE change (Guneriussen et al., 2001). In dry snow, this characteristic can be used to retrieve changes in SWE without a priori information on snowpack density with an estimated 7% uncertainty related to the linear approximation (Leinss et al., 2015). Applying the InSAR technique at low-frequency (e.g., L-band, ~25 cm wavelength) limits interaction between the

radar signal and snow grains, increases the signal penetration in forests and in wet snow (Naderpour et al., 2022), and promotes increased coherence (described below) over longer temporal baselines (Ruiz et al., 2022). A review of the transmissibility of L-band radar in snow is provided in Appendix B.1. With the upcoming launches of L-band SAR satellites, such as the NASA-ISRO SAR satellite (NISAR), the Radar Observing System for Europe satellite (ROSE-L), and the Tandem-L Interferometric Radar Mission, radar products will be publicly available at high spatial and temporal resolution across the globe (NISAR: 80 m spatial resolution, 12-day repeat; ISRO Space Applications Centre, 2023).

InSAR is a change detection method that measures the phase change between repeat SAR acquisitions and relies upon a coherent reflection from the snow-ground interface (Guneriussen et al., 2001; Appendix B.2). The InSAR SWE retrieval technique was first established at C-band from the European Remote-Sensing Satellite (ERS) platform at a field site in Norway. The study showed that snowfall could be mistaken as a deformation signal in interferograms (the interferometric phase change data product; Guneriussen et al., 2001). Deeb et al. (2011) applied this technique to the ERS satellite using repeat acquisitions during an accumulation season to measure changes in SWE (ΔSWE) at a site on the North Slope of Alaska, United States that revealed ΔSWE spatial patterns correlated with the prevailing wind direction. Since then, the technique has been tested for multi-year, season-long ΔSWE retrievals from a tower mounted platform in Finland at Ku-, X-, C-, and L-band frequencies (Leinss et al., 2015; Ruiz et al., 2022), by several studies emphasizing one or two interferometric pairs (Conde et al., 2019; Marshall et al., 2021; Nagler et al., 2022; Palomaki & Sproles, 2023; Tarricone et al., 2023), and by two season-long studies that used a time series of interferometric pairs (Hoppinen et al., 2024; Oveisgharan et al., 2024). In general, these studies have found that InSAR ΔSWE retrievals are

highly correlated with in situ measurements, but accuracy has varied on a case-by-case basis and in situ measurements for evaluation have been limited to point-based measurements that likely do not capture the spatial complexity of the snowpack. Additionally, only three of these studies have considered atmospheric signal delays, which represent a source of uncertainty because changes in atmospheric pressure and water content can further affect the ΔSWE retrieval accuracy (Gong et al., 2013).

Here, coherence refers to the complex interferometric coherence and is a measure of the similarity of the backscattered radar signal properties between two acquisitions (Woodhouse, 2017). Coherence is considered an index for confidence in phase change measurements, where phase changes with higher coherences are considered more accurate, and coherence must be maintained for the accurate unwrapping of interferograms. Coherence is affected by forest cover, changes in soil conditions (e.g., soil moisture changes or freeze-thaw changes), changes in the dielectric permittivity of the snowpack (e.g., melt-refreeze cycles), snow metamorphism (Brangers et al., 2023), and significant snow accumulation/ablation events (Ruiz et al., 2022). Collectively, these factors indicate that as the temporal baseline (i.e., time interval) between interferometric pairs is extended and/or major snowpack changes occur, coherence will degrade (Deeb et al., 2011), particularly at higher frequencies (Ruiz et al., 2022). A review of the calculation of coherence is provided in Appendix B.2.

Here, we calculated ΔSWE retrievals from 10 L-band NASA Uninhabited Aerial Vehicle SAR (UAVSAR; Rosen et al., 2006) InSAR pairs collected during the NASA SnowEx Time Series campaigns in 2020 and 2021 over north-central Colorado. During UAVSAR acquisitions, we collected spatially distributed ground-penetrating radar (GPR) at a very similar frequency to UAVSAR (UAVSAR = 1.26 GHz, GPR = 1.0 GHz) for all InSAR pairs, and we performed

terrestrial lidar scans (TLS) for two InSAR pairs. Our study examines three components of InSAR ΔSWE retrievals. First, we leveraged our ground observations to evaluate the accuracy of the L-band InSAR technique for ΔSWE retrievals for two accumulation seasons in a dry continental subalpine snowpack. We then evaluated UAVSAR ΔSWE retrieval errors against coherence to examine it as a potential metric for ΔSWE retrieval accuracy. Finally, UAVSAR ΔSWE retrievals are summed across each individual winter season and compared with total SWE measured at seven automated stations to evaluate the accuracy of the technique across a time series.

3.2 OVERVIEW OF SNOWEX 2020 AND 2021 AT CAMERON PASS, COLORADO

The SnowEx 2020 Time Series campaign was originally planned for a single season at 13 field sites (Marshall et al., 2019), but was cut short due to the COVID-19 pandemic and subsequently restarted in 2021 at seven field sites. Weekly to bi-weekly surveys were performed at Cameron Pass, Colorado (Figure 3.1a), coinciding with UAVSAR flights (Table 3.1). The flight line was typically ~40 km in length with a swath width of 16 km, but deviations from the spatial baseline and poor GNSS accuracy caused data acquisitions to be shortened for a few dates. The primary flight heading was southeast (141°), with a secondary northwest heading (321°) flown when time allowed. For the analysis, we used the 141° heading for all InSAR pairs except the 27 January to 3 February 2021 interval, which used the 321° heading.

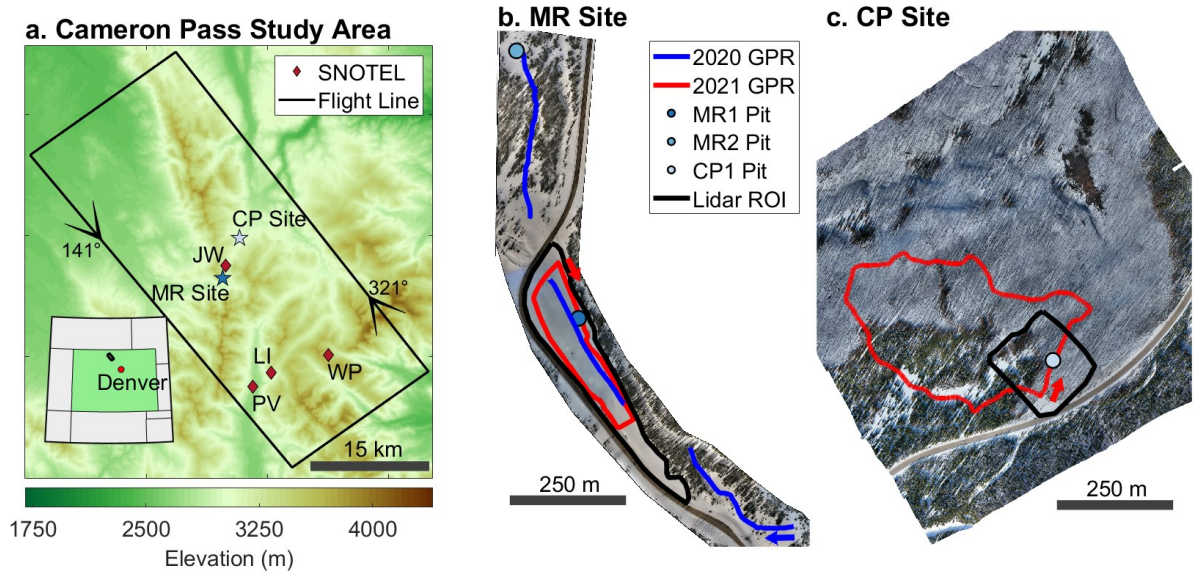

Figure 3.1: (a) Cameron Pass study area showing the Rocky Mountains, CO UAVSAR flight line overlaid on the Copernicus DEM (European Space Agency, 2021) with flight headings indicated by arrows. Locations are given for the Michigan River (MR) field site, Cameron Peak (CP) field site, and the Joe Wright (JW), Willow Park (WP), Lake Irene (LI), and Phantom Valley (PV) SNOTEL stations. Inset depicts the location of the flight line in Colorado. Middle and right panels show uncrewed aerial vehicle (UAV) imagery collected during March 2020 at the (b) MR field site and February 2021 at the (c) CP field site. The MR field site was surveyed during 2020 and 2021, whereas the CP field site was only surveyed during 2021. Key study areas, including snow pit locations, GPR transects, and terrestrial lidar regions of interest (Lidar ROI) are plotted. Arrows indicate the starting location and travel direction of the GPR transects.

Table 3.1: UAVSAR flight dates and times, field survey dates, GPR survey times, and ground observations performed for each field survey date. For instances where both the 141° and 321° flight headings were used, flight times are given for both. Otherwise, only flight times for the 141° heading are listed. For 2021, GPR survey times are given for the Michigan River (MR) and the Cameron Peak (CP) field sites. Ground observations include GPR, TLS, snow pits (SP), and probed depths (PD).

UAVSAR Flight Dates	**UAVSAR Flight Time (Local)**	**Field Survey Dates**	**GPR Survey Time (Local)**	**Ground Observations**
12 February 2020	11:10	12 February 2020	12:06	GPR, SP, PD
19 February 2020	11:42	19 February 2020	11:11	GPR, SP, PD
26 February 2020	11:24	26 February 2020	14:55	GPR, TLS, SP, PD
12 March 2020	10:54	11 March 2020	9:51	GPR, TLS, SP, PD
15 January 2021	10:43	15 January 2021	11:12 (MR), 14:49 (CP)	GPR, SP, PD
20 January 2021	12:20	20 January 2021	11:18 (MR), 15:33 (CP)	GPR, SP, PD
27 January 2021	11:52 (141°), 11:35 (321°)	27 January 2021	11:27 (MR), 15:21 (CP)	GPR, SP, PD
3 February 2021	10:51 (141°), 10:34 (321°)	2 February 2021	10:52 (MR), 14:01 (CP)	GPR, SP, PD
No flight	-	10 February 2021	-	TLS, SP
23 February 2021	15:50	24 February 2021	10:59 (MR), 14:34 (CP)	GPR, TLS, SP, PD
3 March 2021	9:13	3 March 2021	11:05 (MR), 14:43 (CP)	GPR, SP, PD
10 March 2021	8:46	9 March 2021	11:01 (MR), 13:29 (CP)	GPR, SP, PD
16 March 2021	9:03	18 March 2021	10:14 (MR), 14:24 (CP)	GPR, SP, PD
22 March 2021	8:43	22 March 2021	10:31 (MR), 14:12 (CP)	GPR, SP, PD

The region has a continental snow climate (e.g., Trujillo and Molotch, 2014), with a prairie snowpack at lower elevation (<2800 m) within the North Park region and montane and alpine snowpacks in the higher elevation Medicine Bow Mountains and Never Summer Range. Four SNOTEL stations and three automated stations that measured snow depth were located within the flight line (Figure 3.1a). The Joe Wright SNOTEL station, which was within 1.5 km of

our field sites, receives a median peak SWE of 632 mm that occurs on a median date of 5 May (1979–2023). Vegetation within the flightline primarily consists of evergreen forest (58%) and shrubs (32%; Buchhorn et al., 2020). Engleman spruce (*Picea engelmanii)*, subalpine fir (*Abies lasiocarpa*), and lodgepole pine (*Pinus contorta*) are the primary constituents of the forest, with interspersed Aspen (*Populus tremuloides*) groves (Fassnacht et al., 2018). From August to November 2020, the Cameron Peak fire burned >80 km^2 of the flight line, including the Cameron Peak field site (CP; Figure 3.1a) region (McGrath et al., 2023), which is not accounted for in these land cover estimates.

During SnowEx 2020, we surveyed the Michigan River field site (MR; Figure 3.1b), located in mostly open meadows vegetated by willows and grasses, though spruce/fir forests with <70% canopy cover inhabited portions of the northern and southern extent of the GPR transects. We measured stratigraphy, density, snow depth, and snow temperature in two snow pits (MR1, MR2; Figure 3.1b), following the SnowEx methodology outlined by Mason et al. (2023). Interval boards, which captured snow accumulation between surveys, were installed within 10 m of MR1 and at the nearby Joe Wright SNOTEL station. We recorded new snow depth, SWE, and density at each interval board on each site visit. Repeat GPR surveys (~1.6 km in length; McGrath et al., 2021) were performed using a Sensors & Software PulseEkko 1.0 GHz GPR coupled to the snow surface via a sled and pulled behind and to the side of a snowshoer. Snow depths were probed every ~3 m along the GPR transect. Two snow-on terrestrial lidar scans were performed on 26 February and 12 March 2020, in addition to a snow-off UAV-borne lidar scan performed in August 2020 (Williams, 2021).

For SnowEx 2021, we expanded our surveys to include the Cameron Peak field site (CP; Figure 3.1c). At MR, GPR surveys (0.8 km in length; Bonnell et al., 2022) were altered to form a

loop around the primary meadow, with a co-located snow pit (MR1) and interval board. Snow pits and interval boards were surveyed following the SnowEx methodology. Snow depths were manually probed along the eastern portion of the GPR transect at ~5 m intervals. We expanded to CP to leverage the reduced vegetation due to the Cameron Peak fire. CP has severely burned spruce/fir forest to the north and east, with an unburned stand in the central to southern portion (Figure 3.1c). A single snow pit and interval board was surveyed near the GPR transect (1.6 km in length) in the burned section. Snow depths were probed every ~5 m along the southeastern GPR transect, with ~200 m in the forest and ~200 m in the burned area. An automated station was installed near the CP snow pit, which measured snow depth, wind speed and direction, radiation, temperature, and soil moisture. Two snow-on terrestrial lidar scans were performed at both field sites on 10 February and 24 February 2021, with a snow-off terrestrial lidar scan performed on 27 May 2021 at CP (Williams, 2021).

3.3 METHODS

3.3.1 UAVSAR processing

Here, we provide an overview of the key UAVSAR processing steps. For additional and more detailed information, we direct readers to Appendix B.1–B.2. During the 2020 and 2021 airborne campaigns, UAVSAR deployed a fully polarized L-band (1.26 GHz center frequency, 0.24 m wavelength), 80 MHz bandwidth, left-looking InSAR. The instrument was flown at an altitude of ~12,500 m and acquired data along a ~40 km stretch with a 16 km swath width (area = ~640 km2; Figure 1a; NASA UAVSAR, 2023). In 2020, overpasses were performed with a temporal baseline of seven days for the first three acquisitions (12, 19, & 26 February) and 15 days for the final acquisition (12 March). In 2021, overpasses had varying temporal baselines (typically five to eight days) and due to other aircraft commitments, one acquisition had a longer baseline (20 days for 3–23 February). Poor coherence prevented phase unwrapping at the field

sites for one InSAR pair (10–16 March 2021). The UAVSAR team at the NASA Jet Propulsion Laboratory processed the UAVSAR data and generated geocoded amplitude, interferogram, unwrapped interferogram, and coherence products at ~5 m spatial resolution. We accessed the products from the Alaska Satellite Facility (ASF; NASA UAVSAR, 2020, 2021) and converted the products to geotiffs using uavsar_pytools (Hoppinen et al., 2022). InSAR measures phase deformation within a single ±π radians phase cycle, which equates to about ±108 mm SWE. Interferograms where ΔSWE exceeded a full phase cycle for some pixels require unwrapping for the accurate estimation of ΔSWE. Therefore, we focused on the unwrapped interferogram and coherence products, and outline key workflow steps for calculating ΔSWE, rather than total SWE, in Figure 3.2. Although we included all four polarizations, we present the horizontal-transmit/horizontal-receive polarization (HH) for all intervals except the 3–23 February 2021 interval, which used the vertical-transmit/horizontal-receive polarization (VH) due to incomplete phase unwrapping in the HH data product. Detailed radar SWE retrieval methodology is outlined in Appendix B.2.

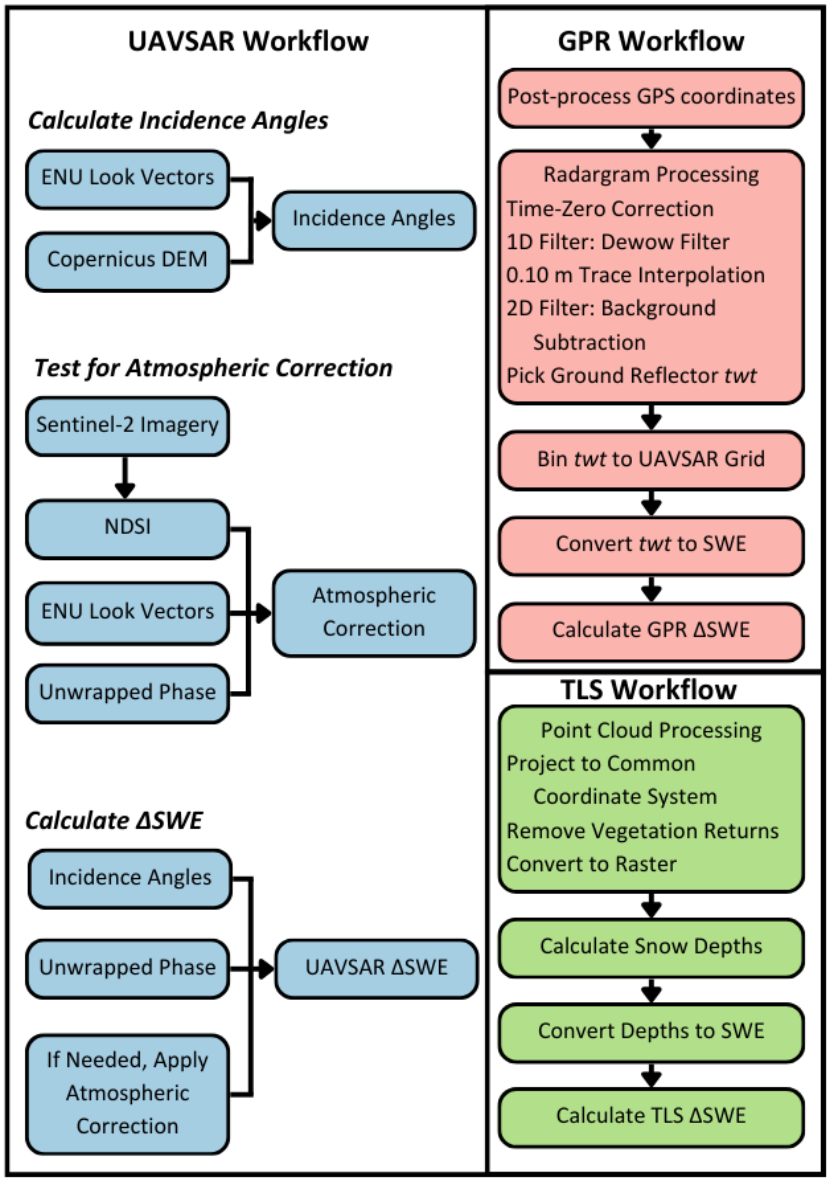

Figure 3.2: Workflow diagrams for deriving ΔSWE from UAVSAR, GPR, and TLS products. For simplification, UAVSAR workflow is described in three steps. ENU indicates the east, north, and up look vectors provided by UAVSAR.

We tested for atmospheric delays following methods developed by Tarricone et al. (2023). We identified snow-free pixels in the unwrapped interferograms using the normalized difference snow index (NDSI; Dozier, 1989) calculated from Sentinel-2 imagery (European Space Agency, 2022; Figure B1) and regressed snow-free unwrapped phase pixels against the corresponding signal path lengths. Importantly, this method assumes that snow-free pixels are

not undergoing any physical changes that would lead to a phase change. We tested whether an atmospheric correction was needed using three criteria outlined in Appendix Text B.2.2. Importantly, no unwrapped interferograms met all three criteria (Table B1). Therefore, we did not apply any atmospheric corrections because we concluded that stratified atmospheric artifacts are either limited for all interferometric pairs or were more complicated than what our linear model identified. See Appendix Text B.2.2 for a more detailed description of the atmospheric correction.

For these flights, UAVSAR had average look angles of 26–70° from near to far range. We calculated incidence angles in uavsar_pytools (Hoppinen et al., 2022; Equation B4) from the Copernicus 30 m DEM (rescaled to the UAVSAR grid) and the UAVSAR-provided look vector. The Copernicus DEM was chosen because it is the primary DEM used within the processing flow of ASF HyP3 and will be the basis for NISAR interferometric products. We evaluated incidence angles derived from the Copernicus DEM and the ΔSWE retrieval uncertainty caused by these incidence angles in Appendix B.2.5.

UAVSAR acquisitions were collected during the winter over relatively short temporal baselines (< 21 days). Therefore, we consider changes at the snowpack surface to be the primary driver of phase deformation in the unwrapped interferograms, but we provide a discussion of other potential sources of phase deformation in Appendix B.2.1. Changes at the snow surface may include new snow accumulation, sublimation, redistribution, or melt. For both study periods, we conclude that the snowpack is dry, based on results presented in Section 3.4.1. Thus, for ΔSWE retrievals, we consider only the density of snow that accumulated between UAVSAR acquisitions. Surface densities were estimated by averaging density measurements of the snow that accumulated on the interval boards between UAVSAR acquisitions (Section 3.3.2). For

instances where snow accumulation had occurred but had been removed from the interval board by, for example, wind redistribution, we used an average of the uppermost 10 cm of the snow pit-measured densities. For each interferometric pair, we converted surface densities to relative permittivity (Equation B5). Relative permittivities, unwrapped phase, and incidence angles were then used to calculate snow depth changes (Equation B6), which were subsequently converted to ΔSWE using the surface snow density (Equation B7). The InSAR technique for ΔSWE retrievals is relatively insensitive to an input density. For example, a higher input snow density results in a lower radar velocity and a lower change in snow depth, but the higher input snow density is used to convert the estimate to ΔSWE, resulting in an uncertainty of <7% (e.g., Hoppinen et al., 2023). Because InSAR phase is relative (Woodhouse, 2017), we estimated absolute phase as the median difference between a 20% set of randomly selected GPR ΔSWE retrievals (Section 3.3.2) and coincident UAVSAR ΔSWE retrievals for each interval. The median differences were then subtracted from the UAVSAR ΔSWE retrievals for each interval and the 20% of the GPR observations used in this step were removed from subsequent analyses. Finally, we supplemented our analysis by evaluating an InSAR ΔSWE retrieval method that approximates ΔSWE from the InSAR phase change and the incidence angle (Leinss et al., 2015) and is thus independent of snow density and relative permittivity measurements. The methods and results of this analysis are reviewed in Appendix B.2.4.

UAVSAR coherence values from corresponding TLS and GPR pixels were used to evaluate coherence as a measure of noise for ΔSWE retrievals. Coincident GPR and UAVSAR ΔSWE retrievals were binned by coherence and the root mean squared error (RMSE) of the UAVSAR ΔSWE retrievals was calculated for each bin. The effect of temporal baseline upon coherence and UAVSAR ΔSWE retrieval accuracy was then evaluated by calculating the median

coherence and RMSE for UAVSAR ΔSWE retrievals across all temporal baselines used in this analysis.

3.3.2 Processing ground-based measurements

3.3.2.1 In situ measurements

Key in situ measurements included in this research are snow pit temperatures, pit-measured densities, pit-measured depths, interval board densities and SWE, and manually probed depths. Pit-measured temperatures were used to detect the possible presence of liquid water within the snowpack. Pit-measured densities were averaged to estimate bulk density, which was used in SWE calculations for the snow pits, GPR, TLS, and probed depths. Interval board densities were used for ΔSWE calculations in the UAVSAR workflow, however, for some dates, the interval boards yielded little-to-no accumulation due to wind redistribution or a lack of precipitation. For these dates, the pit-measured densities from the upper 0.10 m of the snowpack were averaged and used in the UAVSAR workflow. Probed depths were not repeated in identical locations but were geocoded using a Geode GNS2 receiver mounted on top of the probe and converted to SWE using the bulk snow densities. Because the probed depths had a sampling of 1–2 measurements per UAVSAR pixel and were not collected in repeated locations, we use the depth probe dataset to evaluate the GPR and TLS SWE accuracy, rather than evaluating the UAVSAR ΔSWE retrievals directly.

3.3.2.2 GPR

GPR locations were collected via an Emlid RS2 GNSS receiver onboard the GPR sled and post-processed with an Emlid base station located at the MR field site to ensure a spatial accuracy of <0.25 m. High accuracy is important, given that these transects were repeated and the product of interest is ΔSWE, which is sensitive to geolocation errors. Radargrams were processed in ReflexW (Sandmeier, 2019) in four general steps: (1) apply time-varying time-zero

correction, (2) one-dimensional de-wow filter to remove low-frequency noise, (3) trace interpolation to ~0.10 m, and (4) two-dimensional filter to remove instrument noise. After processing the radargrams, the ground reflector, identified as the highest magnitude positive amplitude reflector at depth, was picked and its corresponding two-way travel time (*twt*), representing the time-of-flight through the snowpack, was exported. Further GPR collection and radargram processing details are presented in McGrath et al. (2021) and Bonnell et al. (2022). Bulk snow density was then estimated as the average bulk density between available snow pits and used to estimate bulk relative permittivity (Equation B5) and, thereby, the velocity of the radar signal (Equation B9). Using the estimated velocity, we converted *twt* to SWE (Equations B10, B7). A detailed summary of the GPR theory and methods is provided in Appendix B.3. We evaluated the accuracy of GPR SWE retrievals through a comparison with SWE from probed depths by calculating the median GPR SWE retrieval within a 1.5 m radius around each probed depth. GPR SWE retrievals were then binned at the spatial resolution of the UAVSAR grid by taking the median value of all points within each grid cell. SWE retrievals from corresponding dates were then differenced to generate GPR ΔSWE. The GPR workflow is summarized in Fig. 2.

3.3.2.3 Lidar Scans

Repeat snow-on terrestrial lidar scans were performed in 2020 on 26 February and 12 March at the MR site and in 2021 on 10 February and 24 February at the MR and CP sites. Snow-off lidar scans include a UAV-borne lidar scan that was performed for the MR site in August 2020 and a terrestrial lidar scan performed for the CP site on 27 May 2021. Terrestrial lidar scans were aligned and georeferenced by UNAVCO, Inc. (Williams, 2021). The USGS processed a bare-earth digital elevation model (DEM) from the UAV-borne lidar scan (Bauer et al., 2023). Lidar point clouds were reprojected and surface or bare ground returns were

classified. These points were then converted to rasters, gridded and aligned to the UAVSAR grid, using the average elevation value per pixel. We derived snow depths for each snow-on scan date by subtracting snow-free rasters from snow-on rasters. Snow depth rasters were converted to SWE using the bulk density from the snow pits. ΔSWE was calculated for 26 February to 12 March 2020 and for 10–24 February 2021 by differencing the corresponding SWE rasters. To align TLS datasets with the 3–23 February 2021 InSAR pair, we subtracted the SWE measured on the interval board between 2–10 February 2021 from the UAVSAR ΔSWE retrievals. TLS ΔSWE was then directly compared with the UAVSAR ΔSWE retrievals. The terrestrial lidar workflow is summarized in Figure 3.2.

3.3.3 Comparison between UAVSAR and automated stations

We obtained daily observations of snow depth, SWE, and air temperature from the Joe Wright SNOTEL station (ID 551) and daily observations of SWE from an additional three SNOTEL stations within the UAVSAR swath for the 2020 and 2021 seasons (Figure 3.1a; Table B2). Daily snow depths were obtained from three automated stations (two with sonic sensors and one with a snow stake paired with a time-lapse camera) within 4.5 km of the Joe Wright SNOTEL station (Table B2). We converted the snow depths to SWE by calculating density from Joe Wright SNOTEL station measurements of SWE and snow depth. SWE estimates were then smoothed with a five-day moving median filter to reduce the effects of new snow settlement.

We expanded our UAVSAR analysis beyond our relatively small field sites (~0.2 km^2 total area) to include measurements from the four SNOTEL stations and three automated stations within the swath (Table B2). We calculated the median UAVSAR ΔSWE within a 3×3 pixel grid (~15 m x ~15 m) around each station, added the ΔSWE retrievals for each interval, and matched the ΔSWE time series to the station time series by adding the station's SWE at the start of the UAVSAR flights to the UAVSAR ΔSWE time series. Because of spatially extensive missing data

within the 10–16 March 2021 interferometric pair, we adjusted the UAVSAR ΔSWE time series at each station with the ΔSWE measured by the station. Median coherence was calculated within each 3×3 grid for the SNOTEL stations to evaluate the effects of coherence upon the ΔSWE retrieval time series. Last, station-measured SWE was compared with cumulative InSAR SWE for the final dates of the 2020 and 2021 UAVSAR acquisitions.

3.4 RESULTS

3.4.1 Field observations of SWE and snow density

UAVSAR flights coincided with 117 mm of SWE accumulation (18% of peak SWE; Figure 3.3a) during the 2020 campaign (4 weeks) and 282 mm of accumulation (48% of peak SWE; Figure 3.3b) during the 2021 campaign (9 weeks). SWE at the in situ interval boards increased on average by 34 ±12 mm and 31 ±29 mm per flight interval during the 2020 and 2021 campaigns, indicating that ΔSWE at the field sites was likely within a full phase cycle (±108 mm; Appendix Text B.2.3) for most UAVSAR acquisitions. New snow density, used for UAVSAR ΔSWE calculations, ranged between 106 and 145 kg m^{-3} across all study dates in 2020 (Figure 3.3c), and over a larger range, 118–219 kg m^{-3}, in 2021 (Figure 3.3d). Bulk density, used for GPR and TLS SWE calculations, increased minimally between most flights (mean = +20 kg m^{-3}; Figure 3.3c–d), with a notable exception being the 12–19 February 2020 pair (mean = +72 kg m^{-3}).

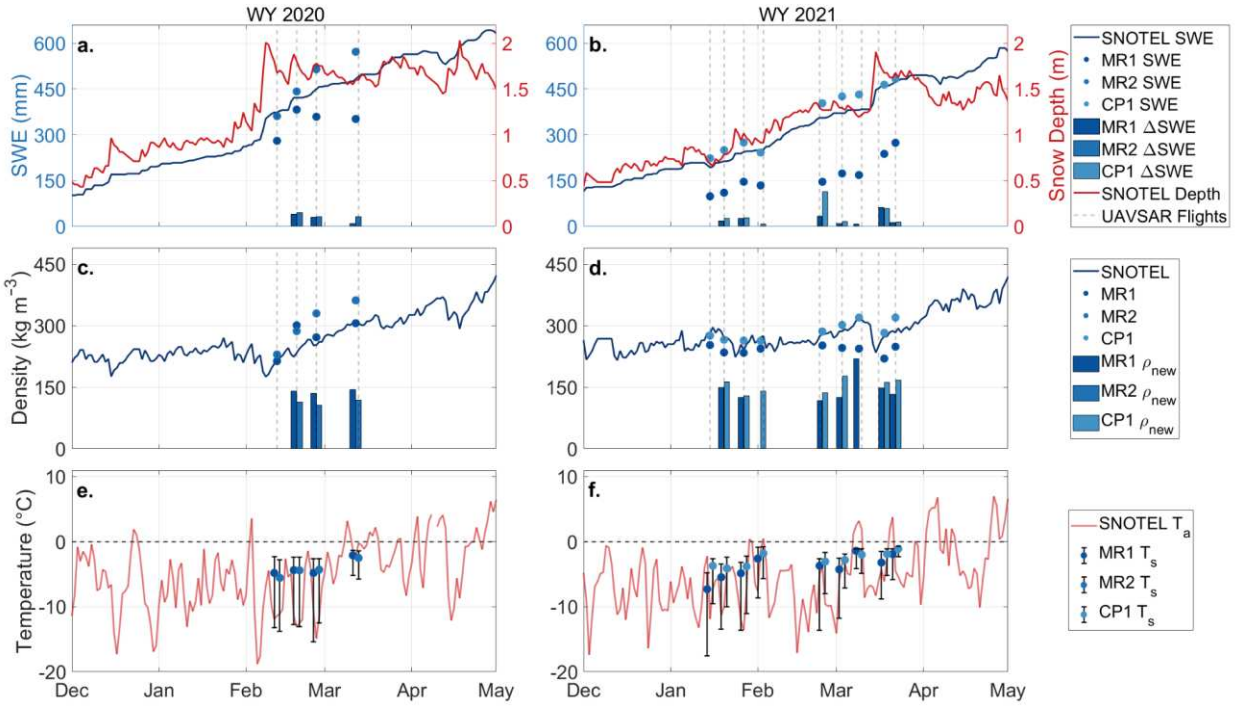

Figure 3.3: Joe Wright SNOTEL SWE and snow depth, bulk SWE and interval board SWE (ΔSWE) recorded at snow pits MR1, MR2, and CP1 for (a) water year (WY) 2020 and (b) WY 2021. SNOTEL density, bulk density and interval board density (ρ_{new}) recorded at snow pits for (c) WY 2020 and (d) WY 2021. SNOTEL air temperature (T_a) and error bar plots of snow pit temperatures for (e) WY 2020 and (f) WY 2021. UAVSAR acquisitions are represented as vertical dashed gray lines for plots (a–d). Bar graphs and error bar plots are paired and centered on the field survey date. Error bar plots show the median and the 25 and 75% quantiles.

Surface melting can lead to significant decorrelation of the radar signal and cause increased uncertainty in the ΔSWE retrievals. There were three notable warm periods during the campaigns (7–9 March 2020, 2–10 March 2021, and 21–22 March 2021), but median snow pit temperatures during our survey dates remained <–1.1°C (Figure 3.3e–f). We did observe near-surface melt-freeze crusts in the snow pits during certain surveys, but our observations suggest that liquid water content was absent or minimal during UAVSAR flight times (Table 3.1) at our study sites throughout the campaigns.

GPR SWE retrievals from the 2020 MR field site showed that median SWE increased by 127 mm between 12 February and 11 March (Figure 3.4a), with the largest median ΔSWE occurring during the 12–19 February interval (+99 mm). The 2021 MR (Figure 3.4b) and CP

(Figure 3.4c) field sites showed similar dynamic ranges, with GPR SWE retrievals increasing by 249 mm at the MR site and 233 mm at the CP site between 15 January and 22 March. For both sites, the largest median ΔSWE occurred during the 2–24 February interval (MR = +97 mm, CP = +110 mm). GPR SWE retrievals and SWE converted from depth probe measurements are highly correlated, with an overall Pearson's correlation coefficient (r) of 0.97 and an overall RMSE of 35 mm (Figure B2).

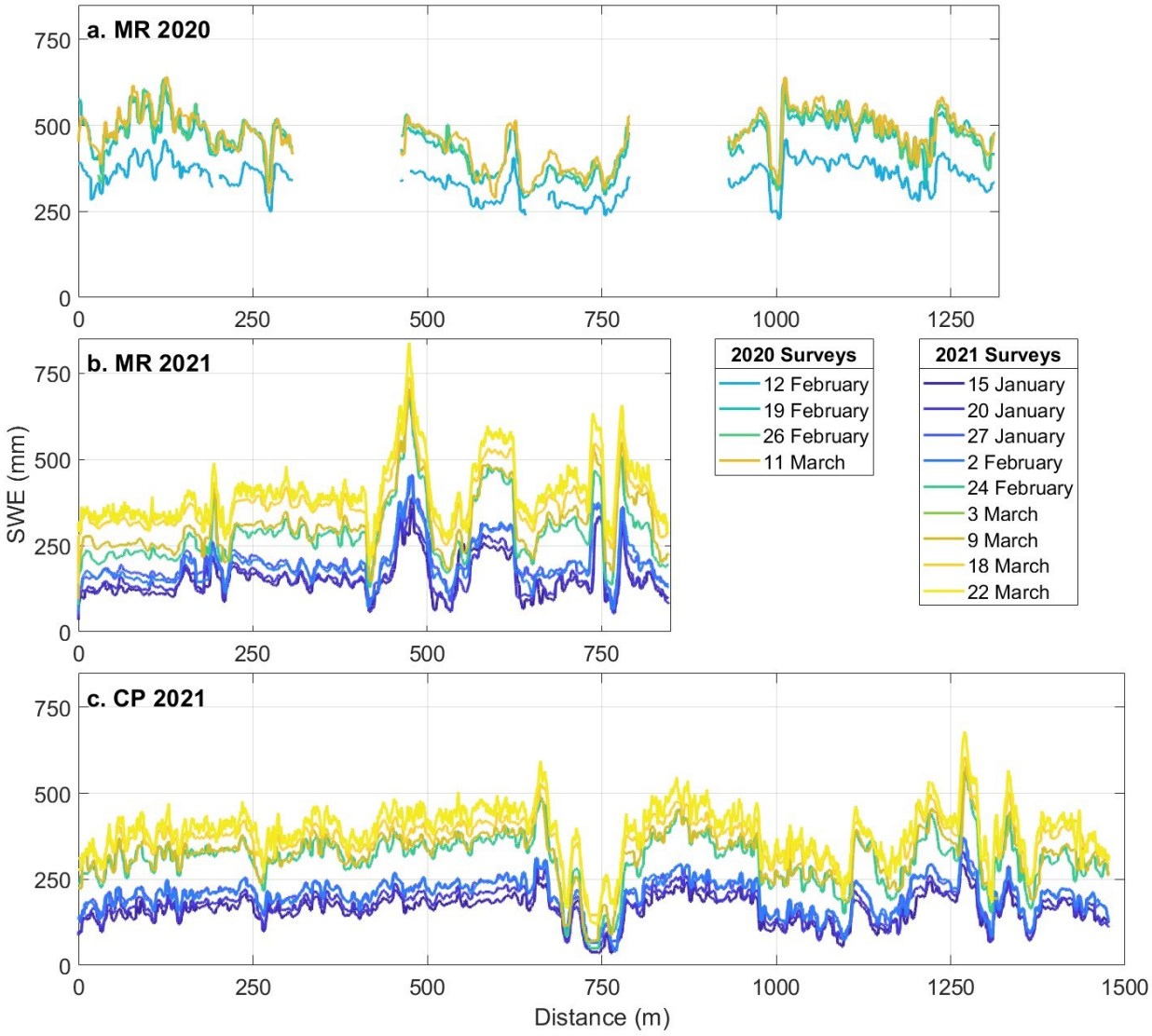

Figure 3.4: GPR SWE retrievals from the (a) 2020 and (b) 2021 MR field site, and (c) the 2021 CP field site. For (a), the transect begins at 0 m at the southern transect terminus and progresses

northward (Figure 3.1b). For (b), the transect starts at 0 m at the northeast corner and progresses clockwise (Figure 3.1b). For (c), the transect starts at 0 m at the southeast corner and progresses counter-clockwise (Figure 3.1c). GPR SWE retrievals in (a–c) have been smoothed with a 5 m moving median filter.

3.4.2 UAVSAR ΔSWE retrievals at the field sites

UAVSAR ΔSWE retrievals along the GPR transect at the 2020 MR field site saw a mean cumulative increase of 40 mm for the three intervals (Figure 3.5c–e; Table B3). The largest median ΔSWE occurred during the 12–19 February interval (median = +97 mm), with modest SWE increases observed for both the 19–26 February (median = +16 mm) and 26 February to 12 March (median = +8 mm) intervals. The largest ΔSWE retrieval range was observed for the 12–19 February interval (minimum = +60 mm, maximum = +149 mm). The expanded 2.7 km × 3.6 km region around the MR site reveals a somewhat different pattern than ΔSWE retrievals along the transect, with less accumulation for 12–19 February (+67 mm) and negligible SWE changes for 19–26 February (0 mm) and 26 February to 12 March (+1 mm; Figure 3.5c–e).

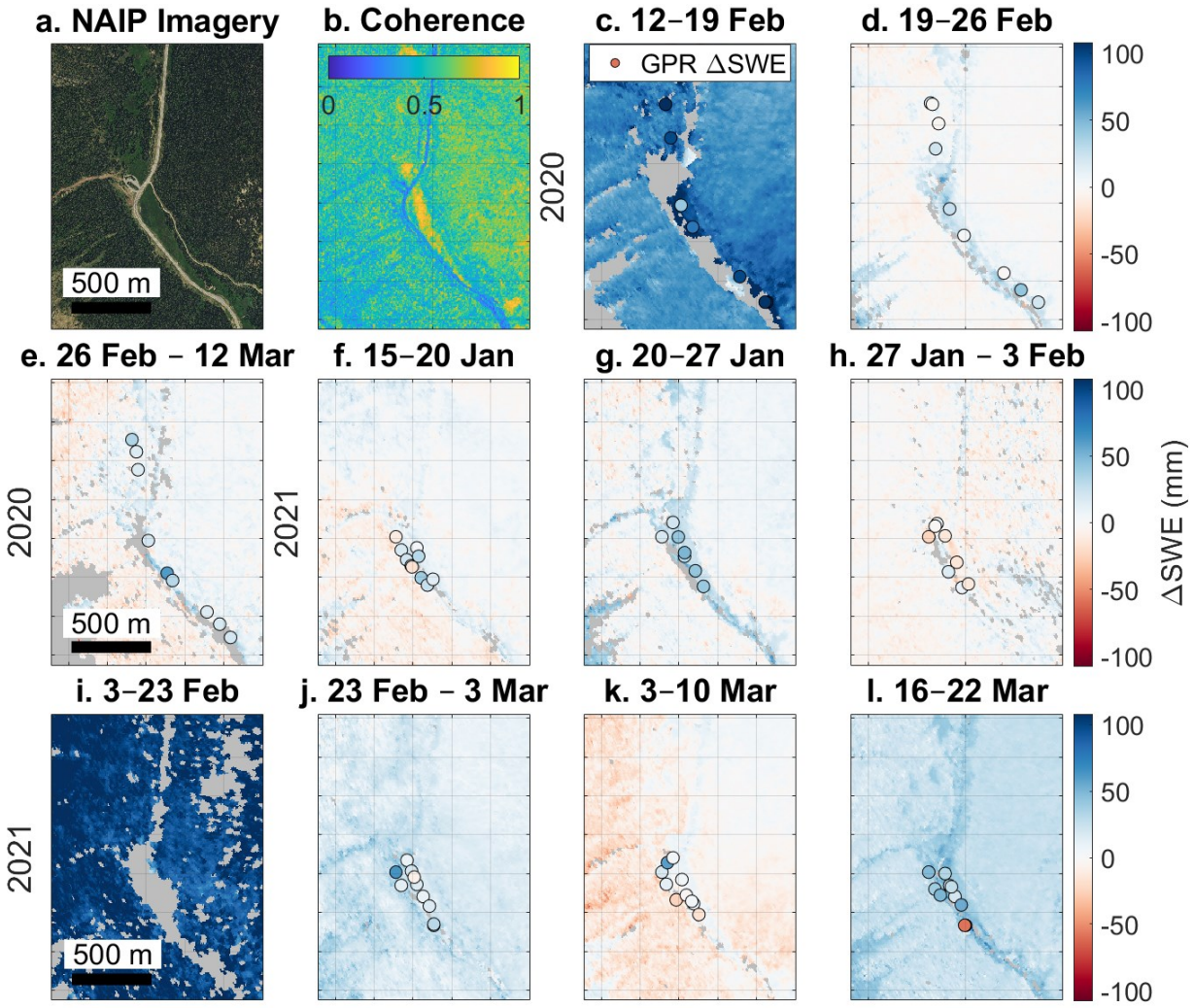

Figure 3.5: (a) National Agriculture Imagery Program (NAIP) imagery from Summer 2023. (b) Median coherence across all dates. (c–l) UAVSAR ΔSWE retrievals for each 2020 and 2021 date interval at the MR field site. GPR ΔSWE retrievals are overlain, but reduced to 5% of the total sample size for visual clarity. ΔSWE colors are minimized/maximized at approximately one phase cycle (±108 mm). All dates used the 141° flight heading and HH polarization, except for the 27 January to 3 February 2021 interval which used the 321° heading and the 3–23 February 2021 interval which used the VH polarization. No GPR points are visible for the 3–23 February 2021 interval because no coincident InSAR ΔSWE retrievals were successfully unwrapped.

UAVSAR ΔSWE retrievals along the GPR transects at the 2021 MR field site saw a median cumulative increase of 104 mm for six of the seven 2021 intervals (no data for 3–23 February 2021), whereas the median cumulative increase for the expanded 2.7 km × 3.6 km region was +143 mm (Figure 3.5f–l). At the CP site, the median cumulative SWE across the seven surveys was 203 mm along the GPR transect and 171 mm from the 2.2 km x 3 km

expanded region around the CP field site (Figure 3.6c–i). The largest median ΔSWE for the expanded regions occurred during the 3–23 February interval (MR median = +103 mm, CP median = +107 mm). Minimum UAVSAR ΔSWE retrieval medians from the expanded regions were observed on 27 January to 3 February at CP (median ΔSWE = –2 mm) and 3–10 March at MR (median ΔSWE = –6 mm).

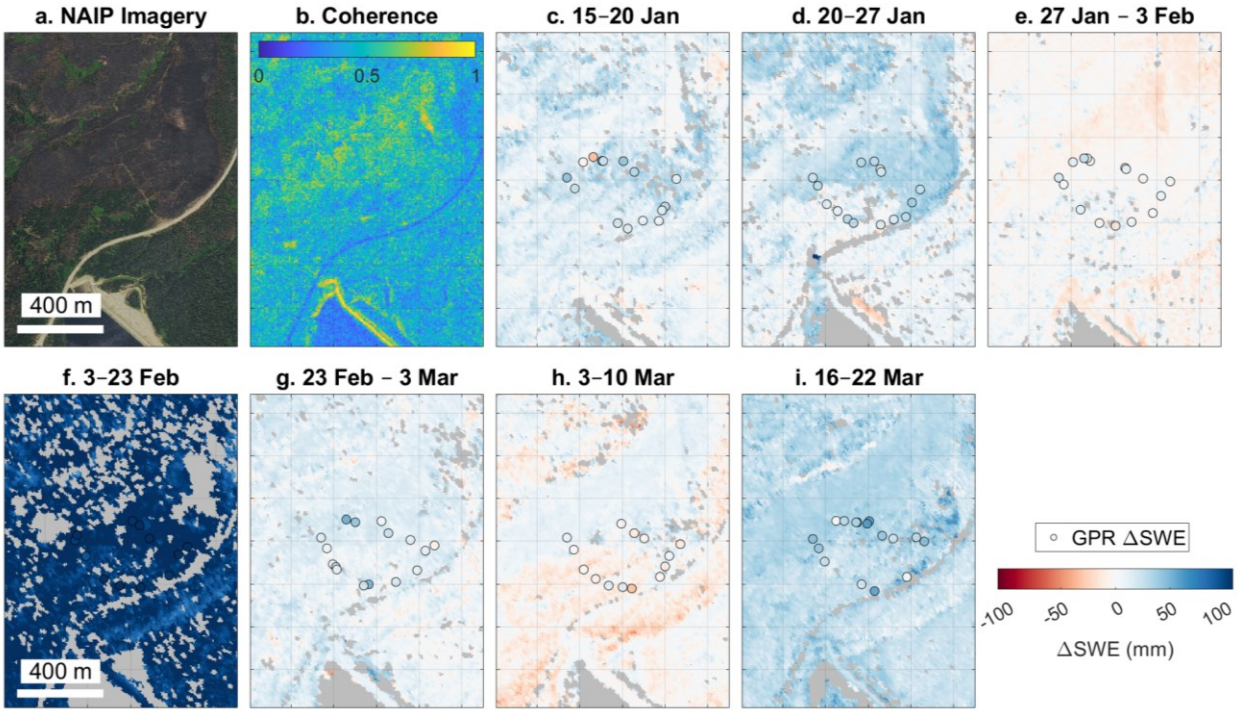

Figure 3.6: (a) Summer 2023 NAIP Imagery of the CP study site. (b) Median coherence across all dates. (c–i) UAVSAR ΔSWE retrievals for each 2021 date interval at the CP field site. GPR ΔSWE retrievals are overlain but reduced to 5% of the total sample size. ΔSWE colors are minimized/maximized at approximately one phase cycle (±108 mm). All dates used the 141° flight direction and HH polarization, except for the 27 January to 3 February interval which used the 321° direction and the 3–23 February interval which used the VH polarization.

UAVSAR ΔSWE retrievals appear to capture detailed spatial distributions of ΔSWE across all dates at each field site. In particular, larger SWE accumulation is observed in the open meadows and avalanche paths in the MR study area than the surrounding forests (mean difference = 66%, range of mean differences = –2 to +29 mm; Figure 3.5). These patterns are particularly noticeable at the MR site for the 12–19 February 2020 interval (Figure 3.5c), which

recorded a median ΔSWE increase of +98 mm in open meadows and avalanche paths, whereas ΔSWE in the surrounding forests increased by a median of +69 mm. A similar spatial pattern exists at the CP site, as the burned area consistently recorded a larger ΔSWE than adjacent unburned forests. This is best observed in the 20–27 January 2021 interval (Figure 3.6d). During this interval, we calculated an average of 31 mm ΔSWE in the burned area and 15 mm ΔSWE in the unburned forests. Median coherence across the time series is somewhat higher for unforested areas in both the MR and CP field sites (+0.05; Figures 3.5b, 3.6b). This subtle difference is further illustrated within the CP field site, where median coherence of the seven-day baseline InSAR pairs increased from 0.56 in 2020 pre-burn forests to 0.60 in 2021 post-burn areas ($p = <0.0001$).

3.4.3 Evaluating UAVSAR ΔSWE retrievals with GPR

UAVSAR ΔSWE retrievals have a relatively low pixel-wise correlation with GPR ΔSWE retrievals for any single InSAR pair ($r = –0.24$ to 0.20; Table B4). However, compiling the measurements across all surveys increases the ΔSWE dynamic range and correlation substantially ($r = 0.79$; Figure 3.7a). Here, we present a time series that includes only InSAR pairs from the HH polarization for all dates except the 3–23 February 2021 pair, which is represented by the VH polarization. For this time series, we observe RMSEs from 16–34 mm (Table B4) for single InSAR pairs, with an overall RMSE = 22 mm (Figure 3.7a). Although pixel-wise comparisons between UAVSAR and GPR ΔSWE retrievals exhibit scatter, the box plot distributions for ΔSWE at co-located GPR-UAVSAR pixels are nearly identical, yielding absolute median differences between median GPR ΔSWE and median UAVSAR ΔSWE of 0–4 mm (Figure 3.7b,c; Table B2). Although we primarily present analyses based on the HH polarization, we find that UAVSAR ΔSWE retrievals have nearly equivalent RMSE values across all four polarizations (RMSE = 19–22 mm; Table B4).

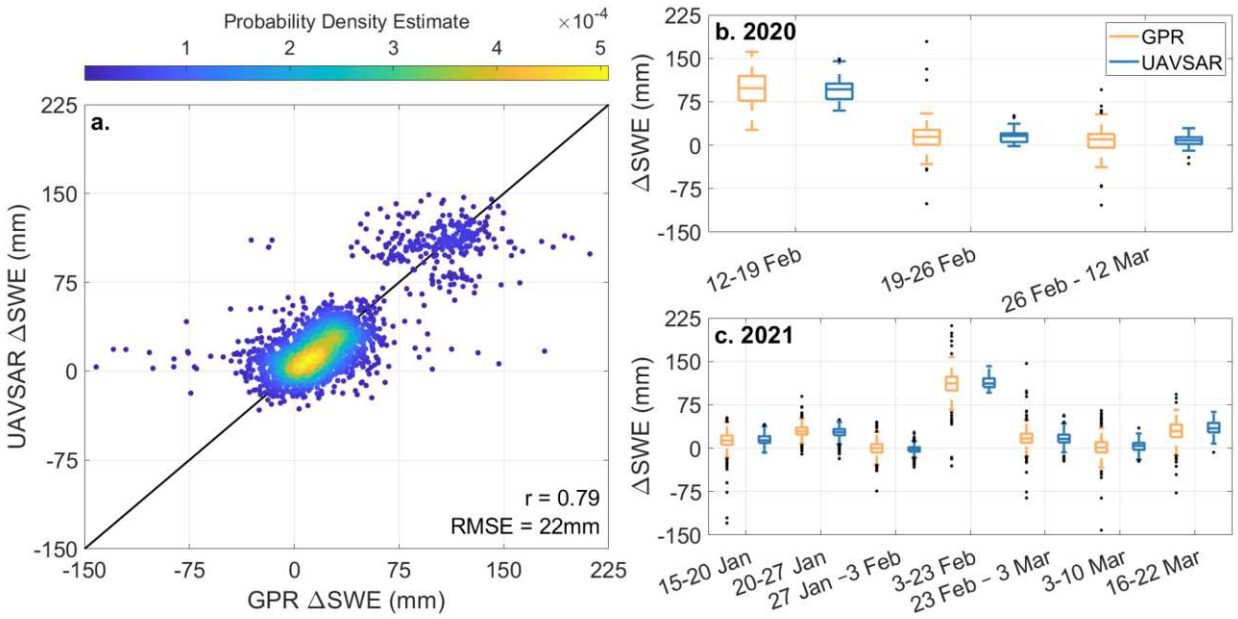

Figure 3.7: (a) UAVSAR ΔSWE retrievals compared with coincident GPR ΔSWE retrievals, with reported Pearson's correlation coefficient (r) and RMSE (n = 2833). Points in (a) are colored by point density. (b) 2020 box plot distributions of GPR and UAVSAR ΔSWE retrievals paired by date. (c) 2021 box plot distributions of GPR and UAVSAR ΔSWE retrievals paired by date. Box plots show the median, 25th and 75th quantiles, and the maximum and minimum, with outliers (>1.5 times the interquartile range) shown as points.

We explored the possibility of coherence as an error metric for UAVSAR ΔSWE retrievals and found that RMSE exhibited a narrow range (21–25 mm) for coherence bins between 0.1 and 0.7 (Figure 3.8a). However, RMSE at very low coherence (0–0.1) is double the RMSE at very high coherence (0.9–1.0). Average coherence was highest for ~weekly baselines, but average coherence for the 15-day baseline (0.51) was within the range of average coherence for the five-to-eight-day temporal baselines (Figure 3.8b). Of note, the 20-day baseline had average coherence >0.40 (Figure 3.7d) but yielded the highest RMSE (33 mm; Figure 3.8b).

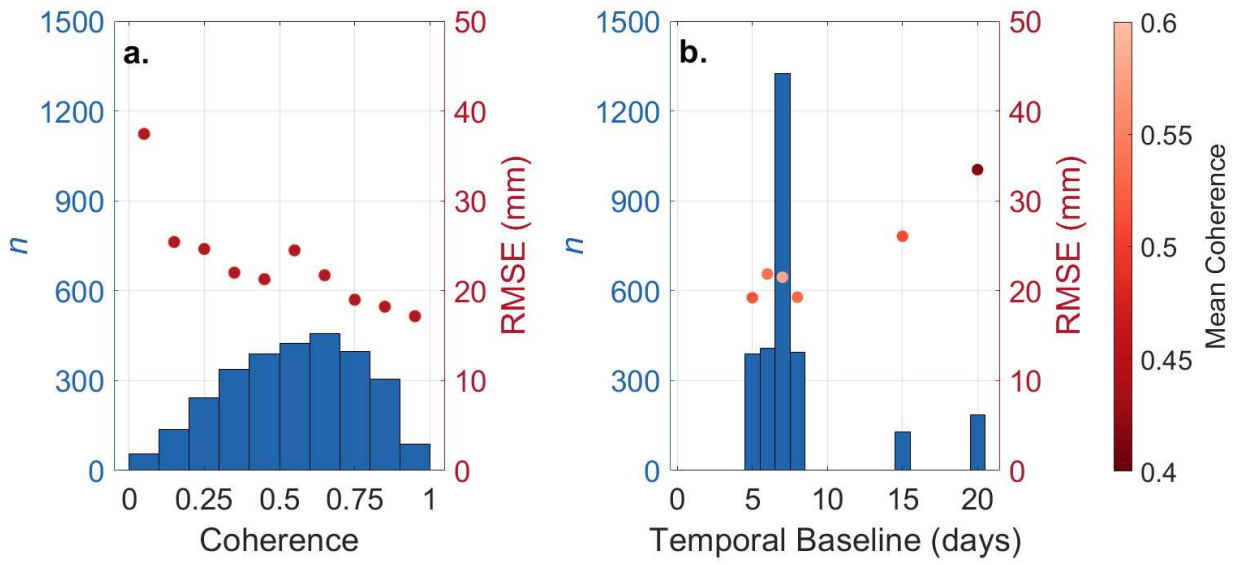

Figure 3.8: Histograms of (a) UAVSAR coherence values and (b) temporal baseline from co-located GPR and UAVSAR pixels. RMSE is shown for each bin. In (b), RMSE points are colored by mean coherence per temporal baseline bin.

3.4.4 Evaluating UAVSAR ΔSWE retrievals with TLS

TLS ΔSWE retrievals had median values of +9 mm for the MR field site during the 26 February to 12 March 2020 interval, and +55 and +39 mm at the MR and CP field sites during the 10–24 February 2021 surveys (Figure 3.9a,d,g). TLS SWE retrievals have a high correlation with SWE converted from depth probes, with a r of 0.83 and RMSE of 66 mm (n = 189; Figure B3). For each set of TLS acquisitions, UAVSAR ΔSWE retrievals had median values of +6, +60, and +45 mm, respectively (Figure 3.9b,e,h). Spatial patterns were similar between the two methods of ΔSWE retrievals. Large portions of data are missing in Figure 3.9e due to coherence-related phase unwrapping errors. RMSEs were comparable between the 2020 survey (MR = 20 mm) and the 2021 surveys (MR = 15 mm, CP = 20 mm). UAVSAR ΔSWE retrievals have an overall RMSE of 19 mm and an r of 0.72 when compared with TLS. Coherence was used to color points on the UAVSAR-TLS comparison plots (Figure 3.9c,f,i) and shows that scatter is approximately equal throughout the range of observed coherences.

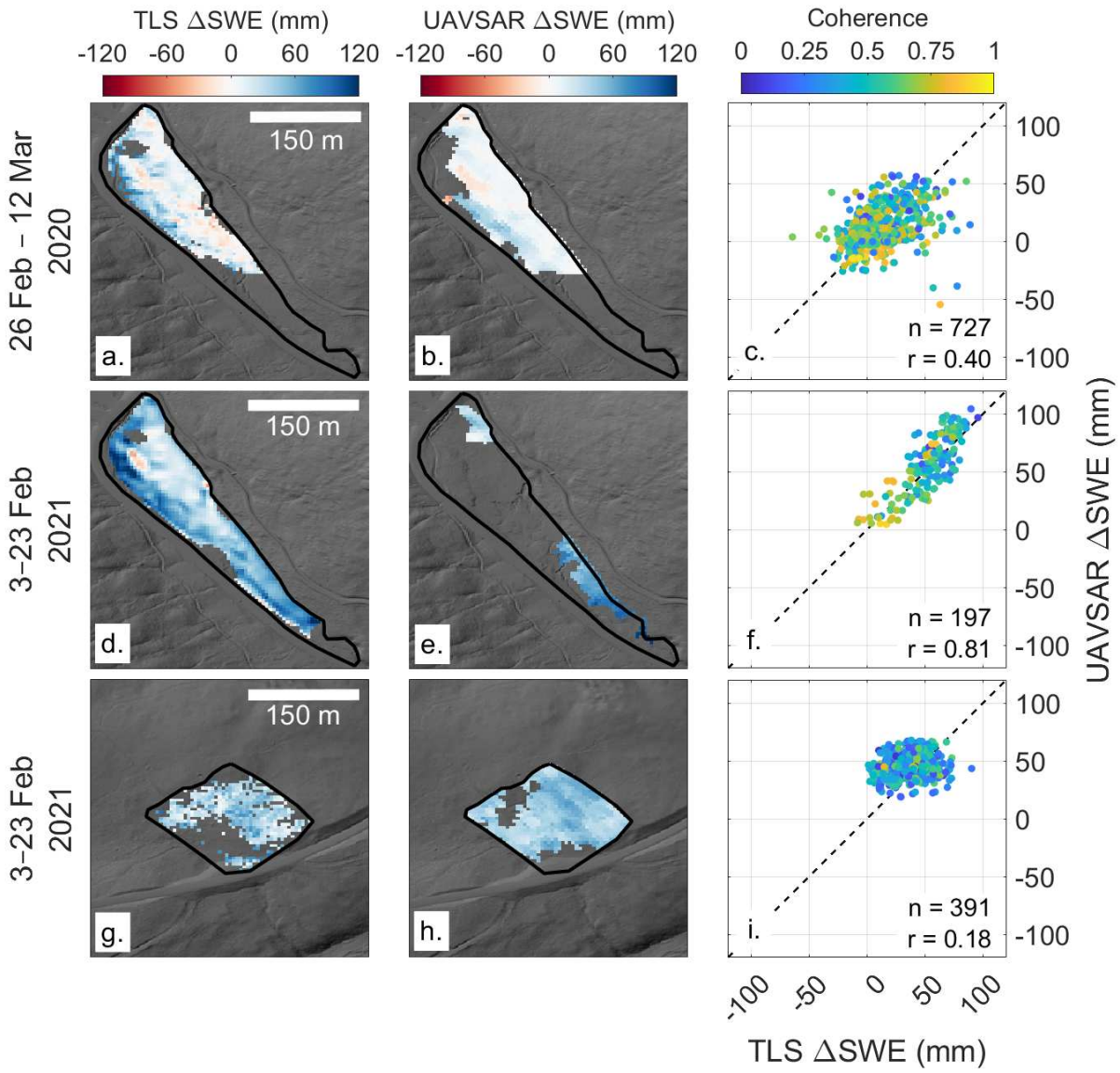

Figure 3.9: Results of the ΔSWE comparison between TLS and UAVSAR. Rows are organized by date and field site. Columns include TLS ΔSWE (left column), UAVSAR ΔSWE (middle column), and the comparison between TLS and UAVSAR (right column). SWE measured at the interval board on 10 February 2021 was subtracted from UAVSAR ΔSWE for 3–23 February 2021 to align with the TLS survey dates. Comparison plots are colored by coherence. The number of pixels (n) and Pearson's correlation coefficient (r) are reported for each comparison.

3.4.5 Evaluation of UAVSAR time series at automated stations

UAVSAR SWE retrievals overestimated SWE accumulation for the 12–19 February 2020 InSAR pair by an average of 163% at the automated stations but underestimated SWE accumulation by an average of 88% between 19 February and 12 March (Figure 3.10a–e). 2021

cumulative UAVSAR SWE retrievals record net increases at all seven sites (+109 to +219 mm), which is similar to the net increases recorded by the stations (+101 to +242 mm; Figure 3.10a–g). Median coherence for the 2020 season was lowest at the Lake Irene SNOTEL station (median coherence = 0.30) and highest at the Phantom Valley SNOTEL station (median coherence = 0.63), whereas median coherence for the 2021 season was lowest at the Montgomery Snow Stake (median coherence = 0.49) and highest at the Lake Irene SNOTEL station (median coherence = 0.60). The lowest median coherence for all sites was observed for the 26 February to 12 March 2020 interval (median coherence = 0.31), an interval that yielded negative SWE retrievals for three of the five operating stations (–17 to –3 mm). At the end of the UAVSAR campaigns, cumulative UAVSAR SWE retrievals from the seven stations (n = 12) yielded an RMSE = 42 mm and an r = 0.92 (Figure 3.10h).

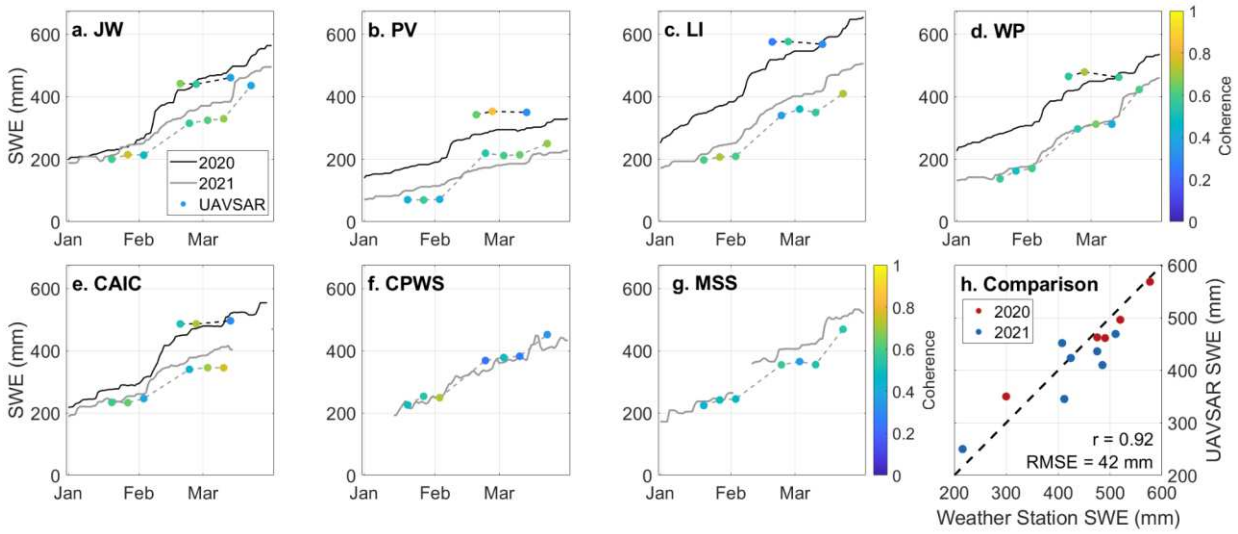

Figure 3.10: Time series of 2020 and 2021 UAVSAR ΔSWE retrievals compared with SWE from (a) the Joe Wright SNOTEL station (JW), (b) the Phantom Valley SNOTEL station (PV), (c) the Lake Irene SNOTEL station (LI), (d) the Willow Park SNOTEL station (WP), (e) the Colorado Avalanche Information Center weather station (CAIC), (f) the Cameron Peak field site weather station (CPWS), and (g) the Montgomery Snow Stake site (MSS). Mean 9-pixel coherence is shown for each UAVSAR point. (h) Comparison between SNOTEL SWE and cumulative UAVSAR SWE for the last UAVSAR flight for each year. For sites (e–g), only snow depth was observed and SWE was estimated using density recorded at the closest SNOTEL

station (Joe Wright SNOTEL). Methods describing the alignment of the UAVSAR time series to the automated stations are described in Section 3.3.3.

3.5 DISCUSSION

3.5.1 Accuracy of L-band InSAR ΔSWE retrievals

From our evaluation with GPR and TLS, we established an RMSE for L-band InSAR ΔSWE retrievals as 19–22 mm for single InSAR pairs (Figures 3.7, 3.9). For cumulative InSAR SWE, we estimated a RMSE of 42 mm at seven automated stations (Figure 3.10). Previous studies have established that UAVSAR ΔSWE retrievals resemble the spatial patterns of lidar-derived ΔSWE retrievals, but differences between the two datasets were not systematic (Marshall et al., 2021; Palomaki & Sproles, 2023). Marshall et al. (2021) evaluated UAVSAR ΔSWE retrievals over a 4 km^2 relatively flat and non-forested region of Grand Mesa, Colorado using airborne lidar and found very low error for the technique (RMSE = 9 mm). UAVSAR ΔSWE retrievals have been evaluated using GPR and automated station measurements in Valles Caldera, New Mexico (Tarricone et al., 2023) and from in situ and SNOTEL measurements of ΔSWE in the mountains of Idaho (Hoppinen et al., 2023). Both studies identified and corrected significant atmospheric artifacts and contained at least one InSAR pair that was collected when liquid water content was present in the snowpack, but estimated study-wide errors of similar magnitude found by our study (RMSE = 15–40 mm; Table B4).

UAVSAR ΔSWE retrievals had higher RMSE in 2020 than in 2021 (Table B4), and the agreement between the InSAR time series and the automated stations was poorer in 2020 than in 2021 (Figure 3.10). One potential explanation for the lower agreement in 2020 was the significant deviation (>10 m) from the cross track and vertical baselines of the aircraft during the 2020 flights (Jones et al., 2016; NASA UAVSAR, 2023). UAVSAR ΔSWE spatial patterns are similar to those of TLS ΔSWE (Figure 3.9) and the comparison of UAVSAR and GPR ΔSWE

site-wide distributions reveal nearly identical medians (absolute median difference = 2 mm; Figure 3.7b–c). We found that low coherence did not substantially increase the RMSE of UAVSAR ΔSWE retrievals as the RMSE was less than 35 mm for >10-day temporal baselines (Figure 3.8). However, lower coherence for InSAR pairs with >10-day temporal baselines exhibited issues with phase unwrapping. Collectively, these findings suggest a high degree of accuracy and reliability for InSAR ΔSWE retrievals, particularly in relatively simpler environments (i.e., dry snow conditions, non-forested areas, slopes <20°) and when atmospheric delays are limited.

3.5.2 Considerations for future evaluations of InSAR ΔSWE retrievals

The NISAR satellite mission holds promise for global repeat 12-day ΔSWE retrievals, providing the opportunity to evaluate the L-band InSAR technique in a range of environments and to better assess its uncertainties. In our evaluation, we used two ground-based methods that many snow community researchers have access to and showed that both methods are capable of assessing InSAR ΔSWE retrieval accuracy. Both methods can be used to derive spatially continuous SWE measurements over large areas and are therefore advantageous over standard in situ SWE measurement methods (Holbrook et al., 2016; McGrath et al., 2019). Below we outline advantages, considerations, and challenges of GPR and TLS for InSAR evaluation.

Few methods match the sophistication of InSAR for change detection. Of the two techniques we employed in our evaluation, lidar is the most applicable for change detection (Deems et al., 2013), but its methodology for ΔSWE retrievals is not straightforward. There are two conceptual paths for ΔSWE retrievals from lidar: (1) subtraction of two repeat snow-on lidar elevation surveys or (2) subtraction of two bulk SWE datasets derived from lidar. The first option is complicated by snow compaction, while the second option requires accurate bulk snow densities and a snow-off bare-earth digital terrain model, which may be difficult to acquire in

densely vegetated areas. We chose the second option because bulk density variability is less of a concern for the relatively small areas surveyed by the TLS (Bonnell et al., 2023). We found the best agreement between UAVSAR and TLS ΔSWE retrievals for surveys that were aligned on the same date, as differential SWE accumulation/redistribution increased uncertainty (Figure 3.9). Note that if the TLS platform is set up on top of the snowpack, accurate TLS ΔSWE retrievals may be hindered by small shifts in the TLS platform as it settles in the snow (Currier et al., 2019).

Repeat GPR transects also have several challenges. Our survey methodology involved marking our transects and post-processing the onboard GPS sensor (±0.25 m accuracy), but it is likely that our tracks were offset by ±1–2 m from the transect for some surveys. Further, as SWE increases throughout a season, the *twt* to the ground reflector increases, effectively increasing both the GPR horizontal footprint and the potential for clutter in the radargram (Daniels, 2004). Surface-coupled GPR has the potential to both compact the snow below the sled and remove snow from the surface (e.g., McGrath et al., 2019), which may further increase the uncertainty of GPR ΔSWE retrievals, particularly in low density snow on the surface of the snowpack. These complications may explain the low Pearson's correlation coefficients observed between UAVSAR and GPR ΔSWE retrievals for single InSAR pairs ($r = –0.24$ to $+0.2$; Table B4), as well as the low GPR-UAVSAR ΔSWE retrieval relation ($r^2 < 0.1$) described by Tarricone et al. (2023). However, as our analysis shows, repeat GPR transects are effective at evaluating the InSAR technique if there is enough data collected across a range of SWE accumulation magnitudes (Figure 3.7).

A major difference between UAVSAR and planned NISAR interferograms is the spatial resolution (~5 m vs. 80 m), which may complicate future NISAR ΔSWE retrieval ground-based

evaluations. GPR surveyed along transects scaled well to the resolution of UAVSAR, but a different survey design (i.e., spiral or grid) may be required to provide sufficient coverage of the NISAR pixels. Thus, GPR may have increased uncertainty in its scalability due to a difficulty of repeating complicated survey designs. Lidar is scalable to coarser resolutions (e.g., 50 m; Painter et al., 2016) and TLS and drone-mounted lidar (e.g., Feng et al., 2023) may be valuable tools for evaluating InSAR ΔSWE retrievals at small field sites. However, at larger scales, comprehensive airborne lidar surveys will be required to fully evaluate NISAR ΔSWE retrievals.

3.5.3 Remaining questions for the L-band InSAR ΔSWE retrieval technique

L-band InSAR has been seen as a promising technique for high resolution snow monitoring for over a decade (Deeb et al., 2011), yet insufficient opportunities existed for robust evaluations. In the last few years, airborne InSAR campaigns over seasonal snowpacks have created opportunities for a more thorough evaluation of this technique. Our study, and others, show that this technique can have high accuracy, but there are several areas of uncertainty that need to be considered, including forested environments, wet snowpacks, complex topography that results in steep incidence angles, spatially varying atmospheric delays, and the integration of InSAR ΔSWE retrievals with other remote sensing methods and models.

Recent UAVSAR studies (Hoppinen et al., 2024; Marshall et al., 2021; Palomaki and Sproles, 2023; Tarricone et al., 2023), including this study, have largely focused on ΔSWE retrievals in open environments. We found that ΔSWE retrievals were 66% higher on average in the open areas around the MR field site than below forest cover. Forest canopy interception and sublimation may play a role in this signal, because this process is known to drive a 20–30% reduction of total snowfall at the nearby Fraser Experimental Forest (Montessi et al., 2004). On the other hand, a contrast between lower snow surface densities in the forest compared with the potentially higher densities we measured in the open could explain a similar magnitude of the

signal. Unfortunately, we are unable to evaluate the forest ΔSWE retrievals as only 20% of GPR observations in 2020 and 10% of GPR observations in 2021 were collected below spruce/fir canopy (15–70% canopy cover). Forests interfere with the radar signal, reducing coherence and potentially biasing retrievals, particularly for longer temporal baselines (Li et al., 2022; Ruiz et al., 2022). However, coherence only improved by +0.05 from forests to open areas at our field sites and even the removal of canopy due to the Cameron Peak wildfire only increased coherence by +0.04. Thus, because of its canopy penetrative capabilities, the L-band InSAR ΔSWE retrieval technique may be the first satellite-based technique viable for SWE monitoring in forests.

At our site, UAVSAR flights occurred during the accumulation season when the snowpack was likely dry (Figure 3.3e–f). However, SWE monitoring is needed for snowpacks that accumulate at or near 0°C and for the melt season, making ΔSWE retrieval evaluation prioritized in wet snowpacks. Liquid water in the snowpack raises both the real and imaginary components of relative permittivity, which decreases the snowpack radar velocity and increases absorption of the radar signal, causing decreased signal penetration (Tsai et al., 2019). Even in the backscattering interface is unchanged, reduced radar velocity causes ΔSWE retrieval overestimation if the liquid water content is not considered (Bonnell et al., 2021; Tarricone et al., 2023). Tarricone et al. (2023) evaluated ΔSWE retrievals with the Landsat fractional snow-covered area product and found reasonable snowpack ablation over a 14-day period in Valles Caldera, New Mexico, but Hoppinen et al. (2024) found reduced ΔSWE retrieval accuracy in wet snowpacks. Wet snow detection techniques have been developed and implemented at C-band (e.g., Gagliano et al., 2023; Nagler and Rott, 2000; Nagler et al., 2016) and similar techniques should be evaluated at L-band frequencies (e.g., Park et al., 2014).

3.6 CONCLUSION

During the winters of 2020 and 2021, UAVSAR collected L-band InSAR datasets over 12 mountainous regions of the western United States, including continental snowpacks of Colorado, intermountain snowpacks of Idaho and Montana, maritime snowpacks of California, and shallow mountain snowpacks in New Mexico. At the Cameron Pass field site, we used extensive GPR and TLS to evaluate UAVSAR ΔSWE retrievals over a three-pair time series (4 weeks) that saw 121 mm SWE accumulation in 2020 and a seven-pair time series (9 weeks) that saw 206 mm SWE accumulation in 2021. Our analysis was not complicated by the presence of liquid water within the snowpack and we emphasized GPR and TLS collection in open areas at our field sites. Our results indicate accurate statistical distributions for the L-band InSAR method for areas without forest cover (absolute median difference = 2 mm compared to GPR), but low correlation coefficients ($r = -0.24$ to $+0.20$) for individual InSAR pairs warrants caution for ΔSWE interpretation at the single pixel scale. UAVSAR ΔSWE retrievals exhibited distinct and repeated spatial patterns relating to the land cover, as forests averaged 66% less ΔSWE per InSAR pair than open meadows, burned forests, and avalanche alleyways in forests. We expanded our in situ SWE observations to include seven automated weather stations, distributed throughout the swath and highlighted the utility of the InSAR method for measuring cumulative SWE (RMSE = 42 mm), a requirement for any SWE remote sensing method. We found that the range in RMSE from coherences of 0.10–0.90 was <10 mm, indicating that low coherence does not necessarily inhibit the accurate retrieval of ΔSWE. Although our ground observations did not target forested areas, we found the median coherence in the forests averaged 0.05 less than in the open, suggesting ΔSWE retrievals may be viable in these environments, but the location of the amplitude-center as forest cover increases remains an active question. Collectively, our study

supports the use of L-band InSAR for measuring SWE in mountain snowpacks, further highlighting the potential for NISAR and other upcoming L-band SAR satellites to contribute substantially to global SWE monitoring.

4. L-BAND INSAR SNOW WATER EQUIVALENT RETRIEVAL UNCERTAINTY INCREASES WITH FOREST COVER FRACTION[3]

4.1 INTRODUCTION

The monitoring of seasonal snowpacks is critical for understanding ecosystems (Gleason et al., 2021; Pedersen et al., 2021), drought forecasting (Livneh & Badger, 2020), and for managing snowmelt runoff, an important resource for billions of people (Barnett et al., 2005). However, current monitoring is insufficient, particularly within mountains, where complex topography, montane forests, and highly variable snowpack distributions present significant challenges to remote sensing methods (Dozier et al., 2016; Sturm et al., 2017). The remote sensing of snow water equivalent (SWE), the defining snow hydrologic variable, is highly prioritized (e.g., National Academies of Science, Engineering, & Medicine, 2018) and methods for snow depth/SWE retrievals are in development, but forests remain a significant challenge (e.g., Hu et al., 2023; Lievens et al., 2019; Oveisgharan et al., 2024).

The retrieval of SWE below forest canopy is critical because forests comprise an estimated 15 million km^2 of the Earth's seasonal snow cover (NASA SnowEx, 2024). In the western contiguous US, an estimated 67% of the seasonal snow covered area is forested and almost entirely contained within mountain environments (Moore et al., 2012; Bourgoin et al., 2023) where 70% of region-wide runoff is generated (Li et al., 2017). In these complex environments, airborne lidar is the most accurate SWE retrieval technique with high spatial resolution (<100 m; Painter et al., 2016), but airborne lidar is cost-prohibitive at global scales, relies on modeled snow density to calculate SWE, and fails to satisfy the <weekly temporal

[3] Chapter in preparation as Bonnell, R., McGrath, D. Elder, K., Marshall, H. P., Starr, B., Adebisi, N., Palomaki, R., & Hoppinen, Z. L-band InSAR Snow Water Equivalent Retrieval Uncertainty Increases with Forest Cover Fraction.

requirements set by the Decadal Survey (National Academies of Science, Engineering, & Medicine, 2018). Considering the required spatial and temporal resolutions for SWE retrievals, photogrammetry from stereo/tri-stereo satellite imagery (e.g., Hu et al., 2023) and methods using synthetic aperture radar (SAR) are the front-runners for measuring SWE in mountain environments. Below, we discuss SAR methods, which includes the SAR interferometry (InSAR) approach implemented in this study.

SARs are side-looking radars that transmit a signal and record the amplitude and phase of the backscattered return. SAR methods have high spatial resolution, but most platforms have >weekly revisit periods. Radar is transmissible through snow at lower frequencies (e.g., <18GHz), and will reflect at boundaries with contrasting dielectric permittivities (e.g., the snow-ground interface; Deeb et al., 2011). Although the radar signal interacts with the forest canopy, SAR may be capable of sub-canopy SWE retrievals because the radar wave can penetrate the canopy, particularly at lower frequencies (e.g., L-band, 1–2 GHz, ~25 cm wavelength). SAR backscatter approaches at high frequency (X-, Ku-band; 8–12 GHz, 2.5–3.75 cm wavelength) are applicable in both shallow and deep snowpacks (e.g., Borah et al., 2023), but accurate modeling of tree microwave emission, absorption, and the tree scattering properties is required for SWE retrievals below forest cover (Tsang et al., 2022). SAR interferometry (InSAR) approaches measure a change in SWE (ΔSWE) from the phase-change between SAR acquisitions (Guneriussen et al., 2001). This approach for SWE retrievals has been implemented using tower-based radars, for satellites operating at C- (4–8 GHz, ~5 cm wavelength) or L-bands, and for airborne SARs operating at L-band (e.g., NASA Uninhabited Aerial Vehicle SAR or UAVSAR). A list of relevant InSAR SWE retrieval studies is provided in Table C1. This technique is particularly advantageous because it requires no a priori snowpack information for dry snow

conditions (Leinss et al., 2015) and coherence, a measure of similarity between two signals, can be maintained for longer temporal baselines (e.g., 12-day; Ruiz et al., 2022). Several uncertainties remain for the technique, particularly below forest cover (e.g., Ruiz et al., 2022).

Here, we evaluate eight L-band InSAR pairs collected from the UAVSAR platform as part of the SnowEx 2021 Time Series Campaign at the Fraser Experimental Forest (FEF), Colorado, USA. In situ measurements were collected across a range of elevations and forest covers, and snow-on/off airborne lidar scans were collected to measure spatially distributed snow depths near the end of the UAVSAR campaign and vegetation heights. Our study examines the applicability and limitations of this method in montane forests by addressing two key questions:

1. What is the accuracy of L-band InSAR ΔSWE retrievals from single interferometric pairs in both forested and open environments based on ground measurements?
2. Can a time series of InSAR SWE capture the observed elevation and forest cover snow distributions documented by lidar snow depths?

Our work informs on the potential applications and limitations of the technique in forests for the upcoming L-band NISAR satellite mission (planned 2024 launch). Because datasets collected by NISAR will be publicly available at high spatiotemporal resolution (80 m, 12-day revisit), this technique may offer the first path towards open-access SWE retrievals in the world's water towers (Immerzeel et al., 2020).

4.2 NASA SNOWEX AT FRASER EXPERIMENTAL FOREST

The NASA SnowEx 2021 Time Series campaign was implemented at seven field sites across the western USA (Marshall et al., 2020). The campaign emphasized acquisitions from UAVSAR, a quad-polarized L-band (1.26 GHz center frequency, 0.24 m wavelength, 80 MHz bandwidth) left-looking SAR. Eight InSAR pairs with a northwest heading (052°) and four pairs

from the reverse heading (233°) were collected over FEF in Colorado (Figure 4.1a). UAVSAR flew at an altitude of ~12.5 km ~weekly from 15 January to 22 March, with a 20-day temporal baseline separating the 3 and 23 February acquisitions.

FEF has a dry continental snow climate with a median peak SWE of 569 mm recorded by the Fool Creek SNOTEL station (3400 m elevation). During UAVSAR flights (±1 day), probed snow depths and snow pit measurements of depth, density, temperature, relative permittivity, and stratigraphy were collected at three field sites: Headquarters (HQ; 0.3 km^2), St. Louis Creek (StL; 1.4 km^2), and Fool Creek (FC; 1.4 km^2; Figure 4.1d–f). The Fool Creek SNOTEL station is near the FC site and records snow depth, density, and air temperature at hourly intervals. FEF has a large elevation range (~1000 m) with communities of lodgepole pine (*Pinus contorta*) and aspen (*Populus tremuloides*) at lower elevations and Engelmann spruce (*Picea engelmannii*) and subalpine fir (*Abies lasiocarpa*) at higher elevations (Huckaby & Moir, 1998). Of the three sites, FC is located at the highest elevation and has the highest average forest cover fraction (~3200 m; 0.62 FCF), whereas both HQ and StL are located at relatively lower elevations and have lower FCF (~2700 m; 0.20 FCF). Snow-on (19 March 2021; ~78% of peak SWE at SNOTEL) and snow-free (18 September 2021) lidar scans were collected to measure spatially distributed snow depths and vegetation heights (Adebisi et al., 2022). In situ sampling strategies are described in Text C1 and UAVSAR flight dates and field survey dates/observations are available in Table C1.

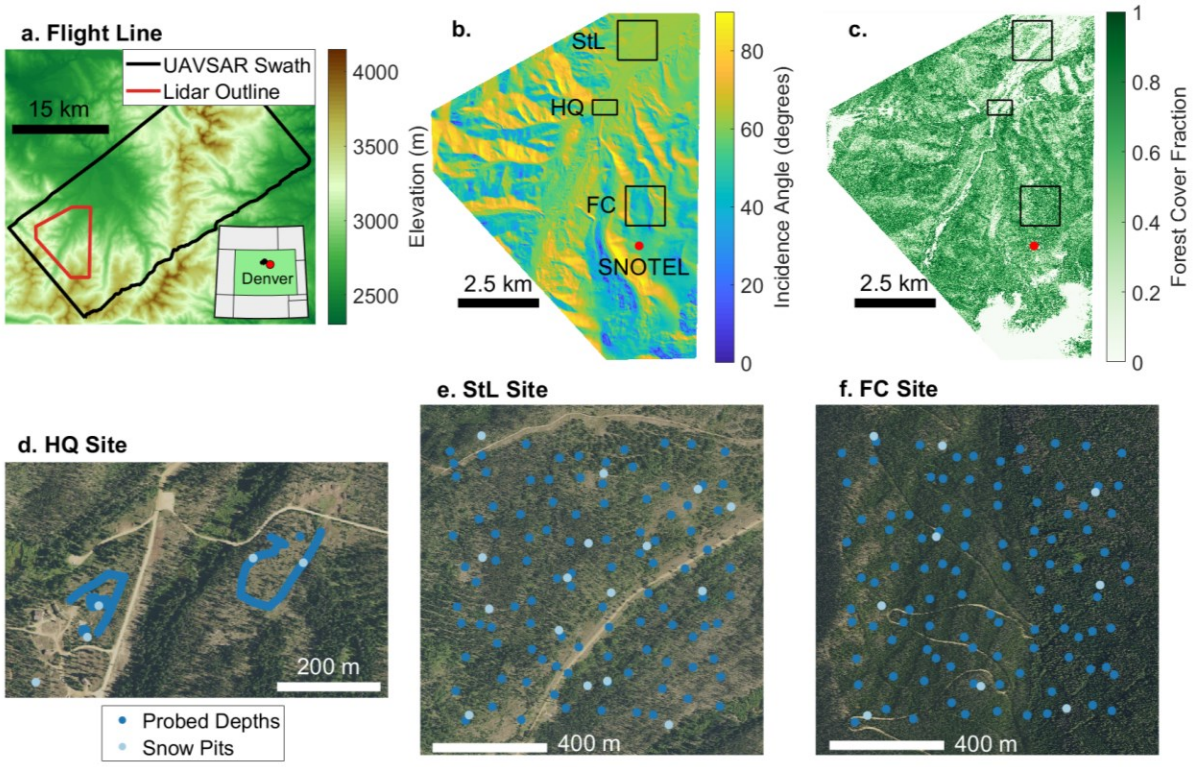

Figure 4.1: Copernicus 30 m DEM with Fraser, CO UAVSAR swath and inset map of Colorado. Study area showing (b) UAVSAR local incidence angles derived from the lidar DEM and (c) FCF derived from lidar vegetation heights. NAIP imagery with locations of depth probe and snow pit measurements at the (d) HQ, (e) StL, and (f) FC field sites.

4.3 METHODS

4.3.1 Processing UAVSAR datasets

We present detailed methods for the ΔSWE calculation from UAVSAR datasets and the polarimetric decomposition in Text C2. Here, we provide a summary of the datasets and processing flow. UAVSAR datasets were collected and processed to ~5 m resolution by the UAVSAR team. We accessed InSAR datasets (i.e., ground projected unwrapped interferograms and coherence products) and the POLSAR datasets (ground projected σ^0 products) via the Alaska Satellite Facility (ASF; NASA UAVSAR, 2021) through uavsar_pytools (Hoppinen & Tarricone, 2022). We performed a polarimetric decomposition to better understand how the scattering characteristics vary by forest cover (Text C2.4). We removed an atmospheric phase ramp from both headings of the 3–10 March InSAR pairs (Text C2.2). We determined that liquid water

content was either absent or <1 vol. % during UAVSAR flights based on snow pit measurements (Figure C3; Text C2.3). However, melt dynamics differ in canopy-intercepted snow (Bonner et al., 2021), which was present during March surveys (Figure C4). Phase calibration for the unwrapped interferograms was calculated as the difference between phase-change estimated from ΔSWE at an HQ snow pit with high coherence (>0.6) and the median phase-change from the 3x3 pixel grid around the snow pit. Finally, ΔSWE retrievals were calculated following Text S2.1 from the unwrapped interferograms, relative permittivity estimated from the upper 10 cm of snow pit-measured densities, and the local incidence angle calculated from the lidar DEM (Adebisi et al., 2022a). ΔSWE was calculated for all four polarizations, but we present only the VV polarization, except 3–23 February, which used the VH polarization due to phase unwrapping errors, in the main text.

4.3.2 Evaluating UAVSAR with in situ measurements

We grouped our in situ measurements into two categories: SWE measured from snow pits, the SNOTEL station, or the HQ interval board as SWE_{sp} and SWE converted from probed snow depths as SWE_{ds} (Text C1.3). UAVSAR ΔSWE was calculated over a 3x3 pixel grid surrounding each SWE_{sp} measurement to reduce uncertainty imposed by the snow pit disturbance. UAVSAR and ΔSWE_{sp} were summed with each sequential UAVSAR acquisition to better understand the UAVSAR accuracy across the nine week period. For SWE_{ds}, only one coincident UAVSAR ΔSWE pixel was compared with the ΔSWE_{ds} measurement. Pearson's Correlation Coefficient (r) and the root mean squared error (RMSE) were calculated for ΔSWE_{sp} and ΔSWE_{ds}. Comparisons were then binned by FCF, coherence, and temporal baseline to better understand the influence of these parameters upon UAVSAR ΔSWE retrieval accuracy (see Text C3 for FCF calculations). Finally, median ΔSWE_{sp} and ΔSWE_{ds} and median UAVSAR ΔSWE

measurements were summed for each interval at each field site and compared. The starting SWE value for each field site was the median in situ SWE for the site on the first date of field observations. The time series at FC was primarily calculated from the SNOTEL station, because only two surveys were performed at this site (Table C2).

4.3.3 Evaluating UAVSAR with lidar snow depths

We resampled the 19 March lidar snow depth dataset (Adebisi et al., 2022b) to the UAVSAR grid and integrated UAVSAR SWE by summing the 052° heading ΔSWE products from 15 January to 22 March. The lidar snow depths represent absolute snow depths at the end of the UAVSAR campaign and are, therefore, not directly comparable to the integrated UAVSAR SWE, which represents the accumulated snow mass during the nine week campaign. However, because snow depth exerts a primary control on SWE (Jonas et al., 2009), we normalized the lidar snow depths and cumulative UAVSAR SWE using the z-score method to compare the spatial distributions. Normalized lidar snow depths and normalized integrated UAVSAR SWE were binned by FCF, elevation, and UAVSAR incidence angle to better understand the limitations of the L-band InSAR technique.

4.4 RESULTS

4.4.1 UAVSAR ΔSWE retrievals

UAVSAR recorded both SWE loss and SWE gain throughout the time series (Figures 4.2, C5). The largest SWE accumulation occurred for the 3–23 February (46 ±17 mm) interval, whereas the 3–10 March (0 ±10 mm) observed negligible gains/losses in SWE. ΔSWE retrieval means and standard deviations were identical between the 052° and 233° headings and across all polarizations (Figures 4.2, C5; Table C3).

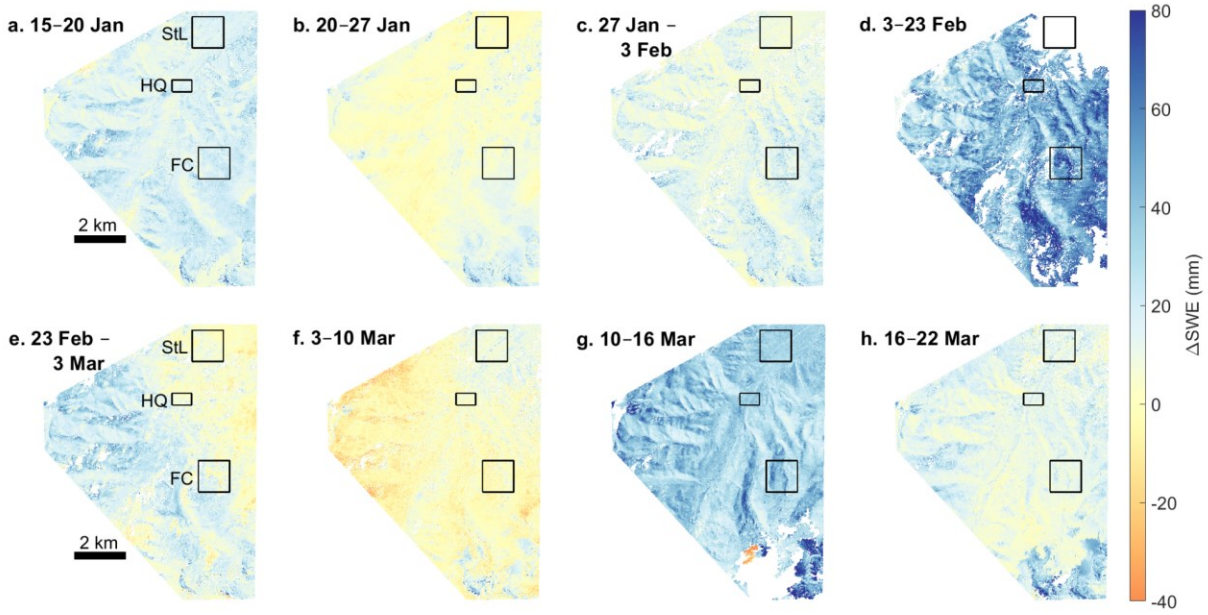

Figure 4.2: UAVSAR ΔSWE retrievals at the study site for each 052° InSAR pair. Field sites are outlined in black. White denotes missing data due to phase unwrapping issues.

The polarimetric decomposition resulted in four scattering categories for FEF (Figure C7). Smooth surface scatter is exclusively observed above treeline, whereas canopy scattering and volume scattering are observed in the remainder of the scene. 95% of the study site is classified as medium entropy, a metric of signal depolarization, and 5% is classified as low entropy, indicating that depolarization occurs even for unforested areas. The overall mean anisotropy, used to describe the number of backscattering interfaces, is 0.35 with <1% of values >0.5, indicating a low likelihood of more than one dominant backscattering interface in the forests.

4.4.2 UAVSAR vs. in situ observations

For the 052° heading, cumulative average UAVSAR SWE was within ±12% of the average in situ SWE at StL and at FC for all InSAR intervals, whereas UAVSAR at HQ overestimated SWE by up to 22% by the end of the campaign (Figure 4.3a). The largest divergence between UAVSAR and in situ measurements occurred during the 10–16 and 16–22

March intervals, where UAVSAR overestimated SWE at the HQ and StL sites and underestimated SWE at the FC site. For single InSAR pairs, UAVSAR ΔSWE yielded similar comparisons with ΔSWE_{sp} (RMSE = 16 mm, r = 0.65; Figure 4.3b) and ΔSWE_{ds} (RMSE = 18 mm, r = 0.55; Figure 4.3c). For reference, the overall RMSE and r for the VV 233° heading was 20 mm and 0.52 (Figure C6). When ΔSWE_{sp} was aggregated across all possible sequential intervals, the RMSE increased to 26 mm and r increased to 0.84 (Figure 4.3b). RMSE for the 052° heading InSAR pairs, compared against ΔSWE_{ds}, varied from 8 mm (20–27 January) to 28 mm (10–16 March) and overall RMSEs ranged from 18–22 mm across the four polarizations and two headings (Tables C4, C5).

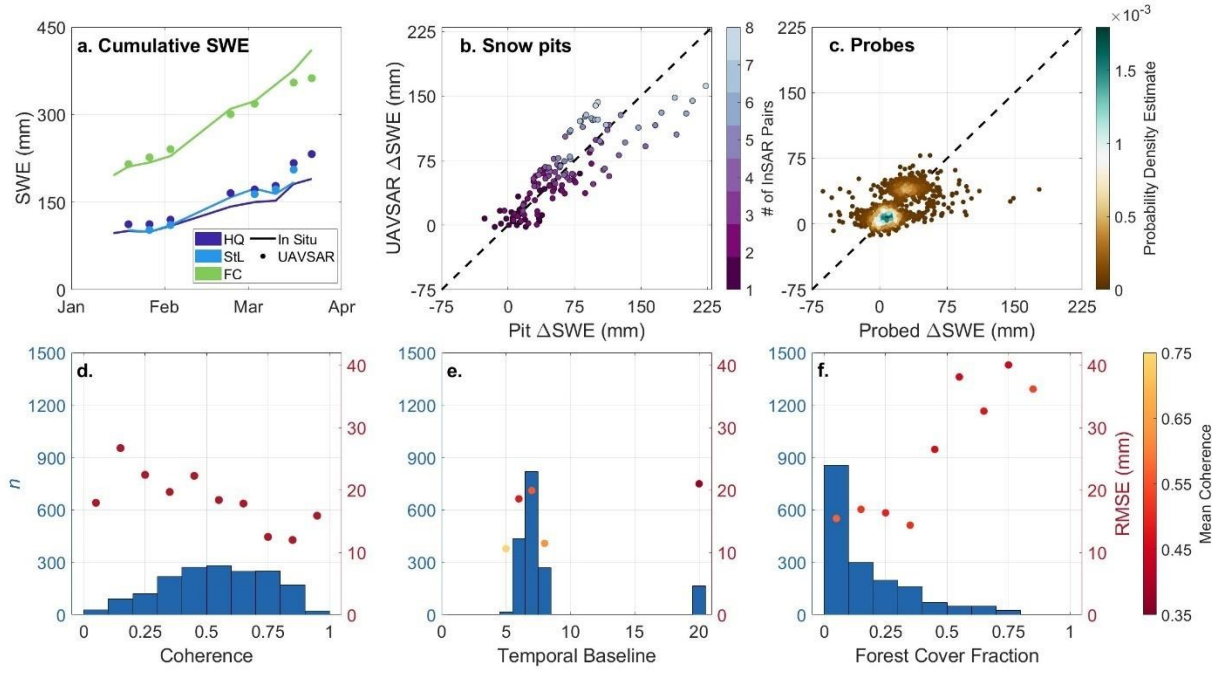

Figure 4.3: (a) Mean SWE measured/estimated from in situ measurements compared with mean integrated 052° heading UAVSAR SWE for each field site. (b) UAVSAR ΔSWE evaluated against ΔSWE_{sp} measurements, with points colored by the number of InSAR pairs that were summed for each comparison. (c) UAVSAR ΔSWE evaluated against ΔSWE estimated from ΔSWE_{ds} measurements. Histograms and RMSE for each histogram bin for (d) coherence, (e) temporal baseline, and (f) forest cover fraction. Points on e and f are colored by the mean coherence calculated within the bin.

The RMSE increased by a factor of two from high coherence to low coherence, but a trend was not observed between RMSE and temporal baseline (Figure 3d–e). RMSE increased from ~15 mm at FCF <0.40 to 26 mm for FCF between 0.40 and 0.50. RMSE approached 40 mm for FCF >0.50. UAVSAR ΔSWE retrievals yielded consistently negative residuals of –22 to –16 mm for FCF >0.50.

4.4.3 Normalized UAVSAR SWE vs. normalized lidar snow depth

Normalized UAVSAR SWE and normalized lidar depth yielded similar distribution patterns, particularly in the St. Louis Creek valley (trends SW to NE) and near higher elevations (western and southern edges; Figure 4.4a–b). However, normalized UAVSAR SWE exhibits clearly visible artifacts related to the SAR viewing geometry that are not visible in the normalized lidar depths. Normalized depth/SWE have a r = 0.35 (Figure 4.4c).

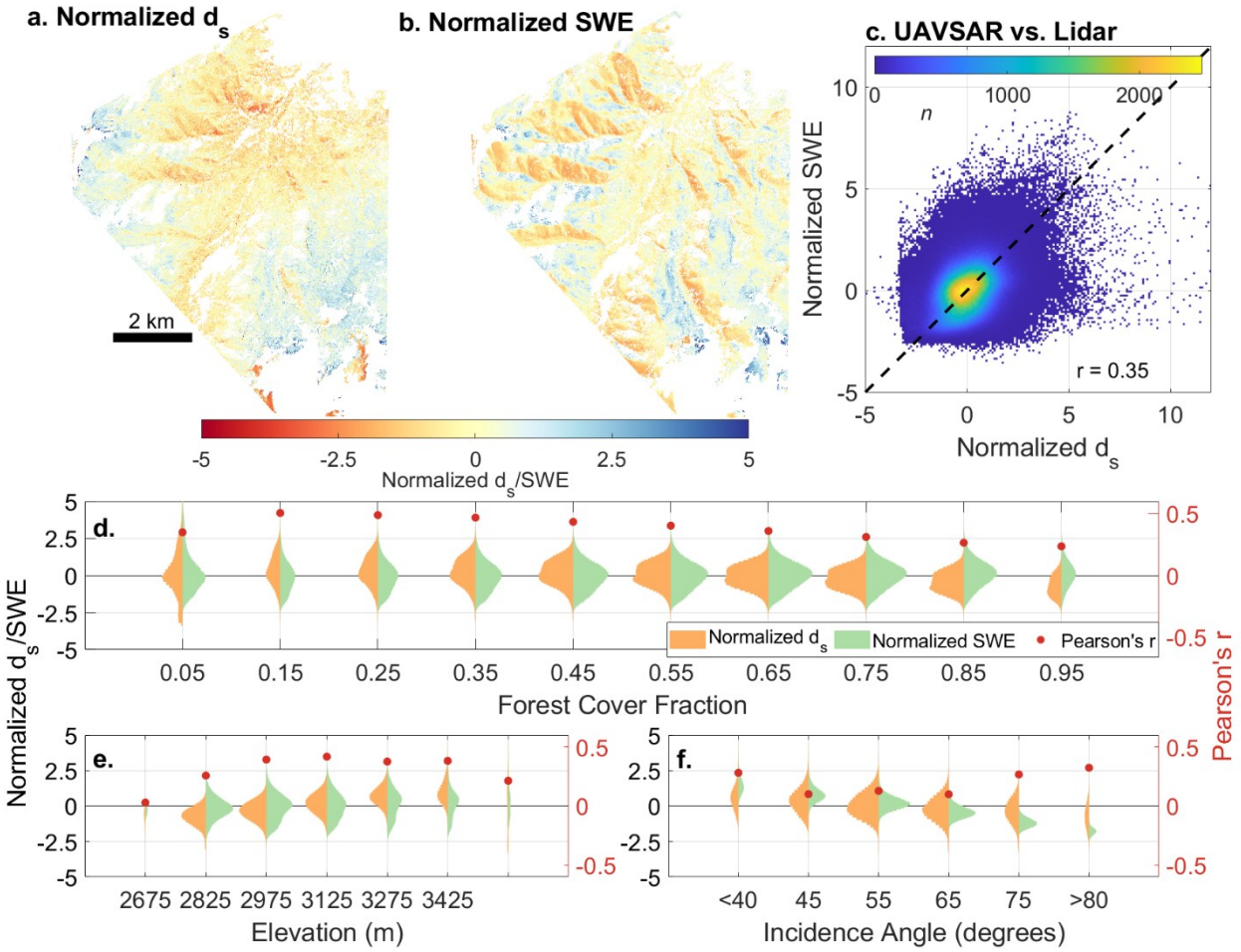

Figure 4.4: Normalized (a) lidar snow depth and (b) cumulative UAVSAR SWE, and (c) a 2-d histogram showing the comparison between the two. Violin plots showing the histogram distributions of normalized lidar snow depth and normalized UAVSAR SWE and r binned by (d) forest cover fraction, (e) elevation, and (f) UAVSAR incidence angle.

For 0.10–0.50 FCF, normalized lidar and SWE exhibit similar means and yield r of 0.43–0.51. For FCF >0.50, the distributions shift, such that mean normalized SWE is greater than mean normalized depth and correlation coefficients drop by ~0.04 per increase of 0.10 FCF. Both normalized depth and SWE increase with increasing elevation, but the distributions are offset for elevations <2900 m and >3350 m (Figure 4.4e). Finally, the distribution of normalized SWE agrees well with normalized depth at incidence angles from 50–70° (Figure 4.4f), but yield poor correlations (r = 0.10–0.13). Normalized SWE is biased positively for incidence angles

<50° and negatively for incidence angles >70°. Correlation coefficients between each of the variables are available in Table C6.

4.5 DISCUSSION

4.5.1 Applications and Limitations of L-band InSAR in montane forests

Forests challenge SWE retrieval techniques from satellite-borne sensors (e.g., Hoppinen et al., 2024b). For InSAR, the phase-center can be affected by trees and branches that shift between acquisitions (e.g., Raleigh et al., 2022) and by snow in the canopy which has different energy balance dynamics. Recent studies suggest that L-band InSAR SWE retrievals may underestimate SWE in the forests: a tower-based SAR study showed that L-band SWE retrievals over a boreal forest were biased by –93 mm for integrated 12-day retrievals (Ruiz et al., 2022) and a UAVSAR study over northern Colorado found an average ΔSWE retrieval bias from 10 InSAR pairs of –66% in the montane forests relative to the open areas, but a lack of in situ data prevented evaluation (Bonnell et al., 2024). In contrast, we found that SWE retrievals were only biased for FCF >0.50, with in situ observations and normalized lidar yielding different ΔSWE retrieval biases (–21 to –16 mm SWE vs. –0.11 to 0.80 normalized SWE; Figures 3f, 4d). However, we note that <10% of in situ observations were obtained in FCF >0.50.

It may be simpler to conclude that L-band InSAR does not work in heavily forested areas, but the polarimetric decomposition yields no detectable differences between the distributions of radar backscatter properties of any FCF interval >0.10 (Figure C7). The positive bias of normalized SWE relative to normalized snow depths at higher FCF may be explained by the presence of snow in the forest canopy. Canopy snow can cause a phase delay in the radar signal and thus be included in the ΔSWE retrieval, whereas the lidar snow depth calculation removes the tree canopy. Field surveys documented snow in the canopy at all field sites on 10 February

and 10, 17, and 22 March. Based on high resolution satellite imagery, we determined that canopy snow was spatially extensive during the last three UAVSAR flights of March (Figure C4; Planet Labs PBC, 2021). Thus, it is possible that increased snow mass in the forest canopy or snow melt in the canopy caused the positive bias for normalized SWE.

4.5.2 Implications for NISAR

The overall RMSE and correlation coefficients of the UAVSAR SWE retrievals, compared to in situ observations (RMSE = 18–26 mm; r = 0.55–0.84; Figure 4.3b–c; Tables C4–C5), fall within the range identified by previous UAVSAR studies (Bonnell et al., 2024; Hoppinen et al., 2024a; Marshall et al., 2021; Tarricone et al., 2023). Here, we use the technique's accuracy, identified by our study, and examine the utility of the L-band InSAR technique for operational SWE monitoring.

Across the study area (~62 km^2; Figure 4.1b), we calculated 2.2 million m^3 of SWE that accumulated from 15 January to 22 March for the 33% of pixels that remained after unwrapping errors and removing pixels with incidence angles <50° or >70° (Figure 4.4f). The uncertainty of this estimate, assuming dry snow conditions, is ±1.2 million m^3 of SWE, based on the reported RMSEs for FCF <0.5 and FCF >0.5 (Figure 4.3f) added in quadrature for each acquisition. The uncertainty is 19 times higher than the reported Airborne Snow Observatory uncertainty (Painter et al., 2016), but the L-band InSAR technique, will have three advantages over airborne lidar: (i) global coverage from NISAR that is (ii) repeated every 12 days, and (iii) does not require any density modeling in dry snowpacks (e.g., Leinss et al., 2015; Oveisgharan et al., 2023), which accounts for ~75% of the uncertainty in airborne lidar SWE retrievals (Raleigh & Small, 2017). Considering that the current global reanalysis products underestimate SWE by as much as 70%

and poorly represent its distribution (Broxton et al., 2016), the L-band InSAR technique offers a significant step in the right direction.

Operational ΔSWE retrievals from NISAR will be challenged by temporal coherence, modeling for atmospheric delays, and wet snow. Similar to previous studies (Bonnell et al., 2024; Tarricone et al., 2023), we found that ΔSWE retrievals can be obtained at lower coherences (<0.4), albeit with reduced accuracy (RMSE = 30–40 mm; Figure 4.3d). Low coherence effects have been addressed through filtering techniques (e.g., Lei et al., 2023) or by using wrapped phase products (e.g., Hoppinen et al., 2024a; Oveisgharan et al., 2023). Atmospheric corrections will be released with associated NISAR interferograms, but previous studies have shown that the atmospheric correction will need to be evaluated (Kirui et al., 2021). Wet snow remains a challenging problem for radar SWE retrievals because liquid water causes signal attenuation that can result in overestimates of ΔSWE (Bonnell et al., 2021; Hoppinen et al., 2024a; Tarricone et al., 2023) or complete decorrelation of the radar signal (Ruiz et al., 2022), but it may be possible to develop a L-band radar approach to identify the presence of liquid water in the snowpack (e.g., Gagliano et al., 2023; Lund et al., 2022; Park et al., 2014).

4.6 CONCLUSION

With increasing water demands from growing populations and less reliable snow water resources due to the warming climate (Hale et al., 2023; Siirila-Woodburn et al., 2021), the need for global snowpack monitoring is greater than ever. The upcoming L-band NISAR satellite mission may be the first satellite mission capable of global SWE retrievals at high spatiotemporal resolution, and it may be viable as soon as this upcoming winter. In lieu of NISAR, we evaluated repeat airborne L-band InSAR SWE retrievals collected during the nine week NASA SnowEx 2021 campaign at FEF. InSAR ΔSWE retrievals revealed complex spatial variability that

compared well with in situ measurements in open environments (FCF <0.10; RMSE = 15 mm) and in forested areas with FCF <0.40 (RMSE = 14–17 mm). However, as FCF increased above 0.50, we noted decreased ΔSWE retrieval accuracy (RMSE = 33–40 mm). Normalized InSAR integrated SWE revealed a correlation between SWE and elevation (overall r = 0.16) and identified similar statistical distributions between normalized SWE and normalized lidar snow depths for FCF <0.50 (r = 0.35–0.51). Notably, mean normalized SWE increased relative to mean normalized snow depth for FCF >0.50 and revealed correlation coefficients that declined by ~0.04 per 0.10 increase in FCF. We identified increased uncertainty for normalized SWE at incidence angles less than or exceeding 50–70°, but we note that the large range of incidence angles inherent to airborne platforms is not common for satellite platforms. We conclude that the L-band InSAR technique may have complications at FCF >0.50, but the technique remains promising for forests with sparser coverage. Thus, we consider NISAR an exciting potential development in the pursuit of global SWE retrievals.

5. CONCLUSION

GPR is gaining notoriety as a means of evaluating remote sensing methods for measuring SWE (e.g., McGrath et al., 2019; Tarricone et al., 2023). The findings presented herein further support the use of GPR for retrieving SWE over large spatial scales and at high resolution, particularly in dry snow conditions. Methodologically, GPR has clear advantages over traditional in situ sampling, with surveys that have near-continuous measurements along transect distances that are multiple km for a single surveyor on skis or snowshoes to tens of km for surveyors operating GPR on snowmobiles. Such a method is cheaper to implement than most lidar systems and several recent studies have begun testing the technique onboard UAVs, which would increase the spatial continuity and speed of GPR surveys (e.g., Valence et al., 2022). The primary detriment of GPR for SWE retrievals is in the processing time for picking the snow-ground interface two-way travel time, which was often >2 hours for lines longer than 1 km. However, recent developments towards automated picking using coherence metrics from multiple receivers show promise for future methods (Meehan et al., 2023).

In Chapter 2, I derived snowpack relative permittivity and snow density from combined lidar-measured snow depths and GPR two-way travel times of the snowpack thickness. The derived densities were then used to calculate the correlation distance of snow density and to evaluate modeled densities. Although my results for mostly linear GPR transects showed scatter for the method of density retrievals (RMSE = 54 kg m^{-3}, r = 0.09), a subsequent study at Grand Mesa found a reduced RMSE of ~30 kg m^{-3} when a gridded pattern was implemented as the survey design (Meehan et al., 2023). Densities derived from the combination of GPR and lidar are a promising method for evaluating snow density models, particularly because the method can

capture densities near-continuously at high spatial resolutions resulting in many thousands of snow density estimates, far out-competing what can be collected through in situ methods. Furthermore, no method has yet been developed that can evaluate the accuracy of spatially distributed physics-based snow density models, which are required inputs for SWE retrievals from depth-based methods and some radar backscatter methods. Thus, this method, if implemented more broadly, could help improve current remote sensing algorithms. The method will only grow more powerful as time-of-flight radars are implemented increasingly on airborne platforms (e.g., Yan et al., 2017).

In Chapters 3 and 4, I found that the L-band InSAR method for SWE retrievals has an RMSE of 18–22 mm for single InSAR pairs that aggregates to a basin wide uncertainty that is ~20 times the uncertainty of airborne lidar SWE retrievals (e.g., Painter et al., 2016). L-band InSAR was shown in Chapter 4 to be capable of extracting SWE information even under canopy cover as dense as 50% (RMSE = ~15 mm), making it a promising candidate for SWE retrievals below forest cover. The technique replicates spatial patterns that were observed in lidar SWE retrievals, with notable SWE retrieval errors at high and low incidence angles. Techniques for filtering to reduce the uncertainty have yet to be explored, so this basin-wide error may be reducible.

The snow climate explored in Chapters 3 and 4 is a dry continental climate with very few midwinter melting events and thus the results are not representative of the method's applicability over other snow climates. Thus, three key uncertainties for the L-band InSAR method that were not explored in this dissertation are: (i) the applicability of the technique for SWE retrievals when the snowpack is wet, (ii) the retrieval of SWE in steep topography, and (iii) approaches for atmospheric corrections. For NISAR, interferograms may hold coherence during the ripening

phase of the snowmelt season, as its planned dawn/dusk acquisitions will occur when liquid water content is at a minimum (Tarricone et al., 2023). However, once the snowpack has fully ripened and melt output begins, liquid water content may remain in the snowpack overnight and cause one of two things to happen: assuming coherence is maintained, either the phase-center remains at the snow-ground interface and the SWE retrievals are overestimated (Bonnell et al., 2021) or the phase-center shifts to a location mid-snowpack or at the snow-air interface because the L-band signal is increasingly attenuated by increasing liquid water in the snowpack (Naderpour et al., 2022). For regions where the snowpack is wet throughout the season, SWE retrievals may be difficult-to-impossible to produce. A method for self-detection of wet snow via L-band SAR has yet to be explored, although a study that used polarimetric decomposition from the PALSAR-2 satellite instrument (L-band) identified snow covered and snow free regions (Park et al., 2014). Perhaps there is a polarimetric difference that can be used to discern when the snow cover transitions from dry to wet. The retrieval of SWE in steep topography is an additional uncertainty for the InSAR SWE retrieval that has not been robustly explored. The original equation was derived assuming that the snowpack surface was parallel to the underlying topography (Guneriussen et al., 2001). This is not necessarily the case for steep topography, but it remains to be determined how much uncertainty this assumption adds. Finally, atmospheric corrections will be available for the NISAR datasets, but other InSAR studies have determined that many of the applicable atmospheric corrections yield contrasting results (Kirui et al., 2021), an important point to consider for SWE retrievals, given that the uncertainty of atmospheric corrections are often within the order of a few centimeters of SWE change (Gong et al., 2013). With the launch of NISAR, the opportunities to explore this technique for SWE retrievals will increase drastically.

Although the remote sensing of SWE has made significant advancements in the last decade, there is still substantial work to be done to develop a global monitoring system that captures accurate daily SWE measurements at high spatial resolutions. Regarding computing power, there is an increased need for more remote sensing datasets to be hosted for cloud optimized computing, given the increased amount of data from both optical/infrared satellites and SAR satellites. More work is needed to develop a model that can assimilate SAR datasets, because the physical properties of radar waves are sensitive to snowpack parameters. Whether L-band radar is integrated with depth-based platforms to retrieve densities or implemented for global SWE retrievals, the future of snow remote sensing is brighter with contributions from L-band radar techniques.

REFERENCES

Adebisi, N., Marshall, H., O'Neel, S., Vuyovich, C. M., Hiemstra, C., & Elder, K. (2022). SnowEx20-21 QSI Lidar DEM 0.5m UTM Grid, Version 1 [Data Set]. Boulder, Colorado, USA. NASA National Snow and Ice Data Center Distributed Active Archive Center. https://doi.org/10.5067/YO583L7ZOLOO

Adebisi, N., Marshall, H., Vuyovich, C. M., Elder, K., Hiemstra, C., & Durand, M. (2022). SnowEx20-21 QSI Lidar Snow Depth 0.5m UTM Grid, Version 1 [Data Set]. Boulder, Colorado, USA. NASA National Snow and Ice Data Center Distributed Active Archive Center. Retrieved 11-01-2022. https://doi.org/10.5067/VBUN16K365DG.

Adebisi, N., Marshall, H., Vuyovich, C. M., Elder, K., Hiemstra, C. & Durand, M. (2022). SnowEx20-21 QSI Lidar Vegetation Height 0.5m UTM Grid, Version 1 [data set]. Boulder, Colorado USA. NASA National Snow and Ice Data Center Distributed Active Archive Center. https://doi.org/10.5067/8RBIUIPEUJ7Z

Alexander, R. & Watkins, R. (1977). The Fraser Experimental Forest, CO. USDA Forest Service. General Technical Report, RM-40, 39 pp.

Alford, D. (1967). Density Variations in Alpine Snow. Journal of Glaciology, 6(46), 495–503. https://doi.org/10.3189/S0022143000019717

Anderson, B. T., McNamara, J. P., Marshall, H.-P., & Flores, A. N. (2014). Insights into the physical processes controlling correlations between snow distribution and terrain properties. Water Resources Research, 50(6), 4545–4563. https://doi.org/10.1002/2013WR013714

Avanzi, F., & De Michele, C. (2015). ON THE PERFORMANCES OF EMPIRICAL REGRESSIONS FOR THE ESTIMATION OF BULK SNOW DENSITY. Geografia Fisica e Dinamica Quaternaria, 38.2, 105–112. https://doi.org/10.4461/GFDQ.2015.38.10

Barnett, T. P., Adam, J. C., & Lettenmaier, D. P. (2005). Potential impacts of a warming climate on water availability in snow-dominated regions. Nature, 438(7066), Article 7066. https://doi.org/10.1038/nature04141

Barrett, A. P. (2003) National Operational Hydrologic Remote Sensing Center SNOw Data Assimilation System (SNODAS) Products at NSIDC. NSIDC Special Report 11. Boulder, Colorado, USA: National Snow and Ice Data Center.

Bauer, M. A., Burgess, M. A., Adams, J. D., Sexstone, G. A., Fulton, J. W., McDermott, W. R., & Brady, L.R. (2023). Lidar Point Clouds (LPCs), Digital Elevation Models (DEMs), and Snow Depth Raster Maps Derived from Lidar Data Collected on Small, Uncrewed Aircraft Systems in the Upper Colorado River Basin, Colorado, 2020-22: U.S. Geological Survey data release. https://doi.org/10.5066/P9LF15AE

Besso, H., Shean, D., and Lundquist, J. D. (2024). Mountain snow depth retrievals from customized processing of ICESat-2 satellite laser altimetry, Remote Sensing of Environment, 300, 113843. https://doi.org/10.1016/j.rse.2023.113843

Bevis, M., Businger, S., Herring, T. A., Rocken, C., Anthes, R. A., and Ware, R. H. (1992). GPS meteorology: Remote sensing of atmospheric water vapor using the global positioning system, Journal of Geophysical Research: Atmospheres, 97, 15787–15801. https://doi.org/10.1029/92JD01517

Bisset, R., Floyd, B.C., Menounos, B., Bishop, A., Cebulski, A., Fisk, G., Marchenko, S., & Marshall, P. (2022). Quantifying Spatio-Temporally Distributed Snow Density across

Four Forested Mountain Watersheds in South-Western British Columbia. American Geophysical Union Fall Meeting 2022, Chicago, Il. Poster.

Bonnell, R., & McGrath, D. (2023). Ranch Creek Ground-Penetrating Radar Snow Survey April 07, 2021 [Data Set]. HydroShare. https://doi.org/10.4211/hs.6f39721f1643428f84997f09ef75e2f8

Bonnell, R., McGrath, D., Hedrick, A. R., Trujillo, E., Meehan, T. G., Williams, K., Marshall, H.-P., Sexstone, G., Fulton, J., Ronayne, M. J., Fassnacht, S. R., Webb, R. W., and Hale, K. E. (2023). Snowpack relative permittivity and density derived from near-coincident lidar and ground-penetrating radar, Hydrological Processes, 37, e14996. https://doi.org/10.1002/hyp.14996

Bonnell, R., McGrath, D., Williams, K., Webb, R., Fassnacht, S. R., & Marshall, H.-P. (2021). Spatiotemporal Variations in Liquid Water Content in a Seasonal Snowpack: Implications for Radar Remote Sensing. Remote Sensing, 13(21), Article 21. https://doi.org/10.3390/rs13214223

Bonnell, R., McGrath, D., Zeller, L., Bump, E., & Olsen-Mikitowicz, A. (2022). SnowEx21 Cameron Pass Ground Penetrating Radar, Version 1 [Data Set]. Boulder, Colorado USA. NASA National Snow and Ice Data Center Distributed Active Archive Center. Retrieved 01 December 2022. https://doi.org/10.5067/SRWGLYCB6ZC4.

Bonner, H. M., Raleigh, M. S., & Small, E. E. (2022). Isolating forest process effects on modelled snowpack density and snow water equivalent. Hydrological Processes, 36(1), e14475. https://doi.org/10.1002/hyp.14475

Borah, F. K., Tsang, L., and Kim, E. (2023). SWE Retrieval Algorithms Based on the Parameterized BI-Continuous DMRT Model Without Priors on Grain Size Or Scattering

Albedo, Progress in Electromagnetics Research, 178, 129-147. https://doi.org/10.2528/PIER23071101

Bourgoin, C., Ameztoy, I., Verhegghen, A., Carboni, S., Colditz, R. R., Achard, F. (2023). Global map of forest cover 2020 - version 1. *European Commission, Joint Research Center* [data set]. http://data.europa.eu/89h/10d1b337-b7d1-4938-a048-686c8185b290

Bradford, J. H., Harper, J. T., & Brown, J. (2009). Complex Dielectric Permittivity Measurements from Ground-Penetrating Radar Data to Estimate Snow Liquid Water Content in the Pendular Regime. Water Resources Research, 45(8). https://doi.org/10.1029/2008WR007341

Brangers, I., Marshall, H.-P., De Lannoy, G., Dunmire, D., Matzler, C., and Lievens, H. (2023). Tower-based C-band radar measurements of an alpine snowpack, EGUsphere, 1–25. https://doi.org/10.5194/egusphere-2023-2927

Broxton, P., Ehsani, M. R., & Behrangi, A. (2024). Improving Mountain Snowpack Estimation Using Machine Learning With Sentinel-1, the Airborne Snow Observatory, and University of Arizona Snowpack Data. *Earth and Space Science*, *11*(3), e2023EA002964. https://doi.org/10.1029/2023EA002964

Broxton, P. D., Zeng, X., & Dawson, N. (2016). Why Do Global Reanalyses and Land Data Assimilation Products Underestimate Snow Water Equivalent? Journal of Hydrometeorology, 17(11), 2743–2761. https://doi.org/10.1175/JHM-D-16-0056.1

Buchhorn, M., Smets, B., Bertels, L., Roo, B. D., Lesiv, M., Tsendbazar, N.-E., Herold, M., and Fritz, S. (2020). Copernicus Global Land Service: Land Cover 100m: collection 3: epoch 2019: Globe (Version V3.0.1), Zenodo [data set]. https://doi.org/10.5281/zenodo.393050

Cline, D., Yueh, S., Chapman, B., Stankov, B., Gasiewski, A., Masters, D., Elder, K., Kelly, R., Painter, T. H., Miller, S., Katzberg, S., & Mahrt, L. (2009). NASA Cold Land Processes Experiment (CLPX 2002/03): Airborne Remote Sensing. *Journal of Hydrometeorology* 10(1), 338-348. https://doi.org/10.1175/2008JHM883.1

Cloude, S. R., & Pottier, E. (1997). An entropy based classification scheme for land applications of polarimetric SAR. *IEEE Transactions on Geoscience and Remote Sensing*, *35*(1), 68–78. https://doi.org/10.1109/36.551935

Clow, D. W., Nanus, L., Verdin, K. L., & Schmidt, J. (2012). Evaluation of SNODAS snow depth and snow water equivalent estimates for the Colorado Rocky Mountains, USA. Hydrological Processes, 26(17), 2583–2591. https://doi.org/10.1002/hyp.9385

Conde, V., Nico, G., Mateus, P., Catalão, J., Kontu, A., and Gritsevich, M. (2019). On The Estimation of Temporal Changes of Snow Water Equivalent by Spaceborne Sar Interferometry: A New Application for the Sentinel-1 Mission, Journal of Hydrology and Hydromechanics, 67, 93–100. https://doi.org/10.2478/johh-2018-0003

Currier, W. R., Pflug, J., Mazzotti, G., Jonas, T., Deems, J. S., Bormann, K. J., Painter, T. H., Hiemstra, C. A., Gelvin, A., Uhlmann, Z., Spaete, L., Glenn, N. F., & Lundquist, J. D. (2019). Comparing Aerial Lidar Observations With Terrestrial Lidar and Snow-Probe Transects From NASA's 2017 SnowEx Campaign. Water Resources Research, 55(7), 6285–6294. https://doi.org/10.1029/2018WR024533

Daniels, D. J. (Ed.). (2004). Ground Penetrating Radar (Vol. 1). The Institution of Electrical Engineers: London, UK.

Deeb, E. J., Forster, R. R., & Kane, D. L. (2011). Monitoring snowpack evolution using interferometric synthetic aperture radar on the North Slope of Alaska, USA. International

Journal of Remote Sensing, 32(14), 3985–4003. https://doi.org/10.1080/01431161003801351

Deems, J. S., Painter, T. H., & Finnegan, D. C. (2013). Lidar measurement of snow depth: A review. Journal of Glaciology, 59(215), 467–479. https://doi.org/10.3189/2013JoG12J154

De Roo, R. D., Chang, A., & England, A. W. (2007). Radiobrightness at 6.7-, 19- and 37-GHz downwelling from mature evergreen trees observed during the Cold Lands Processes Experiment in Colorado. *IEEE Transactions on Geoscience and Remote Sensing*, *45*(10), 3224–3229. https://doi.org/10.1109/TGRS.2007.900688

Deschamps-Berger, C., Gascoin, S., Berthier, E., Deems, J., Gutmann, E., Dehecq, A., Shean, D., & Dumont, M. (2020). Snow depth mapping from stereo satellite imagery in mountainous terrain: Evaluation using airborne laser-scanning data. *The Cryosphere*, *14*(9), 2925–2940. https://doi.org/10.5194/tc-14-2925-2020

Di Paolo, F., Cosciotti, B., Lauro, S. E., Mattei, E., & Pettinelli, E. (2020). A critical analysis on the uncertainty computation in ground-penetrating radar-retrieved dry snow parameters. Geophysics, 85(4), H39–H49. https://doi.org/10.1190/geo2019-0683.1

Dietz, A. J., Kuenzer, C., Gessner, U., & Dech, S. (2012). Remote sensing of snow – a review of available methods. International Journal of Remote Sensing, 33(13), 4094–4134. https://doi.org/10.1080/01431161.2011.640964

Dozier, J. (1989). Spectral signature of alpine snow cover from the landsat thematic mapper, Remote Sensing of Environment, 28, 9–22. https://doi.org/10.1016/0034-4257(89)90101-6

Dozier, J., Bair, E. H., & Davis, R. E. (2016). Estimating the spatial distribution of snow water equivalent in the world's mountains. WIREs Water, 3(3), 461–474. https://doi.org/10.1002/wat2.1140

Durand, M., Gatebe, C., Kim, E., Molotch, N., Painter, T. H., Raleigh, M., Sandells, M., & Vuyovich, C. (2018). NASA SnowEx Science Plan: Assessing approaches for measuring water in Earth's Seasonal Snow, version 1.6.

Elder, K., Cline, D., Liston, G. E., & Armstrong, R. (2009). NASA Cold Land Processes Experiment (CLPX 2002/03): Field Measurements of Snowpack Properties and Soil Moisture. *Journal of Hydrometeorology*, *10*(1), 320–329. https://doi.org/10.1175/2008JHM877.1

Elder, K., Brucker, L., Hiemstra, C., & Marshall, H. (2018). SnowEx17 Community Snow Pit Measurements, Version 1 [Data Set]. Boulder, Colorado USA. NASA National Snow and Ice Data Center Distributed Active Archive Center. Retrieved 1 August 2020. https://doi.org/10.5067/Q0310G1XULZS

Enderlin, E. M., Elkin, C. M., Gendreau, M., Marshall, H. P., O'Neel, S., McNeil, C., Florentine, C., & Sass, L. (2022). Uncertainty of ICESat-2 ATL06- and ATL08-derived snow depths for glacierized and vegetated mountain regions. Remote Sensing of Environment, 283, 113307. https://doi.org/10.1016/j.rse.2022.113307

ESRI (2023). ArcGIS Pro v3.1.2 [Software]. Available at: https://www.esri.com/en-us/arcgis/products/arcgis-pro/overview. Accessed 25 May 2022.

European Space Agency (2021) Copernicus Global Digital Elevation Model, Distributed by Google Earth Engine [data set]. https://doi.org/10.5270/ESA-c5d3d65

European Space Agency (2022). Copernicus Sentinel data, Distributed by Google Earth Engine [data set]. https://doi.or/10.5270/S2_-6eb6imz

Fassnacht, S. R. (2021). A Call for More Snow Sampling. Geosciences, 11, 435. https://doi.org/10.3390/geosciences11110435

Fassnacht, S. R., Brown, K. S. J., Blumberg, E. J., López-Moreno, J. I., Covino, T. P., Kappas, M., Huang, Y., Leone, V., & Kashipazha, A. H. (2018). Distribution of snow depth variability. Frontiers of Earth Science, 12, 683-692. https://doi.org/10.1007/s11707-018-0714-z

Fassnacht, S. R., Heun, C. M., López-Moreno, J. I., & Latron, J. (2010). Snow Density Variability in the Rio Esera Valley, Pyrenees Mountains, Spain. Hydrology Days 2010. Paper.

Fassnacht, S. R., Venable, N. B., McGrath, D., and Patterson, G. G. (2018). Sub-seasonal snowpack trends in the Rocky Mountain National Park area, Colorado, USA, Water, 10, 562. https://doi.org/10.3390/w10050562

Feng, T., Hao, X., Wang, J., Luo, S., Huang, G., Li, H., and Zhao, Q. (2023). Applicability of alpine snow depth estimation based on multitemporal UAV-LiDAR data: A case study in the Maxian Mountains, Northwest China, Journal of Hydrology, 617, 129006. https://doi.org/10.1016/j.jhydrol.2022.129006

Fleming, S. W., Zukiewicz, L., Strobel, M. L., Hofman, H., & Goodbody, G. G. (2023). SNOTEL, the soil climate analysis network, and water supply forecasting at the natural resources conservation service: Past, present, and future. JAWRA Journal of the American Water Resources Association, *59*, 585-599. https://doi.org/10.1111/1752-1688.13104

Foster, J. L., Hall, D. K., Chang, A. T. C., & Rango, A. (1984). An overview of passive microwave snow research and results. *Reviews of Geophysics*, *22*(2), 195–208. https://doi.org/10.1029/RG022i002p00195

Gagliano, E., Shean, D., Henderson, S., and Vanderwilt, S. (2023). Capturing the Onset of Mountain Snowmelt Runoff Using Satellite Synthetic Aperture Radar, Geophysical Research Letters, 50, e2023GL105303. https://doi.org/10.1029/2023GL105303

Gleason, K. E., Bradford, J. B., D'Amato, A. W., Fraver, S., Palik, B. J., & Battaglia, M. A. (2021). Forest density intensifies the importance of snowpack to growth in water-limited pine forests. *Ecological Applications*, *31*(1), e02211. https://doi.org/10.1002/eap.2211

Goldstein, R. M., and Werner, C. L. (1998). Radar interferogram filtering for geophysical applications, Geophysical Research Letters, 25, 4035-4038. https://doi.org/10.1029/1998GL900033

Gong, W., Meyer, F. J., Webley, P., and Morton, D. (2013). Performance of the high-resolution atmospheric model HRRR-AK for correcting geodetic observations from spaceborne radars, J Geophys Res Atmos, 118, 11611–11624. https://doi.org/10.1002/2013JD020170

Gorelick, N., Hancher, M., Dixon, M., Ilyushchenko, S., Thau, D., and Moore, R. (2017). Google Earth Engine: Planetary-scale geospatial analysis for everyone, Remote Sensing of Environment, 202, 18–27. https://doi.org/10.1016/j.rse.2017.06.031

Griessinger, N., Mohr, F., & Jonas, T. (2018). Measuring snow ablation rates in alpine terrain with a mobile multioffset ground-penetrating radar system. Hydrological Processes, 32(21), 3272–3282. https://doi.org/10.1002/hyp.13259

Guneriussen, T., Hogda, K. A., Johnsen, H., & Lauknes, I. (2001). InSAR for estimation of changes in snow water equivalent of dry snow. IEEE Transactions on Geoscience and Remote Sensing, 39(10), 2101–2108. https://doi.org/10.1109/36.957273

Hale, K., Kiewiet, L., Trujillow, E., Krohe, C., Hedrick, A., Marks, D., Kormos, P., Havens, S., McNamara, J., Link, T., Godsey, S. E. (2023). Drivers of spatiotemporal patterns of surface water inputs in a catchment at the rain-snow transition zone of the water-limited western United States. Journal of Hydrology, 616, 128699. https://doi.org/10.1016/j.jhydrol.2022.128699

Hammond, J. C., Saavedra, F. A., & Kampf, S. K. (2018). Global snow zone maps and trends in snow persistence 2001–2016. International Journal of Climatology, 38(12), 4369–4383. https://doi.org/10.1002/joc.5674

Hardy, J., Davis, R., Koh, Y., Cline, D., Elder, K., Armstrong, R., Marshall, H.-P., Painter, T., Saint-Martin, G. C., DeRoo, R., Sarabandi, K., Graf, T., Koike, T., & McDonald, K. (2008). NASA Cold Land Processes Experiment (CLPX 2002/03): Local Scale Observation Site. *Journal of Hydrometeorology*, *9*(6), 1434–1442. https://doi.org/10.1175/2008JHM875.1

Havens, S., Marks, D., Sandusky, M., Hedrick, A., Johnson, M., Robertson, M., & Trujillo, E. (2020). Automated Water Supply Model (AWSM): Streamlining and standardizing application of a physically based snow model for water resources and reproducible science. Computers & Geosciences, 144, 104571. https://doi.org/10.1016/j.cageo.2020.104571

Hedrick, A., Marshall, H.-P., Winstral, A., Elder, K., Yueh, S., & Cline, D. (2015). Independent evaluation of the SNODAS snow depth product using regional-scale lidar-derived measurements. The Cryosphere, 9(1), 13–23. https://doi.org/10.5194/tc-9-13-2015

Hedrick, A. R., Marks, D., Havens, S., Robertson, M., Johnson, M., Sandusky, M., Marshall, H.-P., Kormos, P. R., Bormann, K. J., & Painter, T. H. (2018). Direct Insertion of NASA Airborne Snow Observatory-Derived Snow Depth Time Series Into the iSnobal Energy Balance Snow Model. Water Resources Research, 54(10), 8045–8063. https://doi.org/10.1029/2018WR023190

Heilig, A., Mitterer, C., Schmid, L., Wever, N., Schweizer, J., Marshall, H.-P., & Eisen, O. (2015). Seasonal and diurnal cycles of liquid water in snow—Measurements and modeling. Journal of Geophysical Research: Earth Surface, 120(10), 2139–2154. https://doi.org/10.1002/2015JF003593

Holbrook, W. S., Miller, S. N., & Provart, M. A. (2016). Estimating snow water equivalent over long mountain transects using snowmobile-mounted ground-penetrating radar. Geophysics, 81, WA183-WA193. https://doi.org/10.1190/geo2015-0121.1

Hoppinen, Z. M., Oveisgharan, S., Marshall, H.-P., Mower, R., Elder, K., & Vuyovich, C. (2024). Snow Water Equivalent Retrieval Over Idaho - Part 2: Using L-band UAVSAR Repeat-Pass Interferometry. The Cryosphere, 18, 575-592. https://doi.org/10.5194/tc-18-575-2024

Hoppinen, Z., & Tarricone, J (2022). uavsar_pytools (Version 0.7.0), Zenodo [code]. https://doi.org/10.5281/zenodo.6789624

Hoppinen, Z., Palomaki, R. T., Brencher, G., Dunmire, D., Gagliano, E., Marziliano, A., Tarricone, J., & Marshall, H.-P. (2024). Evaluating Snow Depth Retrievals from Sentinel-1 Volume Scattering over NASA SnowEx Sites. *EGUsphere* [Preprint].

Huckaby, L. S. & Moir, W. H. (1998). Forest communities at Fraser Experimental Forest, Colorado. The Southwestern Naturalist, 204-218.

Hu, J. M., Shean, D., and Bhushan, S. (2023). Six Consecutive Seasons of High-Resolution Mountain Snow Depth Maps From Satellite Stereo Imagery, Geophysical Research Letters, 50, e2023GL104871. https://doi.org/10.1029/2023GL104871

Hu, Z. and Mallorquí, J. J. (2019). An Accurate Method to Correct Atmospheric Phase Delay for InSAR with the ERA5 Global Atmospheric Model, Remote Sensing, 11, 1969. https://doi.org/10.3390/rs11171969

Isaaks, E. H. & Srivastava, R. M. (1989). Applied Geostatistics (Vol. 561). New York: Oxford University Press.

ISRO Space Applications Centre (2023). NISAR Utilisation Programme: Announcement inviting project proposals from Indian researchers, Utilization Programme Document, 36 pp.

Jonas, T., Marty, C., & Magnusson, J. (2009). Estimating the snow water equivalent from snow depth measurements in the Swiss Alps. Journal of Hydrology, 378(1), 161–167. https://doi.org/10.1016/j.jhydrol.2009.09.021

Jones, C. E., An, K., Blom, R. G., Kent, J. D., Ivins, E. R., and Bekaert, D. (2016). Anthropogenic and geologic influences on subsidence in the vicinity of New Orleans, Louisiana, Journal of Geophysical Research: Solid Earth, 121, 3867–3887. https://doi.org/10.1002/2015JB012636

Kiewiet, L., Trujillow, E., Hedrick, A., Havens, S., Hale, K., Seyfried, M., Kampf, S., & Godsey, S. (2022). Effects of spatial and temporal variability in surface water inputs on streamflow generation and cessation in the rain–snow transition zone. Hydrology and Earth System Sciences, 26(10), 2779-2796. https://doi.org/10.5194/hess-26-2779-2022

Kim, E. (2018). How Can We Find Out How Much Snow Is in the World? Eos. http://eos.org/science-updates/how-can-we-find-out-how-much-snow-is-in-the-world

Koch, F., Prasch, M., Schmid, L., Schweizer, J., & Mauser, W. (2014). Measuring Snow Liquid Water Content with Low-Cost GPS Receivers. Sensors, 14(11), Article 11. https://doi.org/10.3390/s141120975

Kovacs, A., Gow, A. J., & Morey, R. M. (1995). The in-situ dielectric constant of polar firn revisited. Cold Regions Science and Technology, 23(3), 245–256. https://doi.org/10.1016/0165-232X(94)00016-Q

Kuroiwa, D. (1954). The dielectric property of snow. International Association of Hydrological Sciences Publication.

Largeron, C., Dumont, M., Morin, S., Boone, A., Lafaysse, M., Metref, S., Cosme, E., Jonas, T., Winstral, A., & Margulis, S. A. (2020). Toward Snow Cover Estimation in Mountainous Areas Using Modern Data Assimilation Methods: A Review. Frontiers in Earth Science, 8. https://www.frontiersin.org/articles/10.3389/feart.2020.00325

Lehning, M., Bartelt, P., Brown, B., Fierz, C., & Satyawali, P. (2002b). A physical SNOWPACK model for the Swiss avalanche warning: Part II: Snow microstructure. Cold Regions Science and Technology, 35(3), 147-167. https://doi.org/10.1016/S0165-232X(02)00073-3

Lehning, M., Bartelt, P., Brown, B., & Fierz, C. (2002a). A physical SNOWPACK model for the Swiss avalanche warning: Part III: meteorological forcing, thin layer formation and evaluation. Cold Regions Science and Technology, 35(3), 169-184. https://doi.org/10.1016/S0165-232X(02)00072-1

Leinss, S., Parrella, G., and Hajnsek, I (2014). Snow height determination by polarimetric phase differences in X-band SAR data. IEEE Journal of Selected Topics in Applied Earth Observations and Remote Sensing, 7, 3794-3810. https://doi.org/10.1109/JSTARS.2014.2323199

Leinss, S., Wiesmann, A., Lemmetyinen, J., and Hajnsek, I. (2015). Snow water equivalent of dry snow measured by differential interferometry, IEEE Journal of Selected Topics in Applied Earth Observations and Remote Sening, 8, 3773-3790. https://doi.org/10.1109/JSTARS.2015.2432031

Lei, Y., Shi, J., Liang, C., Werner, C., & Siqueira, P. (2023). Snow Water Equivalent Retrieval Using Spaceborne Repeat-Pass L-Band SAR Interferometry Over Sparse Vegetation Covered Regions. *IGARSS 2023 - 2023 IEEE International Geoscience and Remote Sensing Symposium*, 852–855. https://doi.org/10.1109/IGARSS52108.2023.10282234

Lei, Y. Xu, X., Baldi, C., De Bleser, J.W., Xu, X., Yueh, S., Esteban_Fernandez, D., Elder,K., Starr, B., & Siqueira, P. (2022). Dry Snow Parameter Retrieval With Ground-Based Single-Pass Synthetic Aperture Radar Interferometry. *IEEE Transactions on Geoscience and Remote Sensing*, *60*, pp. 1-14. https://doi.org/10.1109/TGRS.2022.3171269

Li, D., Wrzesien, M. L., Durand, M., Adam, J., and Lettenmaier, D. P. (2017). How much runoff originates as snow in the western United States, and how will that change in the future?,

Geophysical Research Letters, 44, 6163-6172, https://doi.org/10.1002/2017GL073551, 2017.

Lievens, H., Brangers, I., Marshall, H.-P., Jonas, T., Olefs, M., & De Lannoy, G. (2022). Sentinel-1 snow depth retrieval at sub-kilometer resolution over the European Alps. The Cryosphere, 16(1), 159–177. https://doi.org/10.5194/tc-16-159-2022

Lievens, H., Demuzere, M., Marshall, H.-P., Reichle, R. H., Brucker, L., Brangers, I., de Rosnay, P., Dumont, M., Girotto, M., Immerzeel, W. W., Jonas, T., Kim, E. J., Koch, I., Marty, C., Saloranta, T., Schöber, J., & De Lannoy, G. J. M. (2019). Snow depth variability in the Northern Hemisphere mountains observed from space. Nature Communications, 10(1), Article 1. https://doi.org/10.1038/s41467-019-12566-y

Livneh, B., & Badger, A. M. (2020). Drought less predictable under declining future snowpack. *Nature Climate Change*, *10*(5), Article 5. https://doi.org/10.1038/s41558-020-0754-8

Li, Y., Zhao, X., and Zhao, Q. (2022). Snow Depth Inversion in Forested Areas from Sentinel-1 Data Based on Phase Deviation Correction, Remote Sensing, 14, 5930. https://doi.org/10.3390/rs14235930

López-Moreno, J. I., Fassnacht, S. R., Heath, J. T., Musselman, K. N., Revuelto, J., Latron, J., Morán-Tejeda, E., & Jonas, T. (2013). Small scale spatial variability of snow density and depth over complex alpine terrain: Implications for estimating snow water equivalent. Advances in Water Resources, 55, 40–52. https://doi.org/10.1016/j.advwatres.2012.08.010

López-Moreno, J. I., Leppänen, L., Luks, B., Holko, L., Picard, G., Sanmiguel-Vallelado, A., Alons- González, E., Finger, D. C., Arslan, A. N., Gillemot, K., Sensory, A., Sorman, A., Ertas, M. C., Fassnacht, S. R., Fierz, C., & Marty, C. (2020). Intercomparison of

measurements of bulk snow density and water equivalent of snow cover with snow core samplers: Instrumental bias and variability induced by observers. Hydrological Processes, 34, 3120-3133. https://doi.org/10.1002/hyp.13785

Lorenzi, V., Banzato, F., Barberio, M. D., Goeppert, N., Goldscheider, N., Gori, F., Lacchini, A., Manetta, M., Medici, G., Rusi, S., and Petitta, M. (2024). Tracking flowpaths in a complex karst system through tracer test and hydrogeochemical monitoring: Implications for groundwater protection (Gran Sasso, Italy), Heliyon, 10, e24663. https://doi.org/10.1016/j.heliyon.2024.e24663

Lundberg, A., Richardson-Näslund, C., & Andersson, C. (2006). Snow density variations: Consequences for ground-penetrating radar. Hydrological Processes, 20(7), 1483–1495. https://doi.org/10.1002/hyp.5944

Lund, J., Forster, R. R., Deeb, E. J., Liston, G. E., Skiles, S. M., & Marshall, H.-P. (2022). Interpreting Sentinel-1 SAR Backscatter Signals of Snowpack Surface Melt/Freeze, Warming, and Ripening, through Field Measurements and Physically-Based SnowModel. *Remote Sensing*, *14*(16), Article 16. https://doi.org/10.3390/rs14164002

Lv, Z., Pomeroy, J., Fang, X. (2019). Evaluation of SNODAS Snow Water Equivalent in Western Canada and Assimilation into a Cold Region Hydrological Model. Water Resources Research, 55(12), 11166-11187. https://doi.org/10.1029/2019WR025333

Mankin, J. S., Viviroli, D., Singh, D., Hoekstra, A. Y., & Diffenbaugh, N. S. (2015). The potential for snow to supply human water demand in the present and future. Environmental Research Letters, 10(11), 114016. https://doi.org/10.1088/1748-9326/10/11/114016

Marks, D., Domingo, J., Susong, D., Link, T., Garen, D. (1999). A Spatially Distributed Energy Balance Snowmelt Model for Application in Mountain Basins. Hydrological Processes, 13(12-13), 1935-1959, https://doi.org/10.1002/(SICI)1099-1085(199909)13:12/13<1935::AID-HYP868>3.0.CO;2-C

Marshall, H. P., Deeb, E., Forster, R., Vuyovich, C., Elder, K., Hiemstra, C., & Lund, J. (2021). L-Band InSAR Depth Retrieval During the NASA SnowEx 2020 Campaign: Grand Mesa, Colorado. 2021 IEEE International Geoscience and Remote Sensing Symposium IGARSS, 625–627. https://doi.org/10.1109/IGARSS47720.2021.9553852

Marshall, H.-P., Koh, G., & Forster, R. R. (2005). Estimating alpine snowpack properties using FMCW radar. Annals of Glaciology, 40, 157–162. https://doi.org/10.3189/172756405781813500

Marshall, H.-P., Vuyovich, C., Hiemstra, C., Brucker, L., Elder, K., Deems, J., et al. (2019). NASA SnowEx 2020 Experiment Plan (Science Plan).

Marshall, H. P., Vuyovich, C., Skiles, M., Sproles, E., Gleason, K., & Elder, K. (2020). NASA SnowEx 2021 Experiment Plan [Science plan], 77 pp. https://snow.nasa.gov/sites/default/files/users/user194/NASASnowEx21_ExperimentPlan_draft_v02.pdf

Marti, R., Gascoin, S., Berthier, E., de Pinel, M., Houet, T., & Laffly, D. (2016). Mapping snow depth in open alpine terrain from stereo satellite imagery. *The Cryosphere*, *10*(4), 1361–1380. https://doi.org/10.5194/tc-10-1361-2016

Matzler, C. (1996). Microwave permittivity of dry snow. IEEE Transactions on Geoscience and Remote Sensing, 34, 573-581. https://doi.org/10.1109/36.485133

Mason, M., Marshall, H., Craaybeek, D., Elder, K., & Vuyovich, C. M. (2024). SnowEx21 Time Series Snow Pits, Version 1 [data set]. Boulder, Colorado USA. NASA National Snow and Ice Data Center Distributed Active Archive Center. https://doi.org/10.5067/QIANJYJGRWOV

Mason, M., Marhsall, H., McCormick, M., Craaybeek, D., Elder, K., & Vuyovich, C. M. (2023). SnowEx20 Time Series Snow Pit Measurements, Version 1 [Data Set]. Boulder, Colorado, USA. NASA National Snow and Ice Data Center Distributed Active Archive Center. Retrieved 15 May 2023. https://doi.org/10.5067/POT9E0FFUUD1

McCreight, J. L., & Small, E. E. (2014). Modeling bulk density and snow water equivalent using daily snow depth observations. The Cryosphere, 8(2), 521–536. https://doi.org/10.5194/tc-8-521-2014

McCrystall, M. R., Stroeve, J., Serreze, M., Forbes, B. C., and Screen, J. A. (2021). New climate models reveal faster and larger increases in Arctic precipitation than previously projected, Nat Commun, 12, 6765. https://doi.org/10.1038/s41467-021-27031-y

McGrath, D., Bonnell, R., Olsen-Mikitowicz, A., Duncan, C., & Grabowski, J. (2021). SnowEx20 Cameron Pass Ground Penetrating Radar, Version 1 [Data Set]. Boulder, Colorado USA. NASA National Snow and Ice Data Center Distributed Active Archive Center. Retrieved 13 April 2021. https://doi.org/10.5067/U4Q3X27BMRR4.

McGrath, D., Bonnell, R., Zeller, L., Olsen-Mikitowicz, A., Bump, E., Webb, R., & Marshall, H.-P. (2022). A Time Series of Snow Density and Snow Water Equivalent Observations Derived From the Integration of GPR and UAV SfM Observations. Frontiers in Remote Sensing, 3. https://www.frontiersin.org/articles/10.3389/frsen.2022.886747

McGrath, D., Webb, R., Shean, D., Bonnell, R., Marshall, H.-P., Painter, T. H., Molotch, N. P., Elder, K., Hiemstra, C., & Brucker, L. (2019). Spatially Extensive Ground-Penetrating Radar Snow Depth Observations During NASA's 2017 SnowEx Campaign: Comparison With In Situ, Airborne, and Satellite Observations. Water Resources Research, 55(11), 10026–10036. https://doi.org/10.1029/2019WR024907

McGrath, D., Zeller, L., Bonnell, R., Reis, W., Kampf, S., Williams, K., Okal, M., Olsen-Mikitowicz, A., Bump, E., Sears, M., and Rittger, K. (2023). Declines in Peak Snow Water Equivalent and Elevated Snowmelt Rates Following the 2020 Cameron Peak Wildfire in Northern Colorado, Geophysical Research Letters, 50, e2022GL101294. https://doi.org/10.1029/2022GL101294

Meehan, T. G. (2022). Advancements in Measuring and Modeling the Mechanical and Hydrological Properties of Snow and Firn: Multi-sensor Analysis, Integration, and Algorithm Development. Boise State University Theses and Dissertations. https://doi.org/10.18122/td.1979.boisestate

Meehan, T. G., Marshall, H. P., Bradford, J. H., Hawley, R. L., Overly, T. B., Lewis, G., Graeter, K., Osterberg, E., & McCarthy, F. (2021). Reconstruction of historical surface mass balance, 1984–2017 from GreenTrACS multi-offset ground-penetrating radar. Journal of Glaciology, 67(262), 219–228. https://doi.org/10.1017/jog.2020.91

Meyer, J., Hotel, J., Kormos, P., Hedrick, A., Trujillo, E., & Skiles, S. M. (2023). Operational water forecast ability of the HRRR-iSnobal combination: an evaluation to adapt into production environments. Geoscientific Model Development, 16(1), 233-250. https://doi.org/10.5194/gmd-16-233-2023

Michaelides, R. J., Chen, R. H., Zhao, Y., Schaefer, K., Parsekian, A. D., Sullivan, T., Moghaddam, M., Zebker, H. A., Liu, L., Xu, X., & Chen, J. (2021). Permafrost Dynamics Observatory—Part I: Postprocessing and Calibration Methods of UAVSAR L-Band InSAR Data for Seasonal Subsidence Estimation. *Earth and Space Science*, *8*(7), e2020EA001630. https://doi.org/10.1029/2020EA001630

Mizukami, N., & Perica, S. (2008). Spatiotemporal Characteristics of Snowpack Density in the Mountainous Regions of the Western United States. Journal of Hydrometeorology, 9(6), 1416–1426. https://doi.org/10.1175/2008JHM981.1

Moller, D., Andreadis, K. M., Bormann, K. J., Hensley, S., & Painter, T. H. (2017). Mapping Snow Depth From Ka-Band Interferometry: Proof of Concept and Comparison With Scanning Lidar Retrievals. IEEE Geoscience and Remote Sensing Letters, 14(6), 886–890. https://doi.org/10.1109/LGRS.2017.2686398

Montesi, J., Elder, K., Schmidt, R. A., and Davis, R. E. (2004). Sublimation of Intercepted Snow within a Subalpine Forest Canopy at Two Elevations, Journal of Hydrometeorology, 5, 763–773. https://doi.org/10.1175/1525-7541(2004)005<0763:SOISWA>2.0.CO;2

Moore, C., Kampf, S., Stone, B., & Richer, E. (2015). A GIS-based method for defining snow zones: applications to the western United States. Geocarto International, 30(1), 62-82. https://doi.org/10.1080/10106049.2014.885089

Moore, C., Kampf, S., Stone, B., & Richer, E. (2012). Snow persistence grids and snow zone shape files for the western United States. *Mountain Scholar* [data set]. http://dx.doi.org/10.25675/10217/171907

Moraga, J. S., Peleg, N., Fatichi, S., Molnar, P., and Burlando, P. (2021). Revealing the impacts of climate change on mountainous catchments through high-resolution modelling, Journal of Hydrology, 603, 126806. https://doi.org/10.1016/j.jhydrol.2021.126806

Mote, P. W., Li, S., Lettenmaier, D. P., Xiao, M., & Engel, R. (2018). Dramatic declines in snowpack in the western US. Npj Climate and Atmospheric Science, 1(1), Article 1. https://doi.org/10.1038/s41612-018-0012-1

Naderpour, R., Schwank, M., Houtz, D., Werner, C., and Mätzler, C. (2022). Wideband backscattering from alpine snow cover: A full-season study. IEEE Transactions on Geoscience and Remote Sensing, 60, 1-15. https://doi.org/10.1109/TGRS.2021.3112772

Nagler, T. and Rott, H. (2000). Retrieval of wet snow by means of multitemporal SAR data, IEEE Transactions on Geoscience and Remote Sensing, 38, 754–765 https://doi.org/10.1109/36.842004

Nagler, T., Rott, H., Ripper, E., Bippus, G., and Hetzenecker, M. (2016). Advancements for Snowmelt Monitoring by Means of Sentinel-1 SAR, Remote Sensing, 8, 348. https://doi.org/10.3390/rs8040348

Nagler, T., Rott, H., Scheiblauer, S., Libert, L., Mölg, N., Horn, R., Fischer, J., Keller, M., Moreira, A., and Kubanek, J. (2022). Airborne Experiment on Insar Snow Mass Retrieval in Alpine Environment, in: IGARSS 2022 - 2022 IEEE International Geoscience and Remote Sensing Symposium, IGARSS 2022 - 2022 IEEE International Geoscience and Remote Sensing Symposium, 4549–4552. https://doi.org/10.1109/IGARSS46834.2022.9883809

NASA UAVSAR (2023). Product: fraser_05209_21021_003_210322_L090_CX01, Coregistered SLC Stack of Fraser, Colorado [data set]. NASA Jet Propulsion Laboratory.

https://uavsar.jpl.nasa.gov/cgi-bin/product.pl?jobName=fraser_05209_21021_003_210322_L090_CX_01#data

NASA UAVSAR (2023). Product: rockmt_14107_01, Coregistered SLC Stack of Rocky Mountains NP, CO, NASA Jet Propulsion Laboratory [data set]. https://uavsar.jpl.nasa.gov/cgi-bin/product.pl?jobName=rockmt_14107_01#data

NASA UAVSAR (2020). Rocky Mountains, Colorado Flight Line, Alaska Satellite Facility Distributed Active Archive Center [data set].

NASA UAVSAR (2021). Fraser, Colorado Flight Line [data set]. Alaska Satellite Facility Distributed Active Archive Center.

NASA UAVSAR (2021). Rocky Mountains, Colorado Flight Line, Alaska Satellite Facility Distributed Active Archive Center [data set].

National Academies of Sciences, Engineering, and Medicine (2018). Thriving on Our Changing Planet: A Decadal Strategy for Earth Observation from Space. National Academies Press. https://doi.org/10.17226/24938

Nolin, A. W. (2010). Recent advances in remote sensing of seasonal snow. Journal of Glaciology, 56(200), 1141–1150. https://doi.org/10.3189/002214311796406077

Ottinger, M. and Kuenzer, C. (2020). Spaceborne L-Band Synthetic Aperture Radar Data for Geoscientific Analyses in Coastal Land Applications: A Review, Remote Sensing, 12, 2228. https://doi.org/10.3390/rs12142228

Oveisgharan, S., Zinke, R., Hoppinen, Z., & Marshall, H.P. (2024). Snow Water Equivalent Retrieval Over Idaho - Part 1: Using Sentinel-1 Repeat-Pass Interferometry. The Cryosphere, 18, 559-574. https://doi.org/10.5194/tc-18-559-2024

Painter, T. (2018). ASO L4 Lidar Snow Depth 3m UTM Grid, Version 1 [Data Set]. Boulder, Colorado USA. NASA National Snow and Ice Data Center Distributed Active Archive Center. Retrieved 25 July 2020. https://doi.org/10.5067/KIE9QNVG7HP0

Painter, T. H., Berisford, D. F., Boardman, J. W., Bormann, K. J., Deems, J. S., Gehrke, F., Hedrick, A., Joyce, M., Laidlaw, R., Marks, D., Mattmann, C., McGurk, B., Ramirez, P., Richardson, M., Skiles, S. M., Seidel, F. C., & Winstral, A. (2016). The Airborne Snow Observatory: Fusion of scanning lidar, imaging spectrometer, and physically-based modeling for mapping snow water equivalent and snow albedo. Remote Sensing of Environment, 184, 139–152. https://doi.org/10.1016/j.rse.2016.06.018

Painter, T. H. & Bormann, K. J. (2020). ASO L4 Lidar Point Cloud Digital Terrain Model 3m UTM Grid, Version 1 [Data Set]. Boulder, Colorado, USA. NASA National Snow and Ice Data Center Distributed Active Archive Center. Retrieved 25 July 2020. https://doi.org/10.5067/2EHMWG4IT760

Palomaki, R. T. and Sproles, E. A. (2023) Assessment of L-band InSAR snow estimation techniques over a shallow, heterogeneous prairie snowpack, Remote Sensing of Environment, 296, 113744. https://doi.org/10.1016/j.rse.2023.113744.

Park, S.-E., Yamaguchi, Y., Singh, G., Yamaguchi, S., and Whitaker, A. C. (2014). Polarimetric SAR Response of Snow-Covered Area Observed by Multi-Temporal ALOS PALSAR Fully Polarimetric Mode, IEEE Transactions on Geoscience and Remote Sensing, 52, 329–340. https://doi.org/10.1109/TGRS.2013.2240000

Patil, A., Singh, G., and Rüdiger, C. (2020). Retrieval of Snow Depth and Snow Water Equivalent Using Dual Polarization SAR Data, Remote Sensing, 12, 1183. https://doi.org/10.3390/rs12071183

Pedersen, S. H., Bentzen, T. W., Reinking, A. K., Liston, G. E., Elder, K., Lenart, E. A., Prichard, A. K., & Welker, J. M. (2021). Quantifying effects of snow depth on caribou winter range selection and movement in Arctic Alaska. *Movement Ecology*, *9*(1), 48. https://doi.org/10.1186/s40462-021-00276-4

Pistocchi, A. (2016). Simple estimation of snow density in an Alpine region. Journal of Hydrology: Regional Studies, 6, 82–89. https://doi.org/10.1016/j.ejrh.2016.03.004

Planet Labs PBC (2021). Planet Application Program Interface: In Space for Life on Earth. *Planet*. https://api.planet.com

Raleigh, M. S., & Small, E. E. (2017). Snowpack density modeling is the primary source of uncertainty when mapping basin-wide SWE with lidar. Geophysical Research Letters, 44(8), 3700–3709. https://doi.org/10.1002/2016GL071999

Rosen, P. A., Hensley, S., Wheeler, K., Sadowy, G., Miller, T., Shaffer, S., Muellerschoen, R., Jones, C., Zebker, H., and Madsen, S. (2006). UAVSAR: a new NASA airborne SAR system for science and technology research, in: 2006 IEEE Conference on Radar, 2006 IEEE Conference on Radar, 8 pp. https://doi.org/10.1109/RADAR.2006.1631770

Ruiz, J. J., Lemmetyinen, J., Kontu, A., Tarvainen, R., Vehmas, R., Pulliainen, J., and Praks, J. (2022). Investigation of Environmental Effects on Coherence Loss in SAR Interferometry for Snow Water Equivalent Retrieval, IEEE Transactions on Geoscience and Remote Sensing, 60, 1–15. https://doi.org/10.1109/TGRS.2022.3223760

Sandmeier, K. J. (2019). ReflexW–GPR and Seismic Processing Software, Sandmeier [software]. https://www.sandmeier-geo.de/reflexw.html

Saavedra, F. A., Kampf, S. K., Fassnacht, S. R., & Sibold, J. S. (2018). Changes in Andes snow cover from MODIS data, 2000–2016. The Cryosphere, 12(3), 1027-1046. https://doi.org/10.5194/tc-12-1027-2018

Schwanghart, W. (2022a). Experimental (Semi-) Variogram (Version 1.4.0.0). MATLAB Central File Exchange. Retrieved 01 August 2022. https://www.mathworks.com/matlabcentral/fileexchange/20355-experimental-semi-variogram

Schwanghart, W. (2022b). variogramfit (Version 1.5.0.0). MATLAB Central File Exchange. Retrieved 01 August 2022. https://www.mathworks.com/matlabcentral/fileexchange/25948-variogramfit

Sexstone, G. A., & Fassnacht, S. R. (2014). What drives basin scale spatial variability of snowpack properties in northern Colorado? The Cryosphere, 8(2), 329–344. https://doi.org/10.5194/tc-8-329-2014

Shah, R., Xu, X., Yueh, S., Chae, C. S., Elder, K., Starr, B., & Kim, Y. (2017). Remote Sensing of Snow Water Equivalent Using P-Band Coherent Reflection. *IEEE Geoscience and Remote Sensing Letters*, *14*(3), 309–313. https://doi.org/10.1109/LGRS.2016.2636664

Shaw, T. E., Gascoin, S., Mendoza, P. A., Pellicciotti, F., and McPhee, J. (2020). Snow Depth Patterns in a High Mountain Andean Catchment from Satellite Optical Tristereoscopic Remote Sensing, Water Resources Research, 56, e2019WR024880 https://doi.org/10.1029/2019WR024880

Shean, D. E., Alexandrov, O., Moratto, Z. M., Smith, B. E., Joughin, I. R., Porter, C., & Morin, P. (2016). An automated, open-source pipeline for mass production of digital elevation models (DEMs) from very-high-resolution commercial stereo satellite imagery. ISPRS

Journal of Photogrammetry and Remote Sensing, 116, 101–117. https://doi.org/10.1016/j.isprsjprs.2016.03.012

Shi, J. and Dozier, J.: Estimation of Snow Water Equivalence Using SIR-C/X-SAR, Part II (2000). Inferring Snow Depth and Particle Size, IEEE Transactions on Geoscience and Remote Sensing, 38, 2475–2488. https://doi.org/10.1109/36.885196

Shi, J., Xiong, C., & Jiang, L. (2016). Review of snow water equivalent microwave remote sensing. Science China Earth Sciences, 59(4), 731–745. https://doi.org/10.1007/s11430-015-5225-0

Shook, K., & Gray, D. M. (1996). Small-Scale Spatial Structure of Shallow Snowcovers. Hydrological Processes, 10(10), 1283–1292. https://doi.org/10.1002/(SICI)1099-1085(199610)10:10<1283::AID-HYP460>3.0.CO;2-M

Siirila-Woodburn, E. R., Rhoades, A. M., Hatchett, B. J., Huning, L. S., Szinai, J., Tague, C., Nico, P. S., Feldman, D. R., Jones, A. D., Collins, W. D., & Kaatz, L. (2021). A low-to-no snow future and its impacts on water resources in the western United States. Nature Reviews Earth & Environment, 2(11), Article 11. https://doi.org/10.1038/s43017-021-00219-y

Singh, S., Durand, M., Kim, E., & Barros, A. P. (2024). Bayesian physical–statistical retrieval of snow water equivalent and snow depth from X- and Ku-band synthetic aperture radar – demonstration using airborne SnowSAr in SnowEx'17. *The Cryosphere*, *18*(2), 747–773. https://doi.org/10.5194/tc-18-747-2024

St. Clair, J., & Holbrook, W. S. (2017). Measuring snow water equivalent from common-offset GPR records through migration velocity analysis. The Cryosphere, 11(6), 2997–3009. https://doi.org/10.5194/tc-11-2997-2017

Sturm, M. (2015). White water: Fifty years of snow research in WRR and the outlook for the future. Water Resources Research, 51(7), 4948–4965. https://doi.org/10.1002/2015WR017242

Sturm, M., Goldstein, M. A., & Parr, C. (2017). Water and life from snow: A trillion dollar science question. *Water Resources Research*, *53*(5), 3534–3544. https://doi.org/10.1002/2017WR020840

Sturm, M., Holmgren, J., & Liston, G. E. (1995). A Seasonal Snow Cover Classification System for Local to Global Applications. Journal of Climate, 8(5), 1261–1283. https://doi.org/10.1175/1520-0442(1995)008<1261:ASSCCS>2.0.CO;2

Sturm, M., Taras, B., Liston, G. E., Derksen, C., Jonas, T., & Lea, J. (2010). Estimating Snow Water Equivalent Using Snow Depth Data and Climate Classes. Journal of Hydrometeorology, 11(6), 1380–1394. https://doi.org/10.1175/2010JHM1202.1

Susong, D., Marks, D., & Garen, D. (1999). Methods for developing time-series climate surfaces to drive topographically distributed energy-and water-balance models. Hydrological Processes, 13(12-13), 2003-2021.

Tarricone, J., Webb, R. W., Marshall, H. P., Nolin, A. W., & Meyer, F. J. (2023). Estimating snow accumulation and ablation with L-band interferometric synthetic aperture radar. The Cryosphere, 17(5), 1997-2019. https://doi.org/10.5194/tc-1997-2023

Techel, F., & Pielmeier, C. (2011). Point observations of liquid water content in wet snow – investigating methodical, spatial and temporal aspects. The Cryosphere, 5(2), 405–418. https://doi.org/10.5194/tc-5-405-2011

Trujillo, E. and Molotch, N. P. (2014). Snowpack regimes of the Western United States, Water Resources Research, 50, 5611–5623. https://doi.org/10.1002/2013WR014753

Tsai, Y.-L. S., Dietz, A., Oppelt, N., and Kuenzer, C. (2019). Remote Sensing of Snow Cover Using Spaceborne SAR: A Review, Remote Sensing, 11, 1456. https://doi.org/10.3390/rs11121456

Tsang, L., Durand, M., Derksen, C., Barros, A. P., Kang, D.-H., Lievens, H., Marshall, H.-P., Zhu, J., Johnson, J., King, J., Lemmetyinen, J., Sandells, M., Rutter, N., Siqueira, P., Nolin, A., Osmanoglu, B., Vuyovich, C., Kim, E., Taylor, D., Merkouriadi, I., Brucker, L., Navari, M., Dumont, M., Kelly, R., Kim, R. S., Liao, T.-H., Borah, F., & Xu, X. (2022). Review article: Global monitoring of snow water equivalent using high-frequency radar remote sensing. The Cryosphere, 16(9), 3531–3573. https://doi.org/10.5194/tc-16-3531-2022

U.S. Geological Survey (2023). USGS Water Data for the Nation [Data Set]. National Water Information System data available on the World Wide Web. Retrieved 1 June 2021. https://doi.org/10.5066/F7P55KJN

USDA Natural Resources Conservation Service (2023). SNOwpack TELemetry Network (SNOTEL) [Data Set]. NRCS. Retrieved 1 June 2021. https://data.nal.usda.gov/dataset/snowpack-telemetry-network-snotel

Viste, E., and Sorteberg, A. (2015). Snowfall in the Himalayas: an uncertain future from a little-known past, The Cryosphere, 9, 1147-1167. https://doi.org/10.5194/tc-9-1147-2015

Voegeli, C., Lehning, M., Wever, N., & Bavay, M. (2016). Scaling precipitation input to spatially distributed hydrological models by measured snow distribution. Frontiers in Earth Science, 4, 108. https://doi.org/10.3389/feart.2016.00108

Webb, R. W., Marziliano, A., McGrath, D., Bonnell, R., Meehan, T. G., Vuyovich, C., & Marshall, H. P. (2021). In situ determination of dry and wet snow permittivity: improving

equations for low frequency radar applications. Remote Sensing, 13(22), 4617. https://doi.org/10.3390/rs13224617

Webb, R., McGrath, D., Hale, K., & Molotch, N. P. (2019). SnowEx17 Ground Penetrating Radar, Version 2 [Data Set]. Boulder, Colorado USA. NASA National Snow and Ice Data Center Distributed Active Archive Center. Retrieved 25 July 2020. https://doi.org/10.5067/G21LGCNLFSC5.

Webb, R. W., Jennings, K. S., Fend, M., & Molotch, N. P. (2018). Combining Ground-Penetrating Radar With Terrestrial LiDAR Scanning to Estimate the Spatial Distribution of Liquid Water Content in Seasonal Snowpacks. Water Resources Research, 54(12), 10,339-10,349. https://doi.org/10.1029/2018WR022680

Webb, R. W., Raleigh, M. S., McGrath, D., Molotch, N. P., Elder, K., Hiemstra, C., Brucker, L., & Marshall, H. P. (2020b). Within-Stand Boundary Effects on Snow Water Equivalent Distribution in Forested Areas. Water Resources Research, 56(10), e2019WR024905. https://doi.org/10.1029/2019WR024905

Webb, R. W., Wigmore, O., Jennings, K., Fend, M., & Molotch, N. P. (2020a). Hydrologic connectivity at the hillslope scale through intra-snowpack flow paths during snowmelt. Hydrological Processes, 34(7), 1616–1629. https://doi.org/10.1002/hyp.13686

Webb, R. W., Musselman, K. N., Ciafone, S., Hale, K. E., & Molotch, N. P. (2022). Extending the vadose zone: Characterizing the role of snow for liquid water storage and transmission in streamflow generation. Hydrological Processes, 36(3), e14541. https://doi.org/10.1002/hyp.14541

Webster, R. & Oliver, M.A. (2001). Geostatistics for Environmental Scientists, John Wiley, N.Y.

Williams, K. (2021). Cameron Pass NASA SnowEx [Data Set]. Boulder, Colorado USA. UNAVCO Inc. Retrieved 1 June 2021. https://tls.unavco.org/projects/U-077/

Winkler, M., Schellander, H., & Gruber, S. (2021). Snow water equivalents exclusively from snow depths and their temporal changes: The ΔSNOW model. Hydrology and Earth System Sciences, 25(3), 1165–1187. https://doi.org/10.5194/hess-25-1165-2021

Woodhouse, I. H. (2017). Introduction to Microwave Remote Sensing, CRC Press, ISBN 036722514X.

Wrzesien, M. L., Durand, M. T., Pavelsky, T. M., Kapnick, S. B., Zhang, Y., Guo, J., & Shum, C. K. (2018). A New Estimate of North American Mountain Snow Accumulation From Regional Climate Model Simulations. Geophysical Research Letters, 45(3), 1423–1432. https://doi.org/10.1002/2017GL076664

Wrzesien, M. L., Pavelsky, T. M., Durand, M. T., Dozier, J., and Lundquist, J. D. (2019). Characterizing Biases in Mountain Snow Accumulation From Global Data Sets, Water Resources Research, 55, 9873-9891. https://doi.org/10.1029/2019WR025350.

Yildiz, S., Akyurek, Z., & Binley, A. (2021). Quantifying snow water equivalent using terrestrial ground penetrating radar and unmanned aerial vehicle photogrammetry. Hydrological Processes, 35(5), e14190. https://doi.org/10.1002/hyp.14190

Yunjun, Z., Fattahi, H., and Amelung, F. (2019). Small baseline InSAR time series analysis: Unwrapping error correction and noise reduction, Computers & Geosciences, 133, 104331. https://doi.org/10.1016/j.cageo.2019.104331

APPENDIX A: CHAPTER 2 SUPPLEMENT

Text A.1 Detailed methods: Lidar and ground-penetrating radar data processing

During surveys, lidar-measured snow depths were collected from one of three platforms (airborne, terrestrial, and uncrewed aerial vehicle). The Airborne Snow Observatory (ASO) processed snow-free and snow-on lidar elevation point clouds, producing 3 m snow depth rasters (Painter et al., 2016). U.S. Geological Survey (USGS) processed snow-free and snow-on uncrewed aerial vehicle (UAV) lidar point clouds and produced bare earth and snow depth rasters at 0.10 m spatial resolution (Bauer et al., 2023). USGS rasters were subsequently rescaled to 3 m spatial resolution. Terrestrial lidar scan (TLS) point clouds were accessed from UNAVCO, Inc. (Williams, 2021), filtered, aligned, and projected (Table 2.1) to align with the snow-free digital terrain model (DTM) collected by the USGS. For each lidar dataset, the snow surface was identified and point returns from vegetation were removed in ArcGIS Pro v3.1.2 (ESRI, 2023). The lidar datasets were converted to raster format with 3 m resolution using the average point elevation per cell. The snow-on rasters were aligned with the snow-free raster using the mean elevation difference between the snow-on and snow-free rasters from a 0.7 km section of snow-free highway (CO-14) that parallels the study area. The snow-free raster was then differenced from the snow-on scans to produce snow depth rasters. We assumed the road that bounds the meadow (Highway CO-14) had the same elevation for all scans and we estimated snow depth uncertainty as the standard deviation of the differences in elevation between the snow-on and snow-free rasters along the road. Finally, because lidar scans were performed after ground-penetrating radar (GPR) surveys, each snow depth raster received a + 0.02–0.05 m adjustment based on field notes of average snow surface compression from the GPR sled.

GPR radargrams were collected as common-offset surveys via a sled coupled to the snow surface. Grand Mesa GPR surveys used a 1.6 GHz center-frequency Mala ProEx GPR, whereas surveys at the other two sites used a 1.0 GHz center-frequency Sensors & Software PulseEkko GPR. Both GPR units operated in free run and collected traces at 5–10 Hz. Radargram processing followed a general workflow: (1) geolocate traces (spatial accuracy = ± 0.25 m), (2) time-zero correction, (3) remove DC-shift (dewow), (4) equidistant trace interpolation to 0.10 m, (5) 2-dimensional filtering to remove instrument noise, and (6) picking the ground reflection two-way travel time. Additional processing notes are provided in the User Documentation for each published GPR dataset (Webb et al., 2019; McGrath et al., 2021; Bonnell et al., 2022).

Text A.2 Detailed methods: Identifying dry and wet snow conditions

Surveys were identified as dry snow based on notes and temperatures taken in snow pits (Figure C2). A number of snow pit surveys at Grand Mesa (Elder et al., 2018) noted the presence of LWC using the hand squeeze test (Techel & Pielmeier, 2011), but the snow temperature measurements seemingly contradict these observations. Although near-surface (< 30 cm depth) snow layers had a median temperature of – 1°C on 10 February, the deeper layers had a median temperature of – 2°C and, given the accuracy of the thermometers (± 0.5°C), indicates that any LWC that was present was minor and likely limited to the uppermost layer/s. Thus, its volumetric content was not substantial enough to warrant the 8 February 2017 survey being classified as wet snow. We classified the 7 April 2021 survey at Ranch Creek and the 27 May 2021 survey at Cameron Pass as wet snow surveys. Snow temperatures collected in five snow pits at Ranch Creek indicated isothermal conditions with a bulk snowpack temperature of – 0.5 °C and surface melt was noted during GPR collection. Snow temperatures were not collected for the 27 May

2021 Cameron Pass survey, but we classified it as a wet snow survey based on the presence of standing water up to 0.12 m in the snow pit.

Text A.3 Detailed methods: Snow density model parameters

Empirical models range from simpler equations (e.g., Mizukami & Perica, 2008) that require a time parameter and a snow climate parameter, to more complicated equations (Sexstone & Fassnacht, 2014) that require snow depth, geographic (e.g., elevation or UTM coordinates), and time parameters. The required model inputs are listed in Table A2. Empirical models can be calibrated to specific study domains using nearby weather stations which measure snow water equivalent (SWE) and snow depth (McCreight & Small, 2014; Pistocchi, 2016). We chose to forego calibration for two reasons: (1) many of the regions that would benefit from SWE remote sensing are poorly instrumented and, therefore, not capable of model calibration, and (2) the main source of our calibration would be SNOTEL stations near the study areas, which are located in small forest openings, where snow density tends to be underestimated when compared to the unforested areas where most of our transects were located (Bonner et al., 2022). Empirical models were run for our surveys using inputs from the lidar snow depth rasters, but only using grid cells where relative permittivity and density values were derived.

The Snow Data Assimilation System (SNODAS) provides daily SWE and snow depth estimates, which can be divided to calculate snow density. The data are accessible at the National Snow and Ice Data Center (NSIDC; Barrett, 2004). SNODAS datasets that aligned with our survey dates were accessed and reprojected into the coordinate systems for each field site (Table 2.1). SNODAS has a much larger pixel size (~1000 m) than the derived snow density rasters (3 m), so the median of all derived densities within each SNODAS pixel was calculated to evaluate the SNODAS density estimates.

The iSnobal model (Marks et al., 1999) is incorporated as the heart of the Automated Water Supply Model (AWSM; Havens et al., 2020). AWSM handles all the data formatting, configuration, downscaling, and interpolation of input meteorological data from numerical weather prediction models via the Spatial Modeling for Resources Framework (SMRF). AWSM requires topographic and vegetation information as well as meteorological data at hourly time steps. A 50 m digital elevation model (DEM) and topographic data were generated for the Cameron Pass study area from the USGS National Elevation Dataset (https://www.usgs.gov/tools/national-map-viewer; accessed 1 April, 2023) and the 2014 USGS LandFire dataset (https://landfire.gov/, accessed on 1 April 2023). Hourly meteorological inputs (2 m air temperature and relative humidity, 10 m U- and V-components of wind, total precipitation, downward shortwave radiation flux, and total cloud cover) were derived from the High-Resolution Rapid Refresh (HRRR) atmospheric model hosted by Amazon Web Services (AWS; https://registry.opendata.aws/noaa-hrrr-pds/) and spatially distributed using the AWSM framework. Initially, iSnobal was simulated using precipitation scaling for 1 October through the final survey week of the water years, and subsequently run a second time using a lidar snow depth raster collected by Quantum Spatial Inc. over Cameron Pass on 19 March 2021 (Adebisi et al., 2022) to rescale the precipitation inputs. Precipitation was further scaled based on a comparison between the Joe Wright SNOTEL measured SWE and SMRF-distributed HRRR precipitation. The Susong et al. (1999) snow precipitation density was chosen for the model runs. Median derived densities were calculated for the 50 m iSnobal grid for comparison.

Text A.4: Detailed methods: Evaluation of modeled densities using in situ densities

We assessed the accuracy of modeled densities using a time-series of snow densities observed at the Joe Wright SNOTEL station and snow pit-measured densities from Grand Mesa

and Cameron Pass. The time-series analysis compares empirically modeled density and estimated SWE with SNOTEL density and SWE measured during WY 2020 (Figure A12). We found that the Jonas et al. (2009; J_{09}) and Sexstone & Fassnact (2014; $S\&F_{14}$) models yielded the most accurate densities and SWE at the SNOTEL station, whereas the Sturm et al. (2010; St_{10}) model consistently overestimated density and SWE and the Mizukami & Perica (2008; $M\&P_{08}$) model consistently underestimated density and SWE. SWE estimated from $M\&P_{08}$ was the least affected by short-term fluctuations in snow depth, which was problematic for the three depth-based empirical models (e.g., McCreight & Small, 2014). We then calculated RMSEs for each model using snow pit-measured densities from Grand Mesa (n = 164) and Cameron Pass (n = 12) that correspond with the lidar acquisitions (Table A6). At Grand Mesa, St_{10} yielded the most accurate densities (RMSE = 14 kg m^{-3}), whereas J_{09} yielded the most accurate densities (RMSE = 30 kg m^{-3}) at Cameron Pass. SNODAS performed comparably at both field sites (Grand Mesa RMSE = 52 kg m^{-3}; Cameron Pass RMSE = 44 kg m^{-3}). With the exception of the performance of St_{10} at Grand Mesa, these results corroborate the evaluation of modeled densities which uses the lidar-GPR derived densities as the benchmark (Figure 2.5).

Supplementary Tables

Table A1: Parameters for the Monte Carlo simulation. Mean (μ) and standard deviation (σ) are given for the input snow depth and two-way travel time (*twt)* and the output relative permittivity (ε_s) and snow density (ρ_s). Mean snow depth and *twt* were calculated for each lidar (Bauer et al., 2023; Painter, 2018; Williams, 2021) and GPR (Bonnell et al., 2022; Bonnell & McGrath, 2023; McGrath et al., 2021; Webb et al., 2019) survey date. The standard deviation of the *twt* is estimated using the mean pixel-wise *twt* standard deviation calculated for each *twt* raster. Standard deviations for Grand Mesa snow depths were estimated from previous work established by Currier et al. (2019). Standard deviations for Cameron Pass snow depths were estimated by calculating the standard deviation of the elevational offsets along the CO-14 roadway for each survey date. The standard deviation for Ranch Creek snow depth was estimated from the standard deviation of near-coincident depth probe and lidar snow depth differences.

Study Site	Date	Input d_s m (μ,σ)	Input *twt* ns (μ,σ)	Ouput ε_s (μ,σ)	Ouput ρ_s kg m^{-3} (μ,σ)
Grand Mesa	08 Feb 2017	(1.28, 0.08)	(10.69, 0.19)	(1.591, 0.212)	(305, 98)
Grand Mesa	16 Feb 2017	(1.53, 0.08)	(12.71, 0.17)	(1.568, 0.179)	(295, 84)
Grand Mesa	25 Feb 2017	(1.57, 0.08)	(12.91, 0.27)	(1.537, 0.171)	(280, 81)
Cameron Pass	18 Dec 2019	(0.66, 0.10)	(5.42, 0.21)	(1.667, 0.609)	(321, 256)
Cameron Pass	26 Feb 2020	(1.34, 0.11)	(11.05, 0.22)	(1.559, 0.272)	(288, 126)
Cameron Pass	12 Mar 2020	(1.34, 0.17)	(11.39, 0.24)	(1.716, 0.487)	(351, 208)
Cameron Pass	10 Feb 2021	(1.16, 0.22)	(9.41, 0.24)	(1.701, 0.875)	(322, 333)
Cameron Pass	24 Feb 2021	(1.10, 0.08)	(9.49, 0.26)	(1.712, 0.274)	(359, 122)
Cameron Pass	22 Mar 2021	(1.44, 0.12)	(12.16, 0.26)	(1.632, 0.292)	(322, 132)
Cameron Pass	27 May 2021	(0.67, 0.07)	(6.54, 0.26)	(2.237, 0.531)	N/A
Ranch Creek	07 Apr 2021	(0.62, 0.05)	(6.05, 0.29)	(2.164, 0.418)	N/A

Table A2: Technical details of the snow density models used in this analysis. Parameters for the first four listed models include day-of-year (DOY) or month, snow climate, snow depth (d_s), and geolocation information (i.e., elevation and Universal Transverse Mercator, or UTM, Easting). Parameters for SNODAS (Barrett, 2003) and iSnobal (Lehning et al., 2002a, 2002b) are given in their respective publications. Spatial resolution for empirical models is equivalent to the resolution of the snow depth rasters.

Model Name	Abbreviation	Model Type	Region	Parameters	Spatial Resolution
Mizukami & Perica (2008)	$M\&P_{08}$	Empirical	Western USA	DOY, Snow climate	3 m
Jonas et al. (2009)	J_{09}	Empirical	Global	Month, d_s	3 m
Sturm et al. (2010)	St_{10}	Empirical	Global	DOY, d_s, Snow climate	3 m
Sexstone & Fassnacht (2014)	$S\&F_{14}$	Empirical	Northern Colorado	DOY, d_s, Elevation, UTM Easting	3 m
SNODAS	SNO	Assimilation	USA & Canada	See Barrett (2003)	1000 m
iSnobal	iSnobal	Physical	Global	See Havens et al. (2020)	50 m

Table A3: Root mean squared error (RMSE) and mean residuals from the Kovacs et al. (1995), Kuroiwa (1954), and Webb et al. (2021) equations when compared with snow pit density measurements. *n* is the number of snow pit bulk densities used in the comparison.

		Kovacs et al. (1995)		**Kuroiwa (1954)**		**Webb et al. (2021)**	
Study Site	***n***	**RMSE (kg m^{-3})**	**Mean Residual (kg m^{-3})**	**RMSE (kg m^{-3})**	**Mean Residual (kg m^{-3})**	**RMSE (kg m^{-3})**	**Mean Residual (kg m^{-3})**
Grand Mesa	40	45	–37	101	–98	58	47
Cameron Pass	6	92	48	69	–12	177	139
Overall	46	54	–26	97	–86	83	59

Table A4: Statistical summary of lidar snow depths (d_s), GPR two-way travel times (*twt*), lidar-GPR derived relative permittivities (ε_s), and lidar-GPR derived densities (ρ_s). *n* indicates the number of observations. μ and σ represent the survey mean and standard deviation, respectively. Derived densities are not applicable (N/A) for wet snow surveys (7 April and 27 May 2021). Lidar snow depth data sources include Painter (2018; Grand Mesa), Williams (2021; Cameron Pass), and Bauer et al. (2023; Ranch Creek). GPR data sources include Webb et al. (2019; Grand Mesa), McGrath et al. (2021; Cameron Pass 2020), Bonnell et al. (2022; Cameron Pass 2021), and Bonnell & McGrath (2023; Ranch Creek).

Survey Date	**Study Site**	***n***	**d_s m (μ, σ)**	***twt* ns (μ, σ)**	**ε_s (μ, σ)**	**ρ_s kg m^{-3} (μ, σ)**
08 Feb 2017	Grand Mesa Forest	841	(1.19, 0.19)	(9.90, 1.66)	(1.570, 0.069)	(299, 33)
08 Feb 2017	Grand Mesa Open	3046	(1.30, 0.33)	(10.90, 2.75)	(1.575, 0.074)	(302, 35)
16 Feb 2017	Grand Mesa Forest	323	(1.48, 0.25)	(12.32, 2.02)	(1.548, 0.045)	(289, 21)
16 Feb 2017	Grand Mesa Open	4178	(1.53, 0.17)	(12.74, 1.39)	(1.556, 0.051)	(293, 24)
25 Feb 2017	Grand Mesa Forest	389	(1.32, 0.20)	(10.86, 1.61)	(1.510, 0.055)	(271, 26)
25 Feb 2017	Grand Mesa Open	1224	(1.65, 0.25)	(13.55, 2.03)	(1.529, 0.050)	(280, 24)
18 Dec 2019	Cameron Pass	59	(0.66, 0.10)	(5.42, 0.80)	(1.550, 0.125)	(289, 59)
26 Feb 2020	Cameron Pass	52	(1.34, 0.23)	(11.05, 1.70)	(1.539, 0.078)	(284, 37)
12 Mar 2020	Cameron Pass	212	(1.34, 0.31)	(11.39, 2.68)	(1.632, 0.056)	(328, 26)
10 Feb 2021	Cameron Pass	100	(1.16, 0.30)	(9.41, 2.53)	(1.509, 0.180)	(268, 88)
24 Feb 2021	Cameron Pass	109	(1.10, 0.38)	(9.49, 3.17)	(1.695, 0.103)	(357, 47)
22 Mar 2021	Cameron Pass	114	(1.44, 0.33)	(12.16, 2.75)	(1.608, 0.070)	(317, 33)
27 May 2021	Cameron Pass	99	(0.67, 0.26)	(6.54, 2.92)	(2.163, 0.444)	N/A
07 Apr 2021	Ranch Creek	411	(0.62, 0.13)	(6.05, 1.21)	(2.120, 0.144)	N/A

Table A5: Variogram model parameters for correlation lengths (*a*) and sills (*c*) fit with the exponential variogram function. d_s represents snow depth, *twt* is the two-way travel time of the snowpack thickness, ε_s is the relative permittivity, ρ_s represents the snow density, and SWE represents the snow water equivalent. Units of measurement are indicated within square brackets. Lidar snow depth data sources include Painter (2018; Grand Mesa), Williams (2021; Cameron Pass), and Bauer et al. (2023; Ranch Creek). GPR data sources include (Webb et al. (2019; Grand Mesa), McGrath et al. (2021; Cameron Pass 2020), Bonnell et al. (2022; Cameron Pass 2021), and Bonnell & McGrath (2023; Ranch Creek).

Survey Date	**Study Site**	**d_s (*a* [m], *c* [m^2])**	***twt*** **(*a* [m], *c* [ns^2])**	**ε_s (*a* [m], *c*)**	**ρ_s (*a* [m], *c* [kg m^{-3}]^2)**	**SWE (*a* [m], *c* [mm^2])**
08 Feb 2017	Grand Mesa Forest	(38, 0.01)	(41, 0.88)	(13, 0.004)	(13, 938)	(23, 2339)
08 Feb 2017	Grand Mesa Open	(57, 0.07)	(55, 4.89)	(21, 0.005)	(21, 994)	(46, 8844)
16 Feb 2017	Grand Mesa Forest	(27, 0.01)	(22, 1.04)	(12, 0.002)	(12, 366)	(17, 2236)
16 Feb 2017	Grand Mesa Open	(32, 0.01)	(30, 1.03)	(20, 0.002)	(20, 418)	(23, 1964)
25 Feb 2017	Grand Mesa Forest	(84, 0.02)	(64, 1.34)	(13, 0.003)	(13, 627)	(20, 2421)
25 Feb 2017	Grand Mesa Open	(25, 0.02)	(23, 1.29)	(15, 0.002)	(15, 496)	(19, 2828)
18 Dec 2019	Cameron Pass	(56, 0.01)	(51, 0.92)	(38, 0.016)	(35, 3528)	(34, 2810)
26 Feb 2020	Cameron Pass	(154, 0.14)	(147, 7.41)	(176, 0.019)	(178, 4249)	(14, 1259)
12 Mar 2020	Cameron Pass	(24, 0.12)	(23, 8.40)	(13, 0.003)	(13, 701)	(21, 12554)
10 Feb 2021	Cameron Pass	(18, 0.10)	(22, 7.30)	(24, 0.034)	(24, 8249)	(25, 19368)
24 Feb 2021	Cameron Pass	(16, 0.15)	(16, 10.38)	(18, 0.012)	(17, 2358)	(14, 14978)
22 Mar 2021	Cameron Pass	(22, 0.12)	(22, 8.31)	(10, 0.004)	(10, 947)	(19, 12505)
27 May 2021	Cameron Pass	(42, 0.09)	(52, 11.46)	(55, 0.249)	N/A	N/A
07 Apr 2021	Ranch Creek	(12, 0.02)	(12, 1.40)	(34, 0.021)	N/A	N/A

Table A6: Root mean squared error (RMSE) for modeled snow densities compared with snow pit densities at Grand Mesa and Cameron Pass. The number of snow pits available for each model is given as *n*. Models include Mizukami & Perica (2008; M&P$_{08}$), Jonas et al. (2009; J$_{09}$), Sturm et al. (2010; St$_{10}$), Sexstone & Fassnacht (2014; S&F$_{14}$), the Snow Data Assimilation System (SNODAS; Barrett, 2003), iSnobal (Lehning et al, 2002a, 2002b) with precipitation rescaling (iSn$_{re}$), and iSnobal without precipitation scaling (iSn$_{un}$). S&F$_{14}$, iSn$_{re}$, and iSn$_{un}$ were only run at Cameron Pass and are not available (N/A) at Grand Mesa. Snow pits sourced from Elder et al. (2018; Grand Mesa) and Mason et al. (2023; Cameron Pass 2020).

	Grand Mesa		Cameron Pass	
Model	**RMSE (kg m^{-3})**	***n***	**RMSE (kg m^{-3})**	***n***
M&P$_{08}$	105	164	61	12
J$_{09}$	44	164	30	12
St$_{10}$	14	164	61	12
S&F$_{14}$	N/A	N/A	40	12
SNODAS	52	164	44	12
iSn$_{re}$	N/A	N/A	50	9
iSn$_{un}$	N/A	N/A	75	9

Supplementary Figures

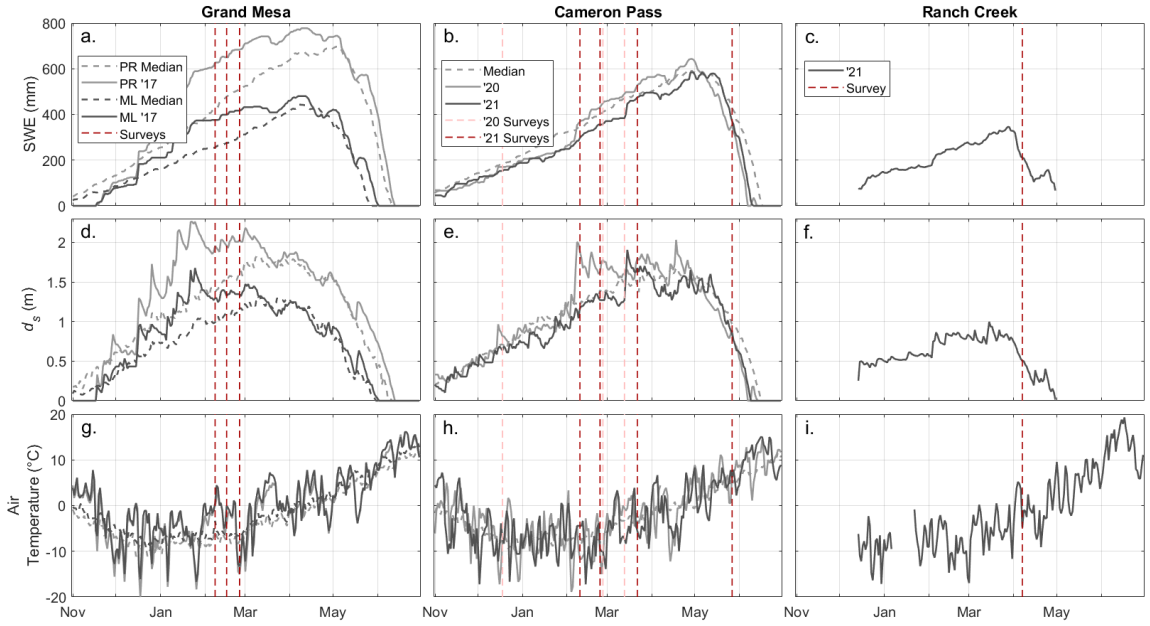

Figure A1: (a–c) Snow water equivalent (SWE), (d–f) snow depth (d_s), and (g–i) air temperature for Grand Mesa (first column), Cameron Pass (middle column), and Ranch Creek (last column). Data were obtained from the Park Reservoir (PR; Site number = 682) and Mesa Lake (ML; Site number = 622) SNOTEL stations at Grand Mesa, the Joe Wright SNOTEL station (Site number = 551) near Cameron Pass, and the U.S. Geological Survey (USGS) Ranch Creek Meadow Weather Station (Site number = 395448105453601) within the Ranch Creek field site. SWE and

air temperature medians are calculated from 1978–2022 for PR and JW and from 1985–2022 for ML. Snow depth medians are calculated from 1997–2022 for PR, 2004–2022 for JW, and 2005–2022 for ML. SNOTEL data were accessed via USDA Natural Resources Conservation Service (2023). Ranch Creek weather station data accessed via U.S. Geological Survey (2023).

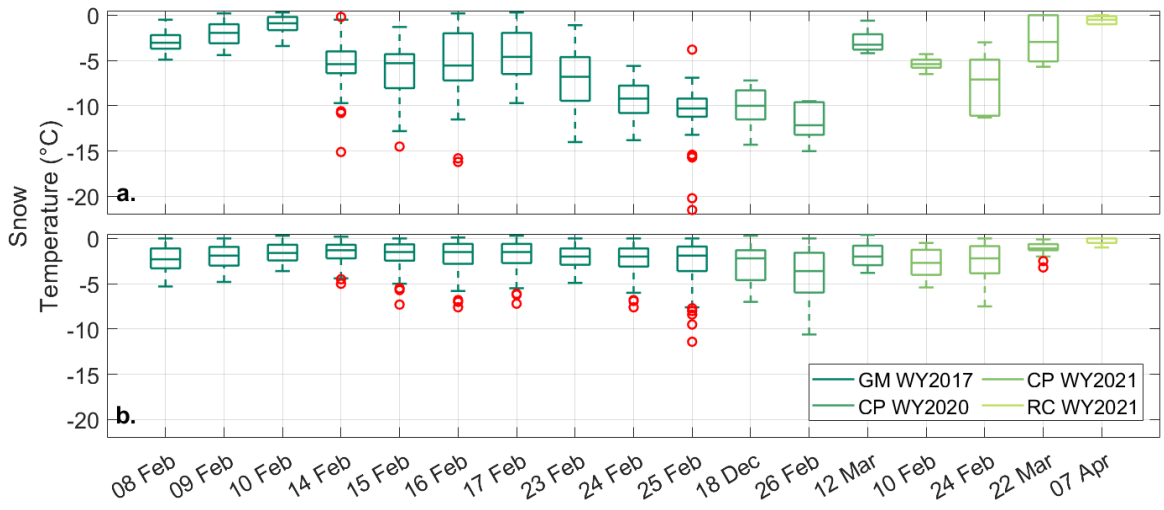

Figure A2: Layer-measured (a) surface (upper 0.30 m) and (b) subsurface (below 0.30 m from surface) snow pit temperatures on days when GPR was collected. Snow pit temperatures were not collected for 27 May 2021, however, standing water up to 0.25 m was noted in the snowpack. Snow pits were collected at Grand Mesa (GM) during Water Year (WY) 2017 (Elder et al., 2018), Cameron Pass (CP) during WY 2020 (Mason et al., 2023) and WY 2021, and at Ranch Creek (RC) during WY 2021.

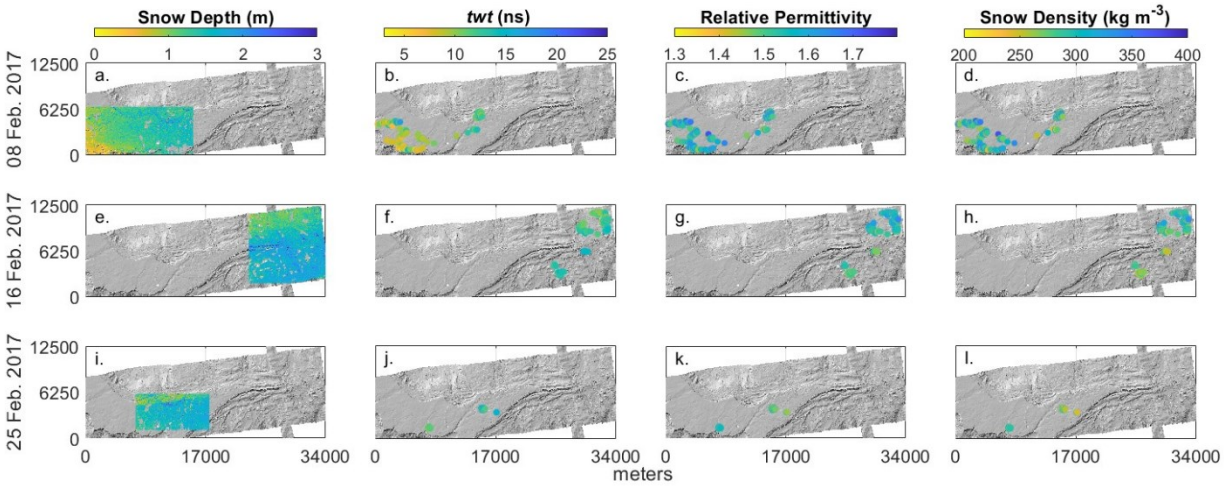

Figure A3: Grand Mesa 2017 datasets. Lidar-measured snow depth (column 1; Painter, 2018), GPR-measured two-way travel time (column 2; Webb et al., 2019), derived relative permittivity (column 3), and derived snow density (column 4). Datasets are displayed on a hill shade raster and organized by date: (a–d) 08 Feb. 2017, (e–h) 16 Feb. 2017, and (i–l) 25 Feb. 2017. Lidar snow depths are clipped to the extent of the GPR coverage to better highlight the region of interest.

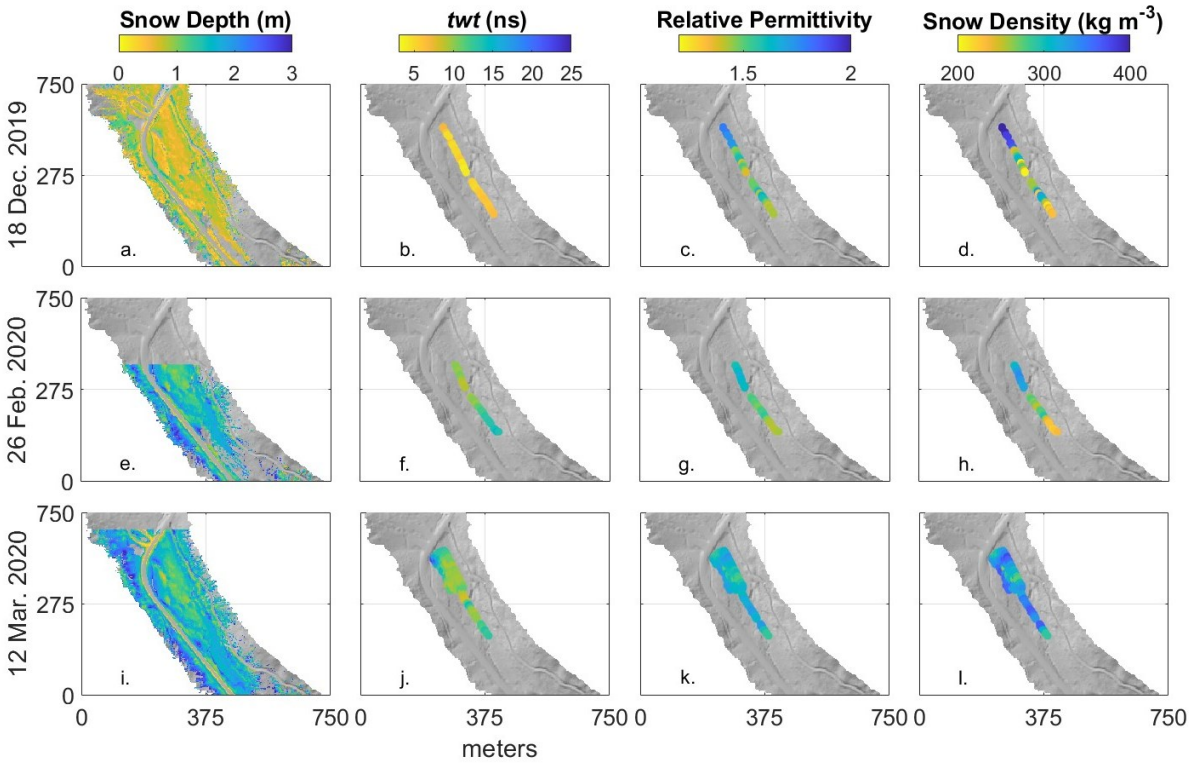

Figure A4: Cameron Pass 2020 datasets. Lidar-measured snow depth (column 1; Williams, 2021), GPR-measured two-way travel time (column 2; McGrath et al., 2021), derived relative permittivity (column 3), and derived snow density (column 4). Datasets are displayed on a hill shade raster and organized by date: (a–d) 18 Dec. 2019, (e–h) 26 Feb. 2020, and (i–l) 12 Mar. 2020.

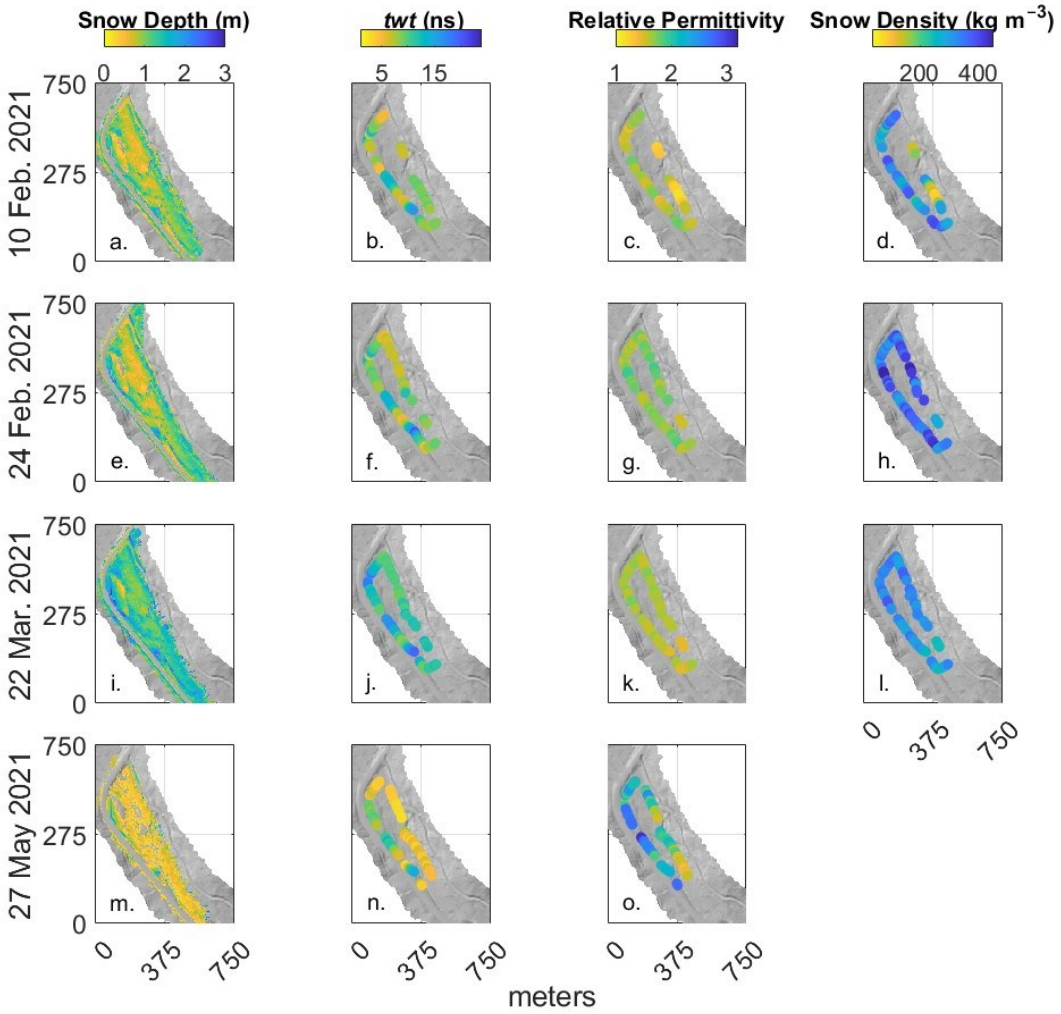

Figure A5: Cameron Pass 2021 datasets. Lidar-measured snow depth (column 1; Williams, 2021), GPR-measured two-way travel time (column 2; Bonnell et al., 2022), derived relative permittivity (column 3), and derived snow density (column 4). Datasets are displayed on a hill shade raster and organized by date: (a–d) 10 Feb. 2021, (e–h) 24 Feb. 2021, (i–l) 22 Mar. 2021, and (m–o) 27 May 2021. Density was not calculated for 27 May 2021 due to the presence of liquid water content within the snowpack.

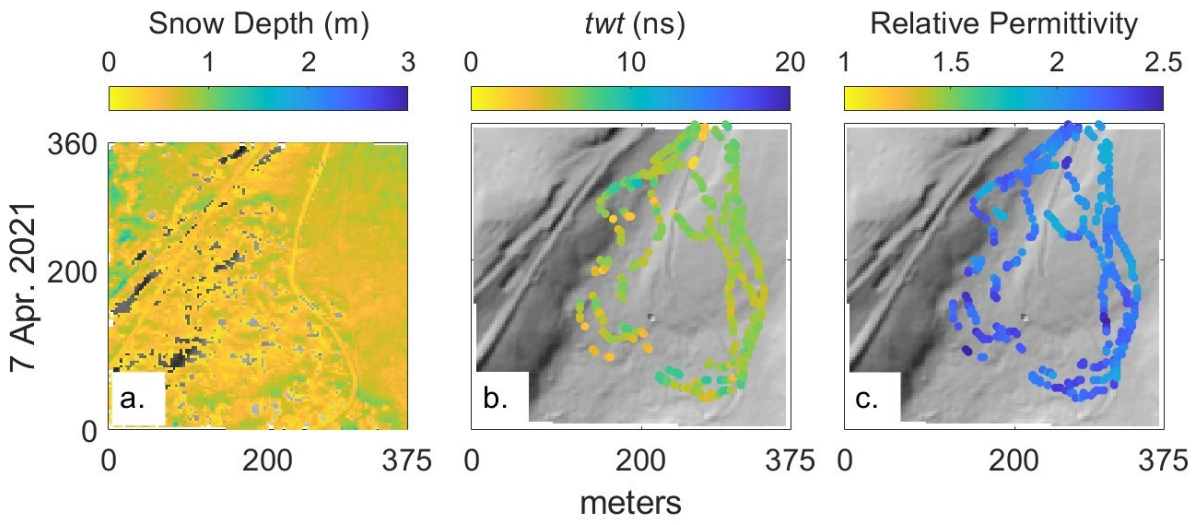

Figure A6: Ranch Creek 2021 datasets. Lidar-measured snow depth (a; Bauer et al., 2023), GPR-measured two-way travel time (b; Bonnell & McGrath, 2023), and derived relative permittivity (c). Density was not derived for this dataset due to the presence of liquid water content in the snowpack. Datasets are displayed on a hill shade raster.

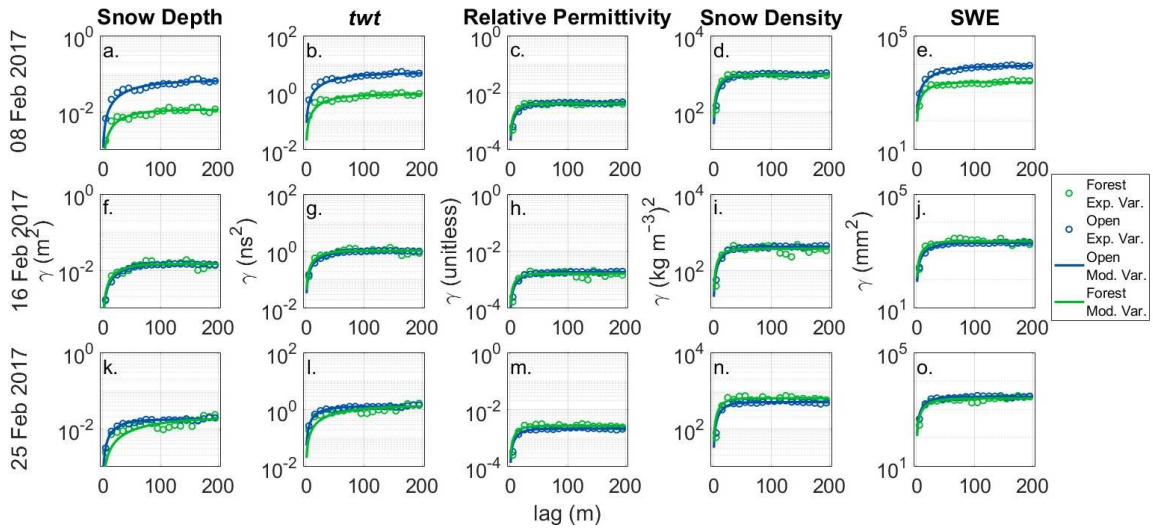

Figure A7: Experimental variograms (Exp. Var.) and best fit exponential variogram models (Mod. Var.) plotted for Grand Mesa on 8 Feb 2017 (a–e), 16 Feb 2017 (f–j), and 25 Feb 2017 (k–o). Columns are organized from left to right by variable: snow depth, *twt*, relative permittivity, snow density, and SWE. Observations were classified as under forest or in the open based on a 2 m threshold from lidar-derived vegetation heights (Painter & Bormann, 2020).

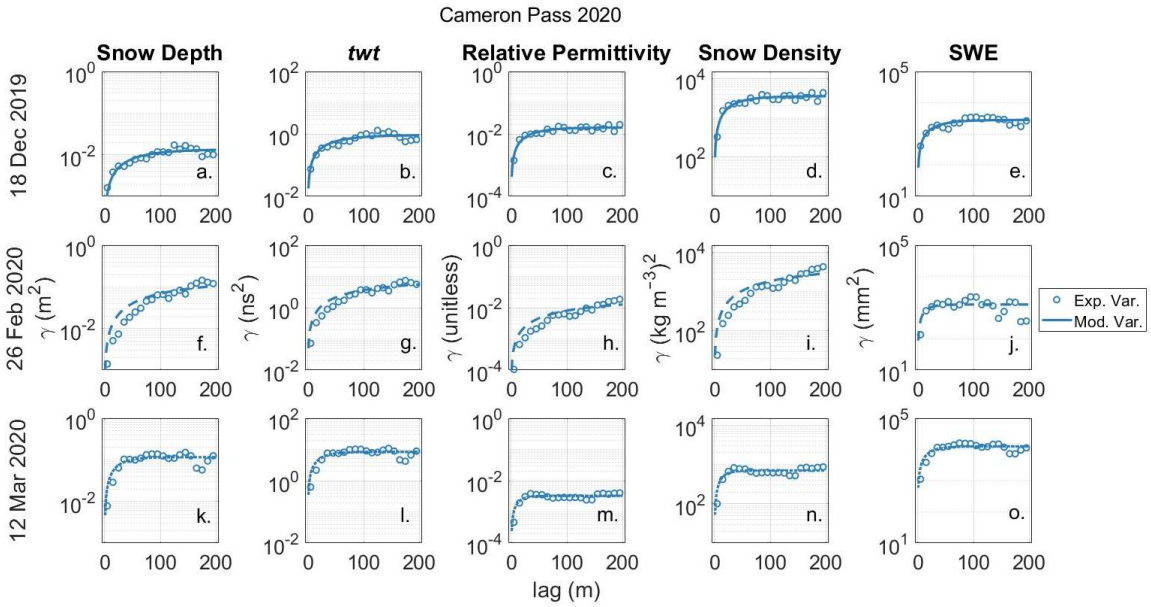

Figure A8: Experimental variograms (Exp. Var.) and best fit exponential variogram models (Mod. Var.) plotted for Cameron Pass on 18 Dec 2019 (a–e), 26 Feb 2020 (f–j), and 12 Mar 2020 (k–o). Columns are organized from left to right by variable: snow depth, *twt*, relative permittivity, snow density, and SWE.

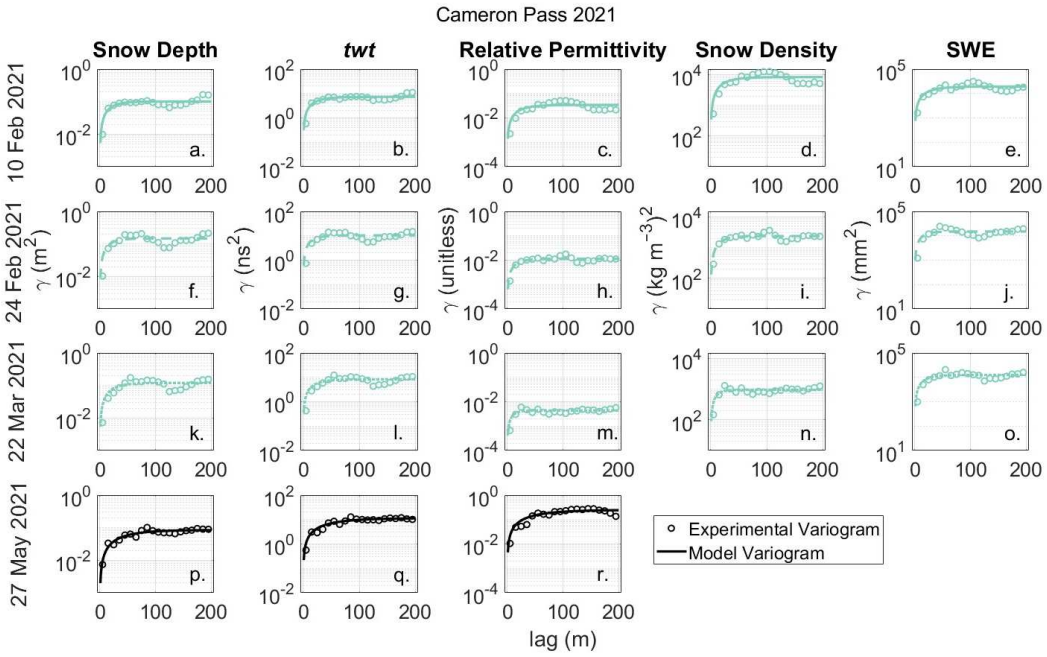

Figure A9: Experimental variograms and best fit exponential variogram models plotted for Cameron Pass on 10 Feb 2021 (a–e), 24 Feb 2021 (f–j), 22 Mar 2021 (k–o), and 27 May 2021 (p–r). Columns are organized from left to right by variable: snow depth, *twt*, relative permittivity,

snow density, and SWE. Due to the presence of liquid water content in the snowpack on 27 May 2021, density and SWE were not calculated.

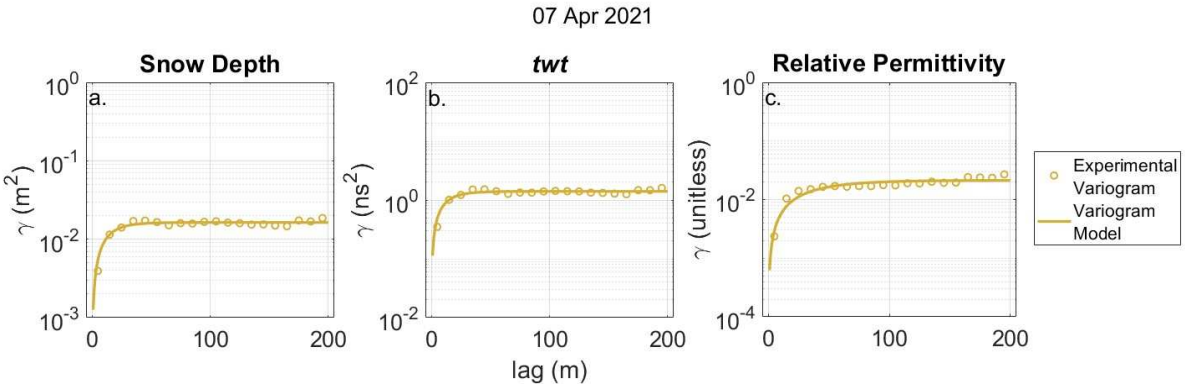

Figure A10: Experimental variograms and best fit exponential variogram models of snow depth (a), *twt* (b), and relative permittivity (c) plotted for the 07 April 2021 Ranch Creek survey. Because of the presence of liquid water content during this survey, snow density and SWE were not calculated.

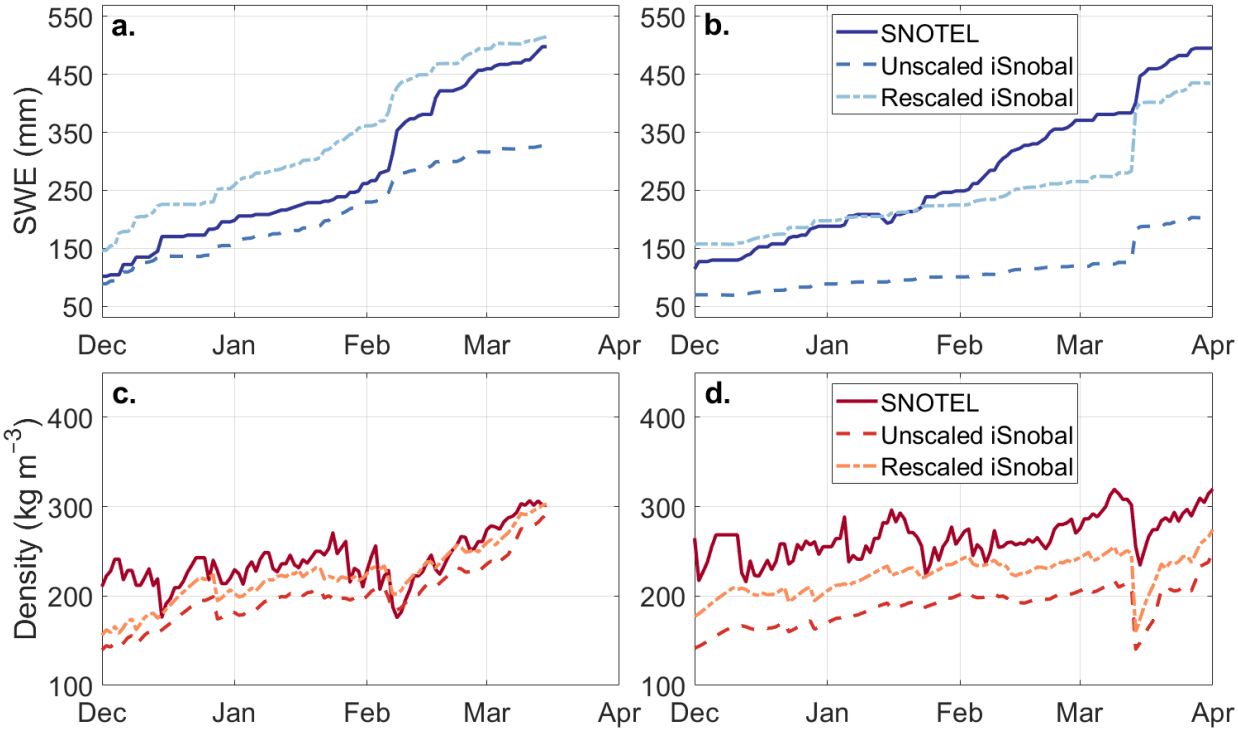

Figure A11: Joe Wright SNOTEL station (Site number = 551; USDA Natural Resource Conservation Service, 2023) measurements compared with iSnobal model results for SWE for WY 2020 (a) and WY 2021 (b) and for density for WY 2020 (c) and WY 2021 (d). iSnobal model results include a simulation where HRRR precipitation from the High Resolution Rapid Refresh (HRRR; rapidrefresh.noaa.gov/hrrr/) is input as provided (unscaled) and a simulation

where HRRR precipitation is rescaled using a snow depth lidar scan from 19 March 2021 (Adebisi et al., 2022) and a precipitation scalar of 1.5 for WY 2020 and 2.0 for WY 2021.

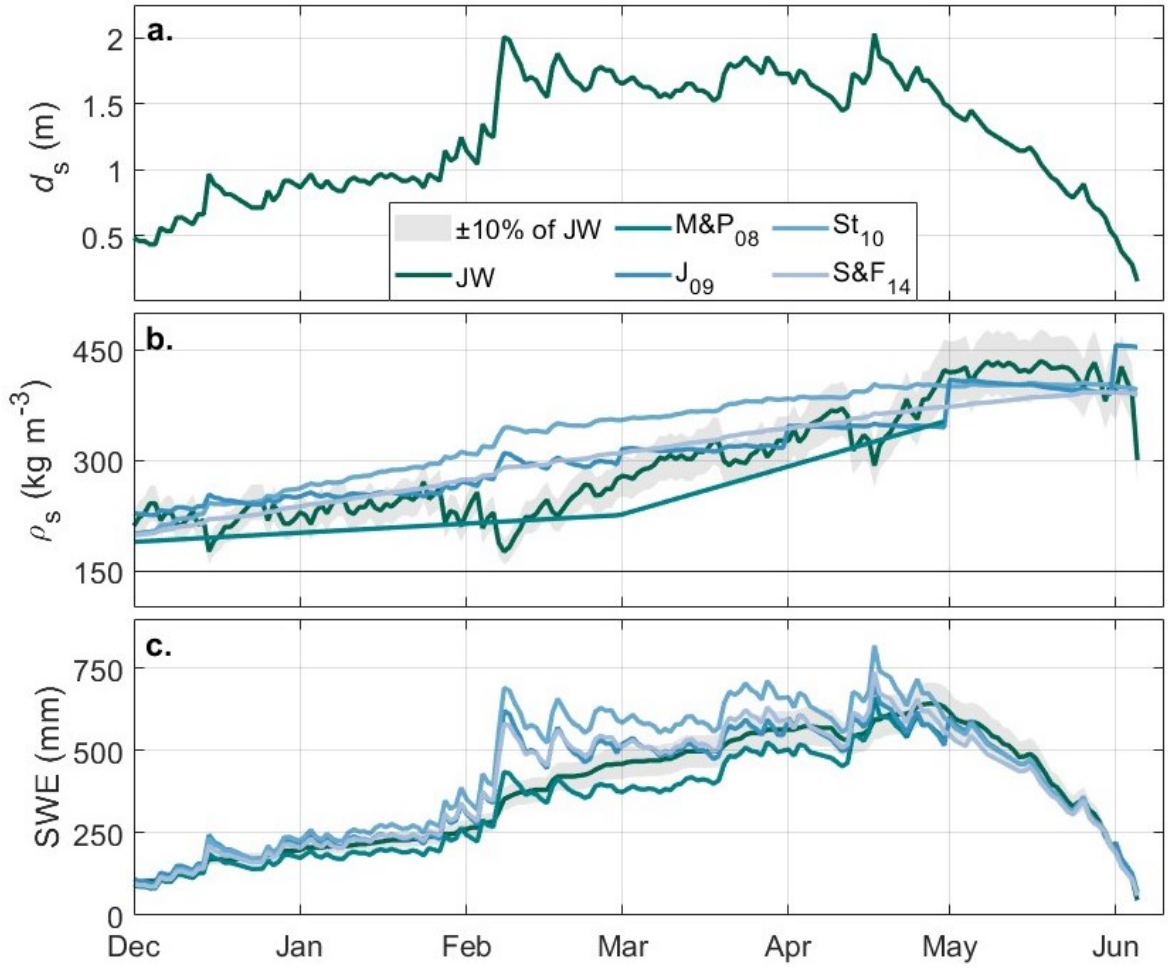

Figure A12: Comparison between the Joe Wright (JW) SNOTEL (Site number = 551; USDA Natural Resource Conservation Service, 2023) measured snow depth (a), snow density (b), and SWE (c) with empirical models for the 2020 water year. A margin of ±10% of the SNOTEL measurements is given in b–c to better understand the accuracy of the empirical models.

APPENDIX B: CHAPTER 3 SUPPLEMENT

Text B.1 Radar for SWE retrievals: L-band transmissibility

At L-band frequencies (1–2 GHz, ~0.25 m wavelength), dry snow is fully transmissible because of limited interactions between snow grains and the radar signal (Tsai et al., 2019). The bulk of reflected energy is returned from the snow-ground interface for areas without dense vegetation (Nagler et al., 2022), but uncertainty regarding the source of the primary backscattering surface increases with increased vegetation density because the L-band signal interacts with tree trunks, large branches, and dense vegetation (Ottinger and Kuenzer, 2020).

Text B.2 Radar for SWE retrievals: The InSAR technique for ΔSWE retrievals

Text B.2.1 Introduction to the InSAR technique

SARs emit polarized radar signals at a given frequency and narrow bandwidth and record the amplitude and phase of backscattered signal (Woodhouse, 2017). InSAR is a change-detection technique that calculates the phase change between two radar signals operating at identical wavelengths and polarizations. Guneriussen et al. (2001) proposed a method for removing the snow accumulation signal from interferometric pairs where at least one of the acquisitions occurred during the snow season. Their proposed method forms the basis for most published InSAR ΔSWE retrieval techniques and is the one we implement. We applied this technique to repeat airborne acquisitions and assume the phase deformation is primarily due to the accumulation or redistribution of snow. We accessed unwrapped interferograms from the ASF Distributed Active Archive Center (DAAC). Interferograms were unwrapped by the UAVSAR team, following the Integrated and Correlation Unwrapping method (Goldstein and Werner, 1998). This technique relies on the interferometric coherence (γ), which is calculated as

$$\gamma = \frac{E[u_1\, u_2^*]}{\sqrt{E[|u_1|^2]}\sqrt{E[|u_2|^2]}} \quad \text{Equation B1,}$$

where E is the expected value of a given variable and u_1 and u_2 are the amplitudes for the two image pairs (Woodhouse, 2017).

In the case of snow, the amplitude center is assumed to be the snow-ground interface and any deformation in phase is expressed as

$$\varphi = \varphi_{flat} + \varphi_{topo} + \varphi_{atm} + \varphi_s + \varphi_{err} \quad \text{Equation B2,}$$

where the total interferometric phase change (φ) is expressed as the sum of the phase changes that arise from changes in the relative distance between the radar platform and the ground target for flat Earth (φ_{flat}) and topography (φ_{topo}), changes in the atmospheric conditions that cause signal delays (φ_{atm}), the changes in phase caused by the change in snow depth or SWE (φ_s), and phase changes caused by instrument noise (φ_{err}; Deeb et al., 2011). Instrument noise can manifest as random error or systematic error, which can result from a non-constant flight track (Jones et al., 2016). Topographic corrections are minimized by the UAVSAR instrument, as it performs acquisitions within a repeated 10 m tube, but both the topographic and flat Earth contributions towards total phase change are accounted for in the UAVSAR unwrapped interferograms. However, atmospheric delays, caused by changes in atmospheric pressure and water vapor mass that occur between acquisitions, may influence the interferometric phase change (Bevis et al., 1992).

Text B.2.2 Radar for SWE retrievals: Atmospheric correction for UAVSAR

Atmospheric delays are generally described as stratified or turbulent, where stratified delays are manifested as phase ramps or are correlated with topography and occur due to relatively homogeneous differences in atmospheric conditions, whereas turbulent delays are more difficult to identify and are caused by heterogeneous differences in atmospheric conditions

(Hu and Mallorquí, 2019). Modeling atmospheric delays from airborne platforms is complicated, primarily due to the relatively coarse vertical resolution of most atmospheric reanalysis/forecast products that extends higher than the UAVSAR flight altitude (~12.5 km). Three recently developed methods may be applicable for our study: (1) a statistical approach that models delays assuming a stratified atmosphere (Tarricone et al., 2023), (2) an approach that integrates phase delays along the signal path using ERA5 atmospheric data (Hoppinen et al., 2024), and (3) modeling the turbulent delay from atmospheric pressure and precipitable water using the High Resolution Rapid Refresh Model (HRRR; Gong et al., 2013). We chose the Tarricone et al. (2023) approach, which has higher spatial resolution than either the ERA5 or HRRR methods, and developed a workflow to evaluate the need for a stratified atmospheric correction.

The workflow estimates an atmospheric correction as a best-fit plane across the UAVSAR scene, by regressing the unwrapped phase at snow-free pixels with the radar signal path length. Before the analysis, we defined requirements that the atmospheric correction had to meet in order to be implemented: (1) regression slope estimators needed to be identical across all four polarizations and the estimator's p-value needed to be <0.05, (2) coefficients of determination (r^2) were required to be >0.20, and (3) the root mean squared error (RMSE) of atmospherically corrected ΔSWE had to improve the RMSE of uncorrected ΔSWE by >20%.

Sentinel-2 Level 2A (Surface Reflectance) 2020 and 2021 products were accessed in Google Earth Engine at 10 m resolution. Clouds were removed for each image and an average image was composited for all Sentinel-2 acquisitions between UAVSAR flights. Normalized difference snow index (NDSI; Dozier, 1989) between green and shortwave infrared (SWIR) bands was calculated as

$$NDSI = \frac{Band_{green} - Band_{SWIR}}{Band_{green} + Band_{SWIR}} \quad \text{Equation B3.}$$

We then masked out forests from the scene using the Copernicus Global Land Cover 100 m dataset (Figure S1). Snow-free pixels were identified as NDSI < 0.2, based on visual inspection of the optical imagery. We then regressed the unwrapped phase at snow-free pixels against the radar signal path length to estimate a phase ramp for each InSAR pair. We calculated RMSE for both atmospherically corrected and uncorrected datasets using SNOTEL ΔSWE calculated from the four SNOTEL stations (Table S2) where we took the median of the nearest nine UAVSAR ΔSWE pixels but removed stations that had coherence <0.5. No single interferogram met our listed requirements (Table S1). We conclude that stratified atmospheric delays may be present, but do not substantially affect the accuracy of ΔSWE retrievals.

B.2.3 Radar for SWE retrievals: Calculating InSAR ΔSWE retrievals

Assuming all other phase terms are accounted for (Equation B2), ΔSWE can be calculated from the snow phase term, the radar wavelength (λ; ~0.238 m), the local incidence angle (θ_{inc}), and the relative permittivity (ε_s). Because the radar signal intersects the snowpack obliquely, the unwrapped phase must be projected to the surface normal using the local incidence angle. We calculated incidence angles in uavsar_pytools (Hoppinen et al., 2022) as

$$\theta_{inc} = (-\hat{n} \cdot \|lkv\|) \quad \text{Equation B4,}$$

where $\hat{n} \cdot \|lkv\|$ is the dot product of the surface normal calculated from a DEM and the magnitude of the UAVSAR-provided look vector (containing the east, north, and up components).

Relative permittivity describes the ratio of the dielectric permittivity of a material to the dielectric permittivity of free space (Daniels, 2004). In dry snow, relative permittivity is determined primarily by the snow density, whereas liquid water content becomes the defining variable in wet snow (Bonnell et al., 2021; Koch et al., 2014). We concluded that the snowpack

was dry throughout our field campaigns (Section 3.4.1). We calculated relative permittivity from the Kovacs et al. (1995) equation, which was found to have a RMSE = 54 kg m^{-3} for densities derived in Colorado (Bonnell et al., 2023). The equation,

$$\varepsilon_s = \left(1 + 0.845 \frac{\rho_s}{1000}\right)^2 \quad \text{Equation B5,}$$

calculates the relative permittivity of snow from the snow density (ρ_s) in kg m^{-3} and represents the median of published dry snow relative permittivity equations (Di Paolo et al., 2020). We estimated the relative permittivity of the snowpack surface using an estimate of the snowpack surface density. The change in snow depth (Δd_s) is given as

$$\Delta d_s = -\frac{\lambda \varphi_s}{4\pi} \times \frac{1}{cos\,\theta_{inc} - \sqrt{\varepsilon_s - sin^2\theta_{inc}}} \quad \text{Equation B6.}$$

At the UAVSAR wavelength and for a given θ_{inc} = 1.2 radians and a snow surface ε_s = 1.270 (ρ_s = 150 kg m^{-3}), phase wrapping occurs at Δd_s = 0.72 m, or ΔSWE = 108 mm. Finally, ΔSWE is calculated by multiplying the snow depth by the surface density:

$$SWE = d_s \times \rho_s \quad \text{Equation B7.}$$

B.2.4 Radar for SWE retrievals: Evaluation of the Leinss et al. (2015) linear approximation for InSAR ΔSWE retrievals

For dry snow, InSAR phase change has a near-linear dependence upon the change in SWE (Guneriussen et al., 2001; Leinss et al., 2015; Oveisgharan et al., 2024), and such a relation can be leveraged to derive InSAR ΔSWE independent of density or relative permittivity measurements. In our study, we calculated ΔSWE using the density-dependent method (Equation B6–B7) because surface density was a target variable during the surveys (Figure 3.3) and several previous studies have opted to use the density-dependent method because airborne platforms yield a much larger range of incidence angles than satellite platforms (e.g., Hoppinen et al., 2024; Marshall et al., 2021; Nagler et al., 2022; Tarricone et al., 2023). We evaluated the utility

of the Leinss et al. (2015) approximation for ΔSWE using the 16–22 March 2021 HH InSAR pair. The equation,

$$\Delta SWE = \frac{\varphi_s \lambda}{2\pi\alpha}\left(1.59 + \theta_{inc}^{\frac{5}{2}}\right)^{-1} \qquad \text{Equation B8,}$$

modifies Equation B6 using the Matzler (1996) permittivity model such that ΔSWE is calculated from the phase change, the radar wavelength, the incidence angle, and an optimization parameter (α). Readers are referred to Leinss et al. (2015) for a review of the optimization parameter. Given the range of incidence angles and snow densities at our field sites, we chose α = 1.02. The linear approximation results in nearly identical ΔSWE retrievals (r=0.99; Figure B4a–c) and the comparison with GPR ΔSWE retrievals yields nearly identical statistical distributions and performance statistics (Figure B4d–f). We conclude that the Leinss et al. (2015) approximation may be an appropriate alternative for ΔSWE retrievals from airborne platforms.

B.2.5 Radar for SWE retrievals: Incidence angle analysis

The incidence angles used to calculate ΔSWE from the UAVSAR unwrapped phase datasets were derived by down-sampling from the Copernicus 30 m DEM. The Copernicus 30 m DEM was derived from TanDEM-X acquisitions, which operates at 9.6 GHz center frequency and the DEM has increased uncertainty over forested landscapes. Here, we evaluated the uncertainty for ΔSWE retrievals caused by errors in the Copernicus-derived incidence angles by calculating incidence angles from a 0.5 m lidar digital terrain model collected in September 2021 (Adebisi et al., 2022) over a subset of the UAVSAR swath that includes our field sites. Although the Copernicus-derived incidence angles display similar trends compared to the lidar-derived incidence angles, a comparison between the two products reveals high variability between the two products (r = 0.08, RMSE = 20°; Figure B5a–c). ΔSWE retrieval uncertainty was estimated through a Monte Carlo simulation with 100 000 realizations around a mean incidence angle of

52.8° and a 20° standard deviation, approximated from the RMSE of the Copernicus-derived incidence angles (Figure B5d). A density of 150 kg m–3 and phase change of 0.5π were used for the ΔSWE inversion (Figure B5e). From the standard deviation of simulated ΔSWE, we estimate a ΔSWE retrieval uncertainty of ±7 mm that can be attributed to the use of the Copernicus-derived incidence angles.

B.3 Radar for SWE retrievals: GPR for SWE retrievals

GPR is a geophysical method for subsurface imaging that, when set up in the common-offset configuration, can measure the *twt* from the antennas to a reflector of interest. We used a L-band GPR with a 1.0 GHz center-frequency and a 1.0 GHz bandwidth. GPR is a well-evaluated tool for estimating spatially distributed snow depth and SWE (Koh et al., 1996; Lundberg et al., 2006; McGrath et al., 2019). GPR surveys aggregate signal traces to form radargrams, which map reflection amplitudes with corresponding *twt*. For SWE retrievals, the reflector of interest is the snow-ground interface, which manifests as the highest magnitude reflector at depth, due to the high contrast between snow and soil permittivity. The radar velocity (v_s) of the snowpack can be estimated from the snowpack relative permittivity (Equation B5),

$$v_s = \frac{c}{\sqrt{\varepsilon_s}} \qquad \text{Equation B9,}$$

where c is the velocity of electromagnetic waves in free space (Daniels, 2004). Then, the *twt* of the ground reflector can be converted to snow depth,

$$d_s = v_s \frac{twt}{2} \qquad \text{Equation B10,}$$

which is subsequently converted to SWE (Equation B7).

Supplementary Tables

Table B1: Results from the test for atmospheric delays. Unwrapped phase (φ) was regressed against signal path length for snow-free pixels. The slope estimate (ß) and coefficient of determination (r^2) are reported for each date and polarization. RMSE was calculated with and

without the estimated atmospheric corrections for four SNOTEL stations distributed throughout the UAVSAR flight line. Improvements in RMSE due to the atmospheric correction are reported as positive percents, while RMSE degradations are reported as a negative percent.

	HH			HV			VH			VV		
InSAR Pair	**β (φ/m)**	**r^2**	**RMSE Change (%)**	**β (φ/m)**	**r^2**	**RMSE Change (%)**	**β (φ/m)**	**r^2**	**RMSE Change (%)**	**β (φ/m)**	**r^2**	**RMSE Change (%)**
12–19 February 2020	6.35e–5	0.14	-6.82	7.85e–5	0.22	-40.74	8.21e–5	0.21	-11.43	7.76e–5	0.29	No Data
19–26 February 2020	–3.23e–5	0.06	0.00	–3.08e–5	0.05	0.00	–2.58e–5	0.03	0.00	–2.97e–5	0.06	0.00
26 February – 12 March 2020	–9.24e–5	0.15	13.70	–1.82e–5	0.25	No Data	–1.34e–4	0.20	No Data	–3.17e–5	0.04	No Data
15–20 January 2021	–3.60e–5	0.08	-2.99	–4.76e–5	0.13	-9.80	–5.38e–5	0.16	-12.24	–3.99e–5	0.11	-2.44
20–27 January 2021	2.97e–5	0.04	12.50	4.45e–5	0.09	3.70	4.34e–5	0.07	15.79	2.65e–5	0.04	16.67
27 January – 3 February 2021	–1.20e–4	0.10	0.00	–1.16e–4	0.09	-3.23	–1.15e–4	0.08	-25.93	–1.01e–4	0.06	40.00
3–23 February 2021	–2.41e–4	0.58	No Data	No Data	No Data	No Data	–2.57e–4	0.63	No Data	No Data	No Data	No Data
23 February – 3 March 2021	5.69e–5	0.12	100.00	4.05e–5	0.06	12.50	6.56e–5	0.11	32.00	3.98e–5	0.07	-200.00
3–10 March 2021	–1.85e–4	0.54	-135.29	–1.72e–4	0.50	9.52	–1.84e–4	0.52	-312.50	–1.70e–4	0.53	-75.00
16–22 March 2021	–2.12e–4	0.22	-37.50	–2.64e–4	0.25	-140.00	–2.52e–4	0.28	-16.67	–2.40e–4	0.25	-300.00

Table B2: Weather Stations within the Rocky Mountains, Colorado UAVSAR flight line. Operators include the Colorado Avalanche Information Center (CAIC), Colorado State University (CSU), and the Natural Resources Conservation Service (NRCS). Location is given as WGS84 latitude and longitude in decimal degrees (DD). Elevation is estimated from the Copernicus 30 m digital elevation model. Vegetation and Canopy Cover details obtained from the Copernicus Global Land Cover 100 m dataset (Buchhorn et al., 2020). Distance is given from the station to the Michigan River field site.

Station Name	Abbreviation	Operator	Dates in Analysis	Location (DD)	Elevation (m)	Vegetation and Canopy Cover	Distance (km)
Cameron Pass Weather Station	CAIC	CAIC	1 Jan to 31 Mar 2020, 1 Jan to 15 Mar 2021	40.497, –105.9	3081	Evergreen >70%	2.5
Cameron Peak Field Site Weather Station	CPWS	CSU	14 Jan to 31 Mar 2021	40.564, –105.867	3012	Severely Burned 0%	5.4
Joe Wright SNOTEL	JW	NRCS	1 Dec to 30 Apr 2020, 1 Dec to 30 Apr 2021	40.533, –105.887	3100	Evergreen >70%	1.6
Lake Irene SNOTEL	LI	NRCS	1 Jan to 31 Mar 2020, 1 Jan to 31 Mar 2021	40.414, –105.820	3254	Evergreen 15–70%	13.1
Montgomery Snow Stake	MSS	CSU	1 Jan to 31 Mar 2021	40.544, –105.881	3067	Evergreen >70%	2.9
Phantom Valley SNOTEL	PV	NRCS	1 Jan to 31 Mar 2020, 1 Jan to 31 Mar 2021	40.398, –105.846	2758	Herbaceous 0%	13.9
Willow Park SNOTEL	WP	NRCS	1 Jan to 31 Mar 2020, 1 Jan to 31 Mar 2021	40.434, –105.736	3263	Evergreen 15–70%	16.2

Table B3: Field site SWE change (ΔSWE) values for the interval board, GPR, and UAVSAR at co-located GPR pixels for the UAVSAR time series presented in Chapter 3 (all date intervals used HH polarization, except the VH polarization used for 3–23 February 2021). The interval board reports the mean because only two interval boards were deployed during surveys.

Date Interval	Interval Board Mean ΔSWE (mm)	GPR Median ΔSWE (mm)	UAVSAR Median ΔSWE (mm)
12–19 February 2020	43	98	97
19–26 February 2020	31	15	16
26 February – 12 March 2020	21	10	8
15–20 January 2021	22.5	13	14
20–27 January 2021	27	30	28
27 January – 3 February 2021	4	0	–2
3–23 February 2021	73	112	112
23 February – 3 March 2021	14	17	16
3–10 March 2021	4	1	4
16–22 March 2021	14	30	34

Table B4: Evaluation of the four polarizations (HH, HV, VH, and VV) of UAVSAR ΔSWE retrievals using GPR ΔSWE retrievals. For each polarization, the number of observations (n), the root mean squared error (RMSE), and Pearson's correlation coefficient (r) are given. Instances where no data was available are indicated by hyphens. Although Chapter 3 presents the HH polarization results, the overall HH statistics presented here differ from the overall statistics presented in Chapter 3 because Chapter 3 includes the 3–23 February 2021 VH pair in the presented time series.

	HH			HV			VH			VV		
InSAR Pair	**n**	**RMSE (mm)**	**r**	**n**	**RMSE (mm)**	**r**	**n**	**RMSE (mm)**	**r**	**n**	**RMSE (mm)**	**r**
12–19 February 2020	110	34	–0.03	122	32	–0.02	130	32	–0.03	-	-	-
19–26 February 2020	143	29	0.13	143	30	0.11	143	28	0.09	143	28	0.19
26 February – 12 March 2020	130	26	0.13	117	28	0.15	118	27	0.08	129	26	0.02
15–20 January 2021	390	19	0.13	401	20	0.16	379	20	0.18	400	17	0.08
20–27 January 2021	337	16	0.19	319	15	0.15	334	16	0.10	382	17	0.25
27 January – 3 February 2021	373	16	0.07	362	15	0.18	350	15	0.19	379	16	0.05
3–23 February 2021	-	-	-	-	-	-	185	33	0.01	-	-	-
23 February – 3 March 2021	396	19	0.20	402	20	0.15	398	20	0.16	390	19	0.17
3–10 March 2021	362	23	–0.24	364	21	–0.15	357	21	–0.16	376	19	–0.18
16–22 March 2021	407	22	0.07	410	20	0.09	429	20	0.13	426	21	0.05
Overall	2648	21	0.66	2640	21	0.68	2823	22	0.80	2625	19	0.48

Supplementary Figures

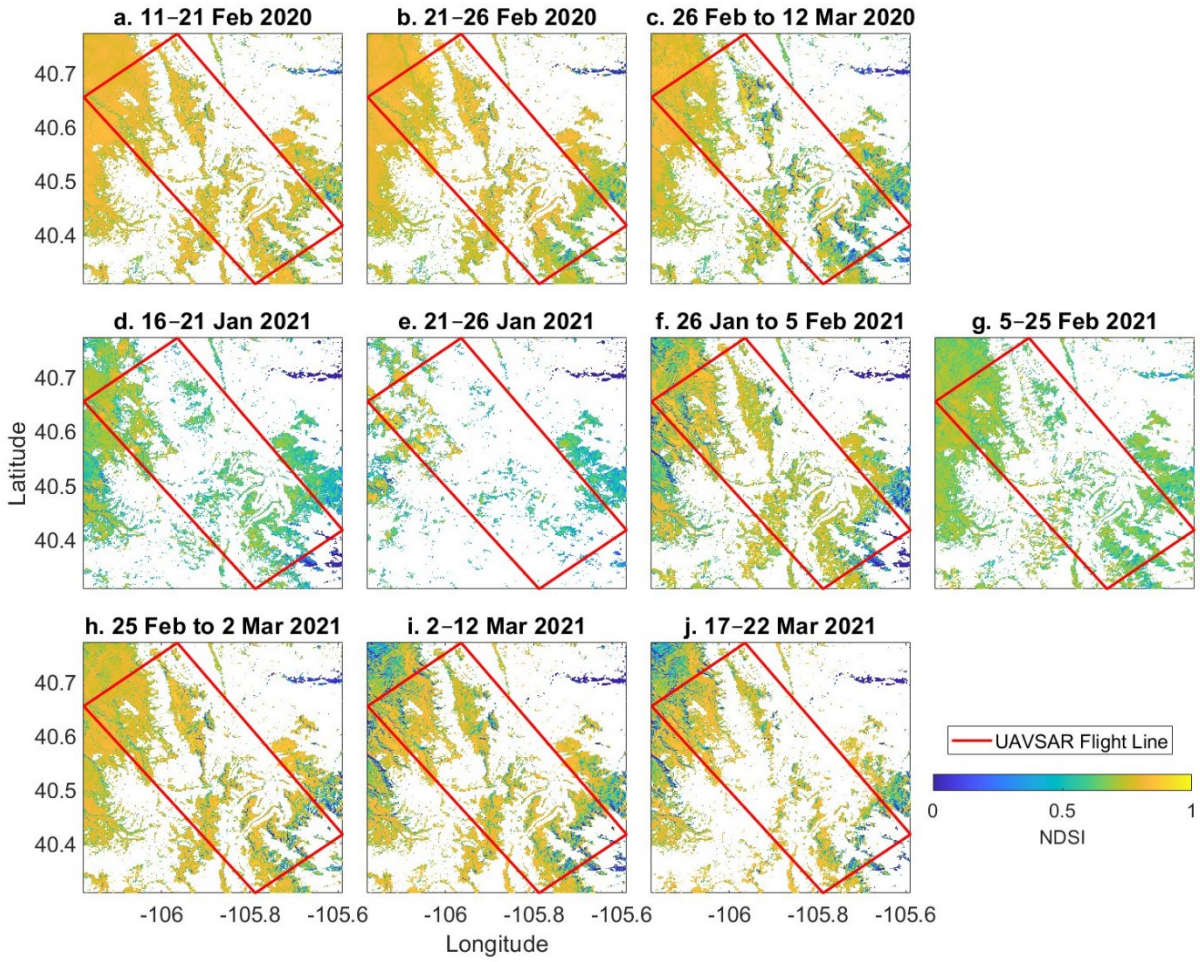

Figure B1: NDSI (Equation B3) maps for each UAVSAR flight interval calculated from composited Sentinel-2 Level 2A imagery. Clouds and forests (Buchhorn et al., 2020) were removed from this analysis. Snow-free pixels were identified as NDSI <0.20.

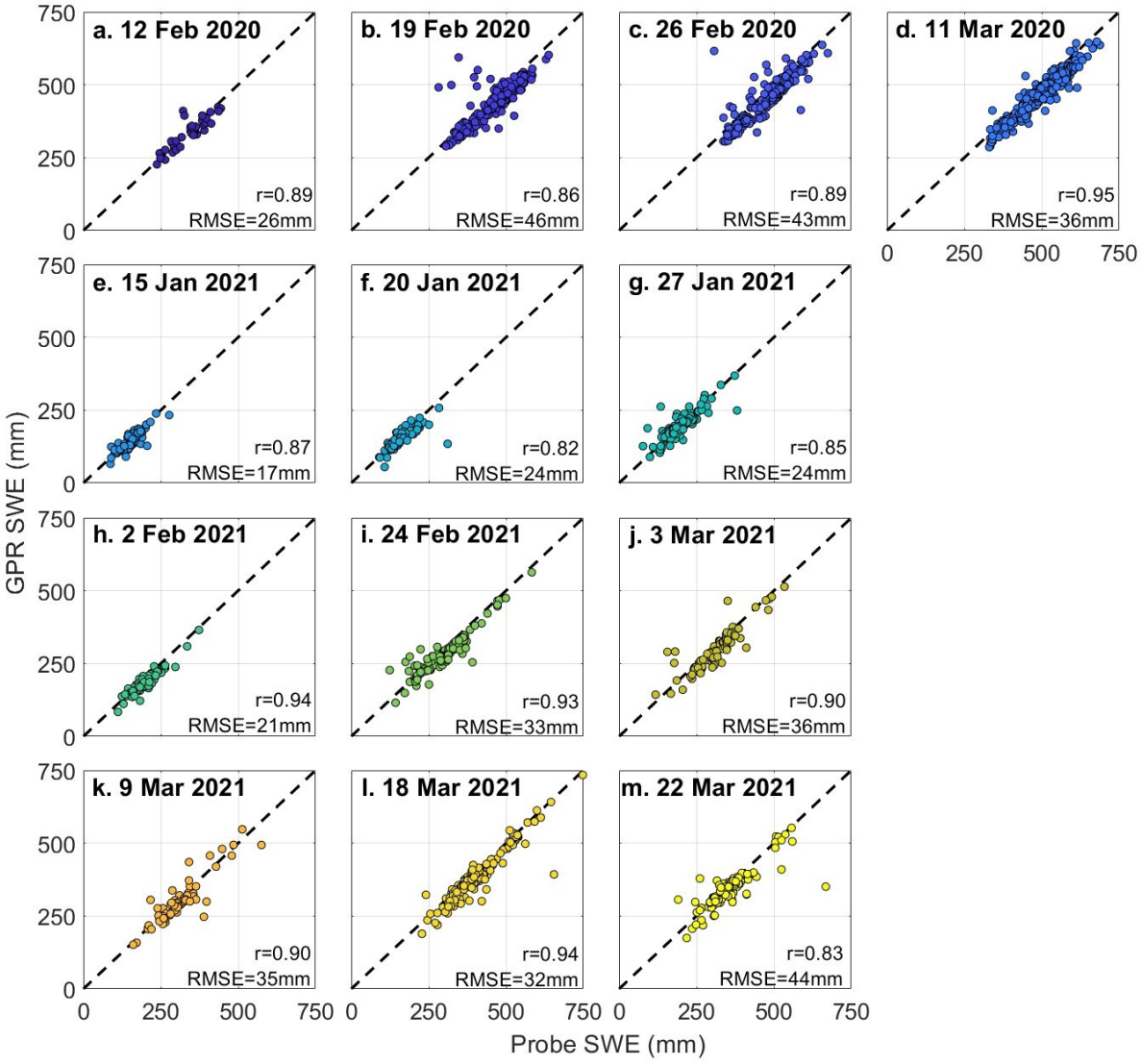

Figure B2: Comparison between GPR SWE retrievals and SWE converted from probed depths for each survey date. Median GPR SWE was calculated within a 1.5 m radius for each probed point. The number of GPR points used for estimating the median GPR SWE for comparison with probed SWE varied, but in most cases, exceeded 10 points per probe. Points are colored by date. In 2020, ~200 probed points were collected per survey date, whereas ~120 were collected per survey date in 2021. Overall Pearson's correlation coefficient = 0.97 and RMSE = 35 mm.

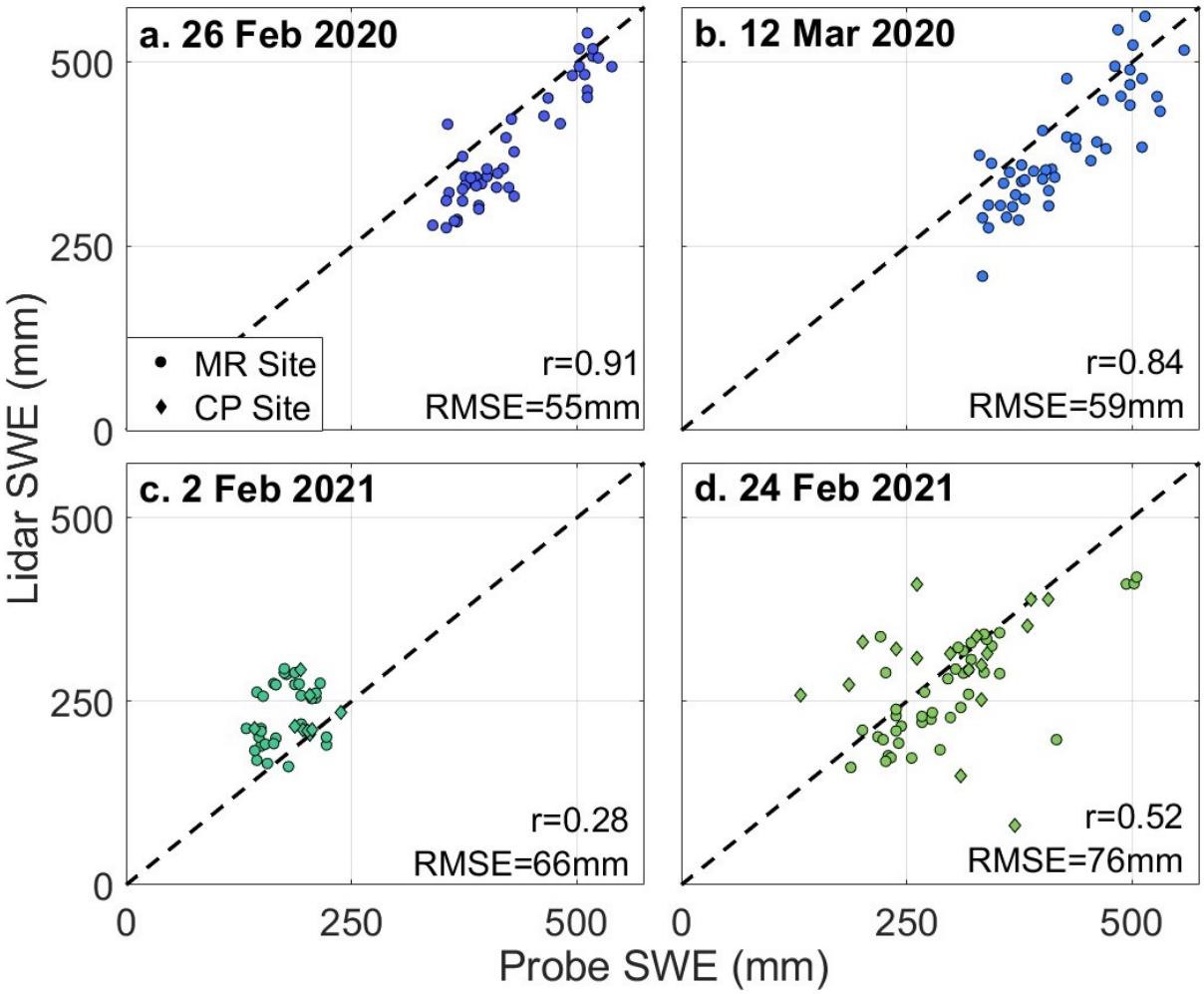

Figure B3: Comparisons between TLS SWE retrievals and SWE converted from probed depths for each lidar survey date. Probed SWE points represent the average of the one to two probed points within a single TLS pixel. The TLS survey conducted on 10 February 2021 was adjusted to 2 February 2021 by using SWE measured on the interval board on 10 February 2021. Overall Pearson's correlation coefficient = 0.83 and RMSE = 66mm. Points are colored by date.

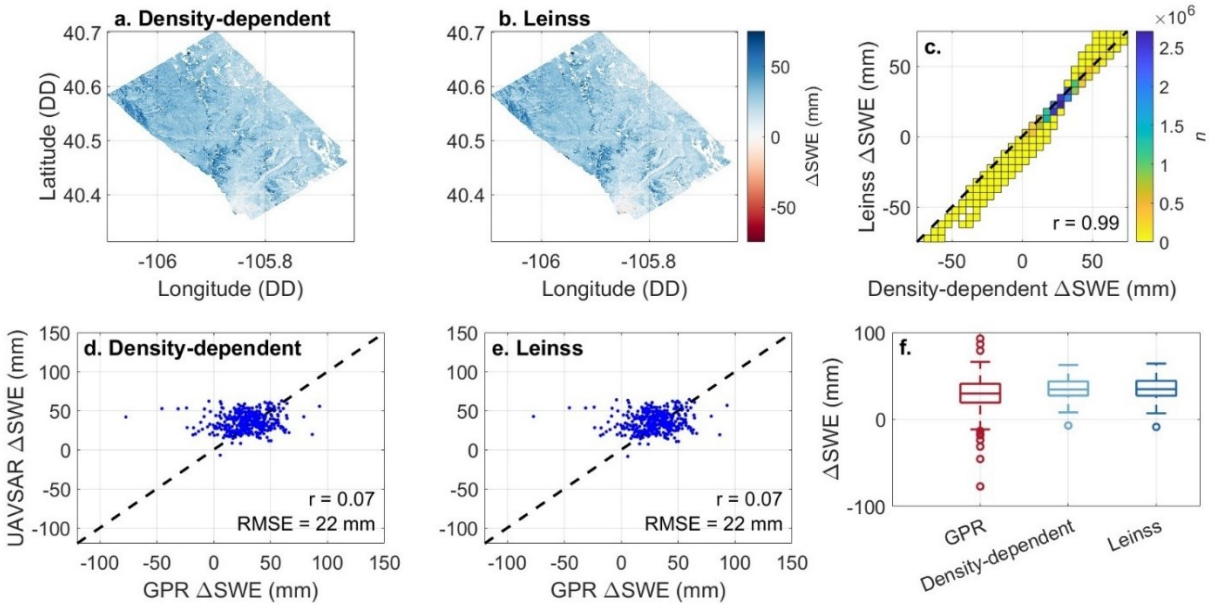

Figure B4: Evaluation of the Leinss et al. (2015) approximation for ΔSWE retrievals from the 16–22 March 2021 HH InSAR pair. ΔSWE retrievals calculated from (a) the density-dependent equation used in Chapter 3 and (b) the Leinss et al. (2015) approximation. (c) Comparison between the density-dependent and Leinss et al. (2015) approximation ΔSWE retrievals. Comparison of GPR ΔSWE retrievals with (d) the density-dependent method and (e) the Leinss et al. (2015) approximation. (f) Box plot distributions of ΔSWE retrievals from the three methods. For plots a–c, the range of ΔSWE is limited to ±75 mm, which represents >99% of the distribution.

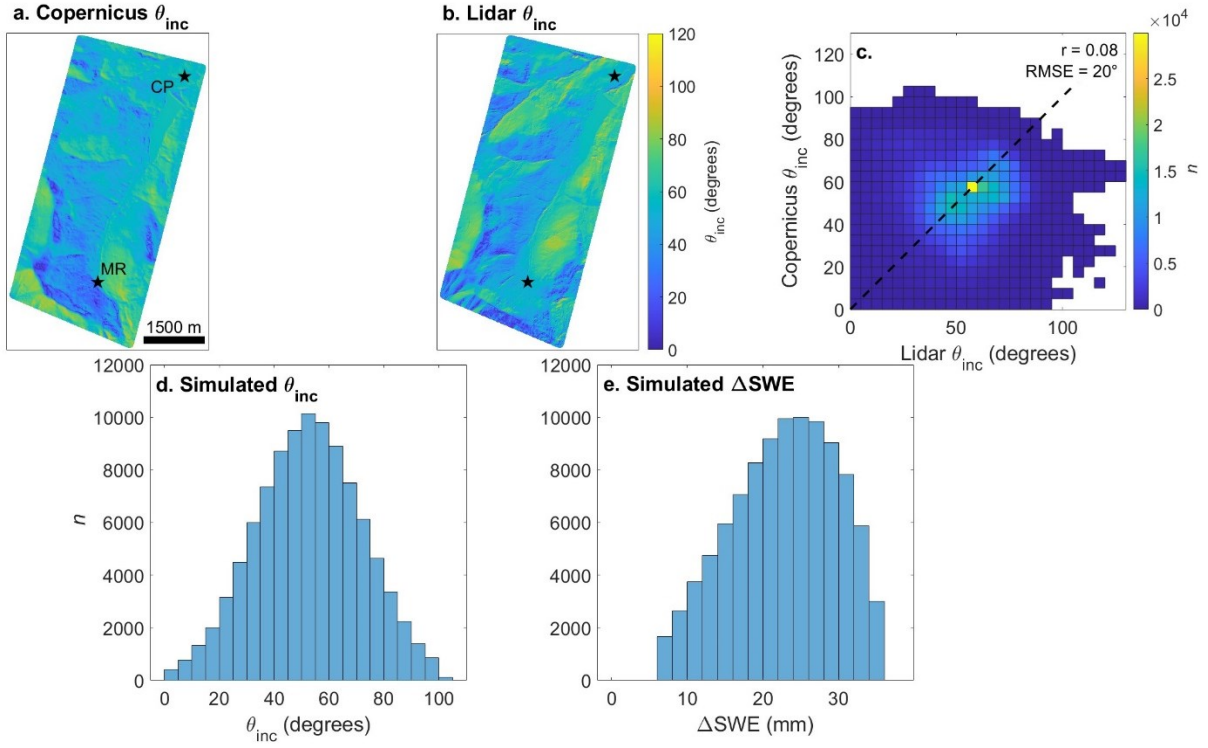

Figure B5: Evaluation of the Copernicus-derived incidence angles. Incidence angles derived from (a) the Copernicus 30 m DEM and (b) the lidar 0.5 m DEM (Adebisi et al., 2022). (c) Two-dimensional histogram showing the comparison between the two sets of incidence angles. Distributions from the Monte Carlo simulation of (d) incidence angles and (e) the corresponding ΔSWE retrievals.

APPENDIX C: CHAPTER 4 SUPPLEMENT

C.1 In Situ Measurements, Sampling Strategy, and Data Organization

C.1.1 Overview of In Situ Measurements

Snow depths and measurements from snow pits were collected at weekly intervals and within a day of UAVSAR flights (Table C2). Snow depth, snow pits, and interval boards were sampled at the Fraser Experimental Forest (FEF) Headquarters (HQ) meteorological site. At the St. Louis Creek field site (StL), snow depths were collected from 20 January to 17 March, although survey dates after 24 February included only a subset of snow depths and no snow pits. The FC field site had less attention, with snow pit and snow depth collections on 3 and 17 March. Measurements of SWE from the Fool Creek SNOTEL station (ID 1186) were incorporated into our analysis to expand the time series at this field site. Snow pit measurements were made following the NASA CLPX and SnowEx protocols (Elder et al., 2009; Mason et al., 2024) and included measurements of depth, density, snow temperature, stratigraphy, and relative permittivity.

A number of radar snow remote sensing experiments have been conducted at the HQ site (e.g., Cline et al., 2008; De Roo et al., 2007; Hardy et al., 2008; Lei et al., 2022; Shah et al., 2017). SnowEx21 used the previously established survey designs. Four short transects (<50 m) and two snow pits were located close to meteorological stations and radar antennae, in a mostly flat and unforested terrain, and with snow depth sampling intervals of ~1 m. Two long transects (240 m and 420 m) and two more snow pits were located in a lodgepole pine (*Pinus contorta)* forest with mixed canopy fractions and deadfall, where snow depth sampling intervals changed from 1 m spacing to 3 m spacing in 30 m increments.

StL and FC were established during the NASA CLPX campaign as two 1000 m x 1000 m (1 km^2) grids (Elder et al., 2009). Snow depths were collected at 100 randomly selected locations within 100 m x 100 m areas nested inside the 1 km^2 grids marked by snow stakes. The StL forest is mainly comprised of lodgepole pine and aspen (*Populus tremuloides*), whereas the FC forest is primarily comprised of Engelmann spruce (*Picea engelmannii*) and subalpine fir (*Abies lasiocarpa*). Both StL and FC contain plots of old growth forests that are 150–300 years old and regenerative growth forests that have grown where previous timber harvesting experiments were conducted in the last 70 years (Alexander et al., 1977; Huckaby & Moir, 1998).

C.1.2 Corrections Applied to In Situ Measurements

Only the HQ field site was visited for the 3 February UAVSAR flight, however, StL was surveyed on 10 February. To increase the number of in situ observations for evaluating the 27 January to 3 February and the 3 February to 23 February InSAR pairs, StL probed depths and snow pit measurements were approximated for 3 February using the 10 February StL survey. These snow depths and SWE measurements were corrected by applying the average snow depth and SWE change between 3 and 10 February observed at HQ.

C.1.3 Organization Scheme for ΔSWE In Situ Datasets

In our study, we devised two categories for in situ SWE measurements: measured SWE and estimated SWE. Measured SWE included SWE from snow pits (the product of depth and bulk density), the SNOTEL station, and the HQ interval board. We estimated SWE from snow depths by multiplying the depth by the average bulk snow density from the field site. After 24 February, only probed depths were collected at StL and we converted StL probed depths to SWE using the bulk snow density from the HQ field site for remaining surveys. HQ and StL have

similar elevations, forest cover fractions (~2700 m, 0.20 FCF), and energy balances, although we note that this method increases the uncertainty of the SWE estimation.

C.2 Processing SAR Datasets

C.2.1 Calculating ΔSWE Retrievals from InSAR

The L-band InSAR method for SWE retrievals was first implemented for a snow-off and snow-on interferometric pair (Guneriussen et al., 2001). However, we have implemented the method for repeat-pass InSAR, which improves the temporal coherence and assumes the component of phase change that relates to snow is primarily at the surface of the snowpack (e.g., ablation, accumulation; Deeb et al., 2011). Thus, this method estimates a change in SWE (ΔSWE) between SAR acquisitions.

Radar is transmissible through snow and the amplitude or phase center is generally the snow-ground interface in unforested areas. The InSAR technique leverages a phase-delay that results from radar velocity attenuation within the snowpack (Guneriussen et al., 2001). As defined by Guneriussen et al. (2001), the phase term for snow (φ_s) is mixed within the total phase recorded in the interferogram:

$$\varphi = \varphi_{flat} + \varphi_{topo} + \varphi_{atm} + \varphi_s + \varphi_{err} \quad \text{Equation C1.}$$

Besides the snow phase term, the total phase change (φ) includes contributions from phase changes that relate to changes in the relative distance between the radar platform and the target on the ground for flat Earth (φ_{flat}) and topography (φ_{topo}), changes in atmospheric precipitable water content or pressure (φ_{atm}; Bevis et al., 1992; Gong et al., 2013), and a phase error term that relates to instrument noise (φ_{err}). UAVSAR removes phase contributions from flat Earth and topography, leaving just the terms for atmosphere, snow, and error. We discuss our atmospheric correction approach in Text C2.2.

After all phase terms have been accounted for, the snow phase term can be used to calculate the change in snow depth (Δd_s):

$$\Delta d_s = -\frac{\lambda \varphi_s}{4\pi} \times \frac{1}{\cos \theta_{inc} - \sqrt{\varepsilon_s - \sin^2 \theta_{inc}}} \quad \text{Equation C2,}$$

where λ is the radar wavelength (~0.238 m), ε_s is the relative permittivity of the snow surface, and θ_{inc} is the radar incidence angle. In dry snow, which is the case considered here (Text C2.3), relative permittivity is primarily determined by the snow density (ρ_s):

$$\varepsilon_s = \left(1 + 0.845 \frac{\rho_s}{1000}\right)^2 \quad \text{Equation C3.}$$

More than 19 equations exist for estimating dry snow relative permittivity from density, but the variation in calculated relative permittivity is limited for low surface densities that were observed at Fraser Experimental Forest (Di Paolo et al., 2020). Regardless, we chose the (Kovacs et al., 1995) equation because it represents the median of the dry snow relative permittivity equations (Di Paolo et al., 2020). Incidence angles were calculated in uavsar_pytools (Hoppinen & Tarricone, 2022) from the UAVSAR look vectors and the lidar 0.5 m x 0.5 m digital terrain models (Adebisi et al., 2023), which was rescaled to the UAVSAR grid. The equation for incidence angles is:

$$\theta_{inc} = (-\hat{n} \cdot \|lkv\|) \quad \text{Equation C4,}$$

where $\hat{n} \cdot \|lkv\|$ is the dot product of the surface normal calculated from the lidar DTM and the magnitude of the look vectors. Finally, ΔSWE is calculated as the product of Δd_s and the average of all snow surface densities (upper 10 cm of the snowpack) collected during surveys.

C.2.2 Atmospheric Correction

The atmospheric phase term results from changes in atmospheric water vapor and pressure between acquisitions (Bevis et al., 1992). Atmospheric corrections are generally categorized as either stratified or turbulent. Stratified delays result from relatively homogenous

changes in atmospheric conditions between acquisitions and manifest in a phase ramp that can often be detected with the eye. Turbulent delays are heterogeneous and can be much more difficult to detect. Atmospheric corrections for airborne InSAR platforms are complicated primarily because the UAVSAR flight altitude (~12.5 km) is below the altitude that most atmospheric models are run for. If performed incorrectly, an InSAR atmospheric correction could lead to artifacts within the ΔSWE retrievals.

Bonnell et al. (2024) evaluated the UAVSAR flight line over the Cameron Pass SnowEx field site (~70 km north) on the same 2021 UAVSAR flight dates and did not detect significant stratified atmospheric artifacts in the interferograms. Thus, we decided that a qualitative assessment to determine the need for atmospheric corrections would suffice. To do so, we reviewed each unwrapped interferogram to determine whether a phase ramp was visible across the UAVSAR swath. A phase ramp was identified for the 3–10 March interval for both flight headings (Figures C1a, C2a).

To remove the phase ramp, we rescaled the data to 25 m and applied a low-pass filter to improve the atmospheric delay signal, which is mixed with the snow signal. Low-pass filtering has been shown to be an effective method for isolating the atmospheric contribution of phase from the UAVSAR platform (Michaelides et al., 2021). Resulting phase values were regressed against the corresponding radar signal path length, calculated as the magnitude of the east/north/up UAVSAR look vectors (Figure C1b, C2b). The regression approach is discussed in Tarricone et al. (2023). Resulting regression slope coefficients have nearly the same sign and magnitude and are statistically significant ($p<0.01$), thus corroborating the presence of atmospheric artifacts. The correction was then applied to the 3–10 March unwrapped interferograms.

C.2.3 Determining Dry/Wet Snowpack Conditions

During the January, February, and 3 March 2021 snow pit surveys, median snow temperatures were below –3 °C (Figure C3) and snow stratigraphy was noted as dry, based on manual observation. Snow pit temperatures warmed to a median of –1 °C by 10 March and snow pit temperatures were nearly isothermal (–0.5 to 0 °C) at HQ on 22 March. On 3 March at HQ, the snow surface was observed to be dry in the morning but moist in the afternoon, based on a manual squeeze test, whereas FC snow pits were described as dry. On 10 March, the stratigraphy at HQ was dry, but a near-surface melt-freeze crust was noted to have increased in thickness by ~4 cm compared to its 0.5 cm thickness in the 3 March HQ snow pits. On 17 March, snow stratigraphy was dry at all HQ and FC snow pits and no evidence of melting was noted in the snow accumulation since 10 March. On 22 March, the morning HQ snow pit, which coincided with the UAVSAR flight noted only dry stratigraphy. However, HQ snow pits observed in the late morning and afternoon noted that the upper 15 cm of the snowpack was moist. Thus, we conclude that the snowpack was most likely dry or had very limited water content (<1 vol. %) during UAVSAR flights (Table C2). However, some melting may have occurred during the 10, 16, or 22 March flights in canopy-captured snow (Figure C4), due to increased exposure to radiative forcings (e.g., Bonner et al., 2022).

C.2.4 Polarimetric Decomposition

We accessed the 052° heading UAVSAR ground projected POLSAR datasets through uavsar_pytools for all 2021 UAVSAR flights. The ground projected datasets contain multi-looked data for the HHHH, HVHV, VVVV, HHHV, HVHV, and HVVV crossproducts (NASA UAVSAR, 2021). Polarimetric parameters were calculated in uavsar_pytools: the mean alpha angle was calculated following Nielsen (2022), whereas entropy and anisotropy were calculated

following the methods of POLSARPRO v6.0. A review of these parameters is provided in Cloude & Pottier (1997).

A 5x5 moving median filter was applied to the mean alpha angle, entropy, and anisotropy datasets for each of the UAVSAR flights to remove speckle. Each polarimetric parameter was composited across the range of dates using the median. Results are shown in Figure S7. Then an image was classified based on the mean alpha angle and entropy following the unsupervised classification technique outlined by Cloude & Pottier (1997). The image suggests that the backscattering falls within one of four different classes: low entropy surface scatter (Zone 9), medium entropy surface scatter (Zone 6), medium entropy vegetation scattering (Zone 5), and medium entropy multiple scattering (Zone 4; Figure S7).

C.3 Calculating Forest Cover Fraction from Lidar Vegetation Heights

Forest cover fraction (FCF) was calculated differently for the UAVSAR vs. in situ comparison and the UAVSAR vs. lidar snow depths comparison. For both comparisons, we used the 0.5 m x 0.5 m lidar vegetation heights (Adebisi et al., 2023). Lidar vegetation heights were converted to a binary canopy cover dataset, using a 2 m threshold to distinguish canopy from brush. For in situ measurements, the FCF was calculated within a 10 m radius to account for the GPS uncertainty of the snow pit and probe locations. For the UAVSAR vs. lidar snow depths comparison, we calculated FCF pixel-wise at the UAVSAR scale (~5 m x ~5 m).

Supplemental Tables

Table C1: List of InSAR SWE retrieval studies and the study site environments.

Authors	Platform Type	Instrument	Frequency	Studied Environment and Location
Guneriussen et al. (2001)	Satellite	ERS 1/2	C-band	Alpine Tundra, Norway
Deeb et al. (2011)	Satellite	ERS-1	C-band	Tundra, Alaska, USA
Leinss et al. (2015)	Tower	SnowScat	X-, Ku-bands	Boreal Forest, Finland
Conde et al. (2019)	Satellite	Sentinel-1	C-band	Boreal Forest, Finland
Marshall et al. (2021)	Airborne	UAVSAR	L-band	Subalpine Meadows, Colorado, USA
Nagler et al. (2022)	Airborne	UAVSAR	C-, L-bands	Alpine, Austria
Ruiz et al. (2022)	Tower	SodSAR	X-, C-, S-, L-bands	Boreal Forest, Finland
Lei et al. (2023)	Satellite	PALSAR-2	L-band	Montane Forests, Colorado, USA
Palomaki & Sproles (2023)	Airborne	UAVSAR	L-band	Prairie, Montana, USA
Tarricone et al. (2023)	Airborne	UAVSAR	L-band	Subalpine Meadows, New Mexico, USA
Bonnell et al. (2024)	Airborne	UAVSAR	L-band	Montane Forests and Subalpine Meadows, Colorado, USA
Hoppinen et al. (2024)	Airborne	UAVSAR	L-band	Montane Forests and Subalpine Meadows, Idaho, USA
Oveisgharan et al. (2024)	Satellite	Sentinel-1	C-band	Montane Forests and Subalpine Meadows, Idaho, USA

Table C2: UAVSAR flights and field survey dates and observations.

UAVSAR Flight Dates	UAVSAR Flight Time (Local)	HQ Survey Dates	HQ Ground Observations	StL Survey Dates	StL Ground Observations	FC Survey Dates	FC Ground Observations
15 January 2021	10:15 (052°)	15 January 2021	1 SP, PD, IB	-	-	-	-
20 January 2021	11:58 (052°)	20 January 2021	2 SP, PD, IB	21 January 2021	2 SP, PD	-	-
-	-	-	-	22 January 2021	4 SP	-	-
27 January 2021	12:12 (052°), 12:25 (233°)	27 January 2021	4 SP, PD, IB	27 January 2021	9 SP, PD	-	-
-	-	-	-	28 January 2021	2 SP	-	-
3 February 2021	11:11 (052°), 11:25 (233°)	3 February 2021	2 SP, PD, IB	10 February 2021	5 SP, PD	-	-
23 February 2021	10:03 (052°)	24 February 2021	4 SP, PD, IB	24 February 2021	9 SP, PD	-	-
3 March 2021	9:34 (052°), 9:47 (233°)	3 March 2021	4 SP, PD, IB	4 March 2021	PD	3 March 2021	8 SP, PD
10 March 2021	9:05 (052°), 9:16 (233°)	10 March 2021	2 SP, PD, IB	11 March 2021	PD	-	-
16 March 2021	15:23 (052°), 15:36 (233°)	17 March 2021	2 SP, PD, IB	17 March 2021	PD	17 March 2021	8 SP, PD
22 March 2021	9:00 (052°), 9:12 (233°)	22 March 2021	4 SP, PD, IB	-	-	-	-

Table C3: Mean UAVSAR ΔSWE ± 1 standard deviation in mm over Fraser Experimental Forest.

Date Interval	052° HH	233° HH	052° HV	233° HV	052° VH	233° VH	052° VV	233° VV
15–20 Jan	17 ± 8	-	17 ± 8	-	18 ± 9	-	17 ± 8	-
20–27 Jan	5 ± 7	-	-	-	7 ± 8	-	5 ± 7	-
27 Jan – 3 Feb	15 ± 10	16 ± 9	16 ± 10	17 ± 9	16 ± 10	16 ± 9	13 ± 9	15 ± 8
3–23 Feb	-	-	-	-	46 ± 17	-	-	-
23 Feb – 3 Mar	10 ± 12	-	12 ± 13	-	11 ± 13	-	13 ± 12	-
3–10 Mar	–4 ± 11	1 ± 11	–6 ± 11	4 ± 11	–3 ± 11	4 ± 11	0 ± 10	3 ± 10
10–16 Mar	36 ± 13	32 ± 11	33 ± 13	31 ± 11	34 ± 15	31 ± 11	34 ± 14	31 ± 11
16–22 Mar	12 ± 11	11 ± 8	18 ± 12	20 ± 10	17 ± 11	22 ± 10	14 ± 11	17 ± 9

Table C4: Statistics for In Situ vs. UAVSAR 052° heading. StL in situ observations used observations collected on 10 February that were adjusted to 3 February. FC observations spanned two InSAR pairs and statistics were included for the 10–16 March pair because this interval saw the larger SWE change.

	HH			HV			VH			VV		
InSAR Pair	**n**	**RMSE (mm)**	**r**	**n**	**RMSE (mm)**	**r**	**n**	**RMSE (mm)**	**r**	**n**	**RMSE (mm)**	**r**
15–20 January 2021	16	9	0.19	16	7	–0.36	16	8	–0.29	16	11	0.23
20–27 January 2021	139	8	0.02	-	-	-	137	8	0.10	139	8	0.05
27 January – 3 February 2021	231	14	–0.02	231	14	0.07	230	14	0.02	231	14	0.08
3–23 February 2021	-	-	-	-	-	-	117	21	–0.07	-	-	-
23 February – 3 March 2021	232	12	0.18	228	13	0.07	230	13	0.03	230	11	0.03
3–10 March 2021	171	18	–0.13	156	17	–0.07	149	17	–0.15	175	18	–0.07
10–16 March 2021	272	30	–0.32	274	30	–0.26	272	28	–0.10	275	28	–0.10
16–22 March 2021	159	16	–0.07	140	18	–0.09	140	17	–0.01	161	17	0.03
Overall	1220	19	0.52	1045	20	0.43	1291	19	0.54	1227	18	0.53

Table C5: Statistics for In Situ vs. UAVSAR 233° heading. FC observations spanned two InSAR pairs and statistics were included for the 10–16 March pair because this interval saw the larger SWE change.

	HH			HV			VH			VV		
InSAR Pair	**n**	**RMSE (mm)**	**r**	**n**	**RMSE (mm)**	**r**	**n**	**RMSE (mm)**	**r**	**n**	**RMSE (mm)**	**r**
27 January – 3 February 2021	232	16	0.06	231	17	0.06	231	17	0.04	232	16	0.06
3–10 March 2021	176	19	–0.15	176	20	–0.14	176	20	–0.13	176	19	–0.19
10–16 March 2021	275	27	–0.04	277	26	0.19	276	26	0.18	277	26	0.20
16–22 March 2021	163	15	–0.06	162	21	0.03	163	23	0.06	163	17	0.03
Overall	846	21	0.47	846	22	0.45	846	22	0.42	848	20	0.52

Supplemental Figures

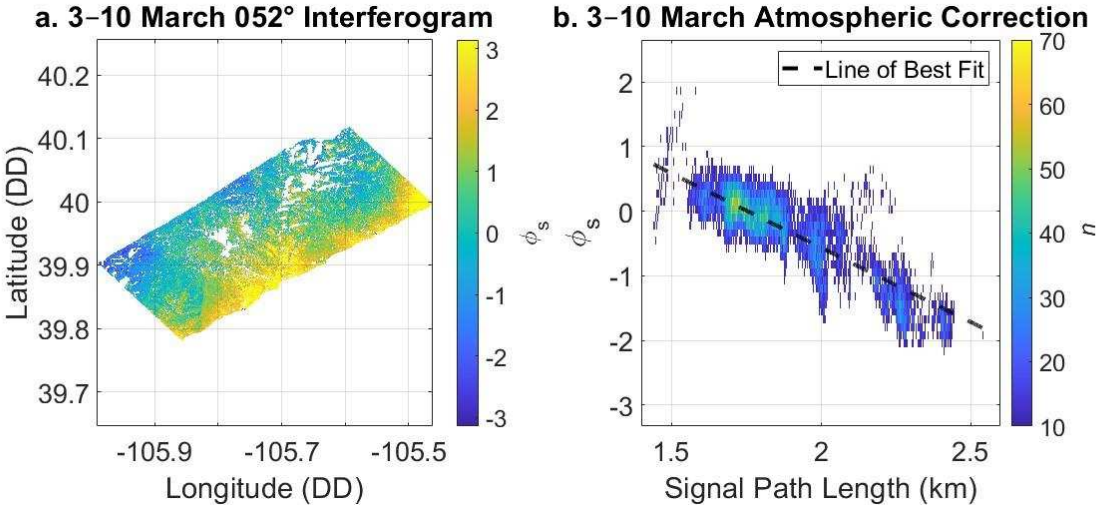

Figure C1: (a) 3–10 March unwrapped interferogram displaying a phase ramp. Color scheme is limited to ±π. (b) Linear regression performed after data filtering. Regression equation has a r^2 of 0.67.

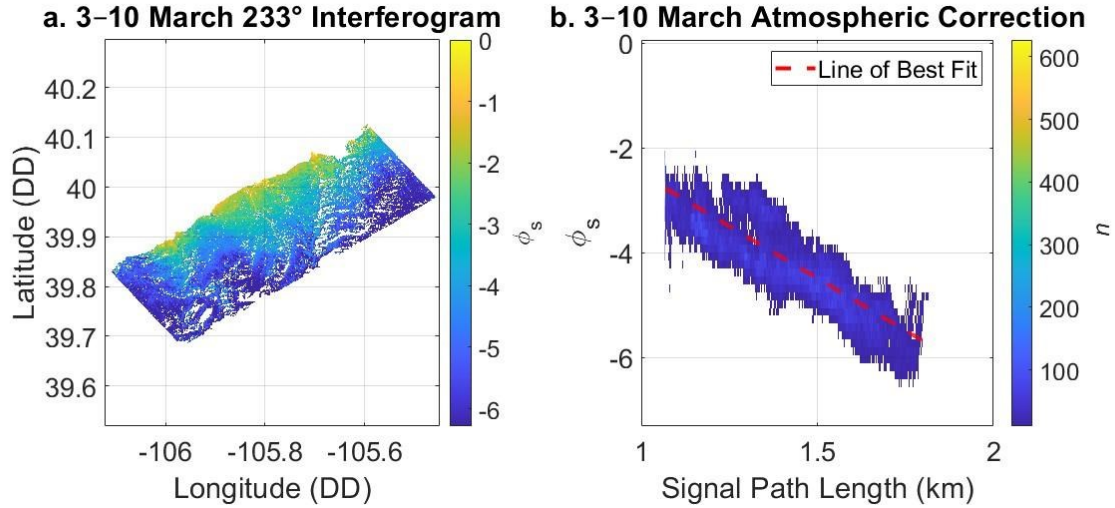

Figure C2: (a) 3–10 March unwrapped interferogram from the 233° heading, displaying a phase ramp from near to far range. Color scheme is limited to –2π to 0. (b) Linear regression performed after data filtering. Regression equation has a r^2 of 0.73.

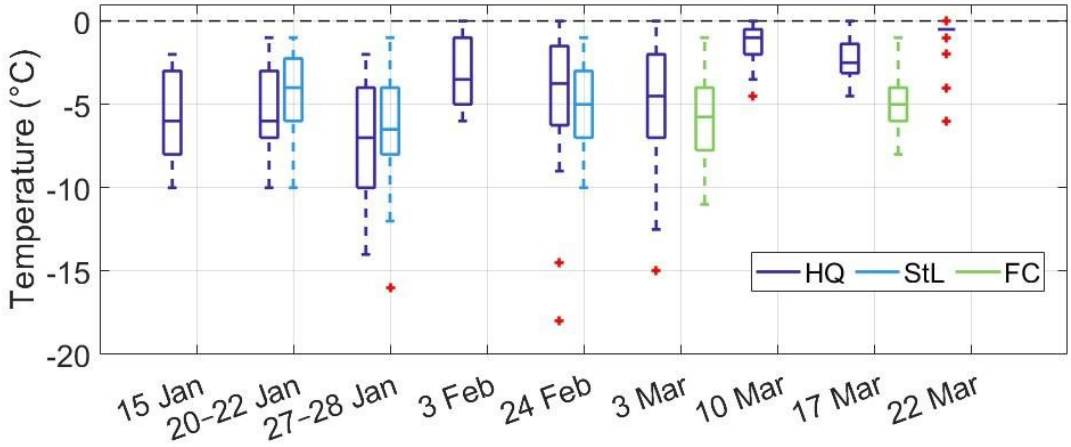

Figure C3: Box plot distributions of snow pit temperatures collected at the Headquarters (HQ), St. Louis Creek (StL), and Fool Creek (FC) field sites. For the 20 January, 27 January, 23 February, and 16 March UAVSAR flights, snow pit observations took place either on a range of dates around the flight date (e.g., 20–22 January) or the day after the flight. Note, surface temperatures tend to be cooler, whereas temperatures near the snow-ground interface tend to be warming.

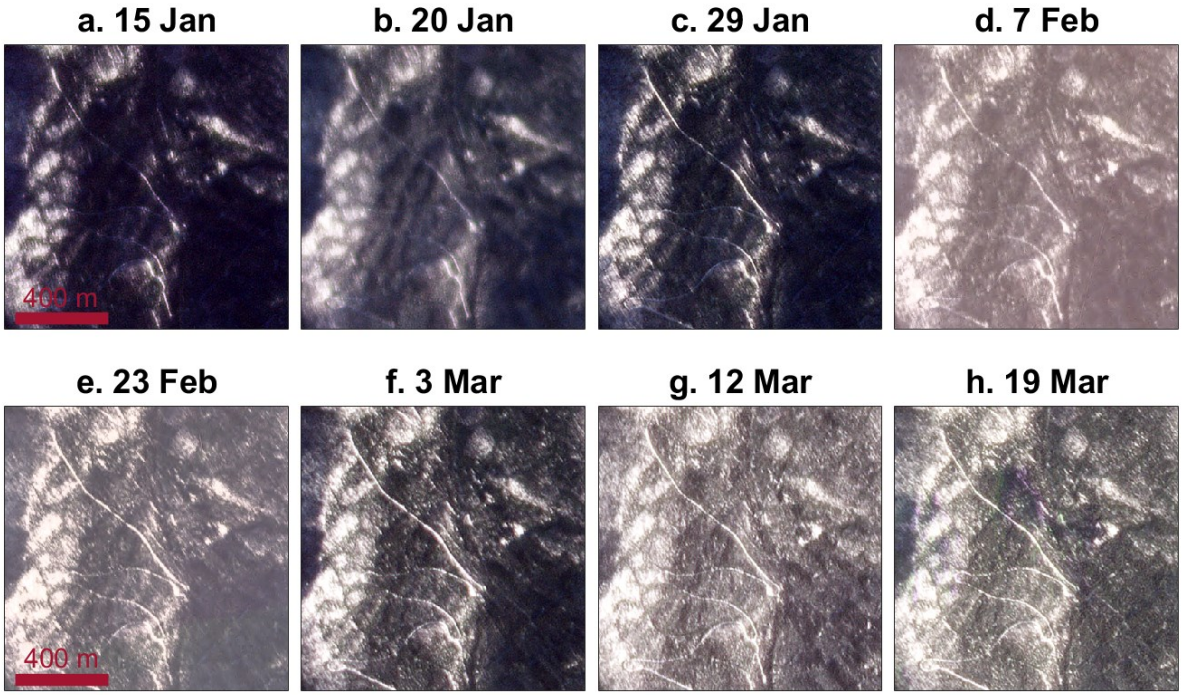

Figure C4: PlanetScope satellite imagery (Planet Labs PBC, 2021) of the Fool Creek field site acquired on or near UAVSAR acquisition dates. Surveyors observed snow in the trees on 10 February, 10 March, 17 March, and 22 March, 2021.

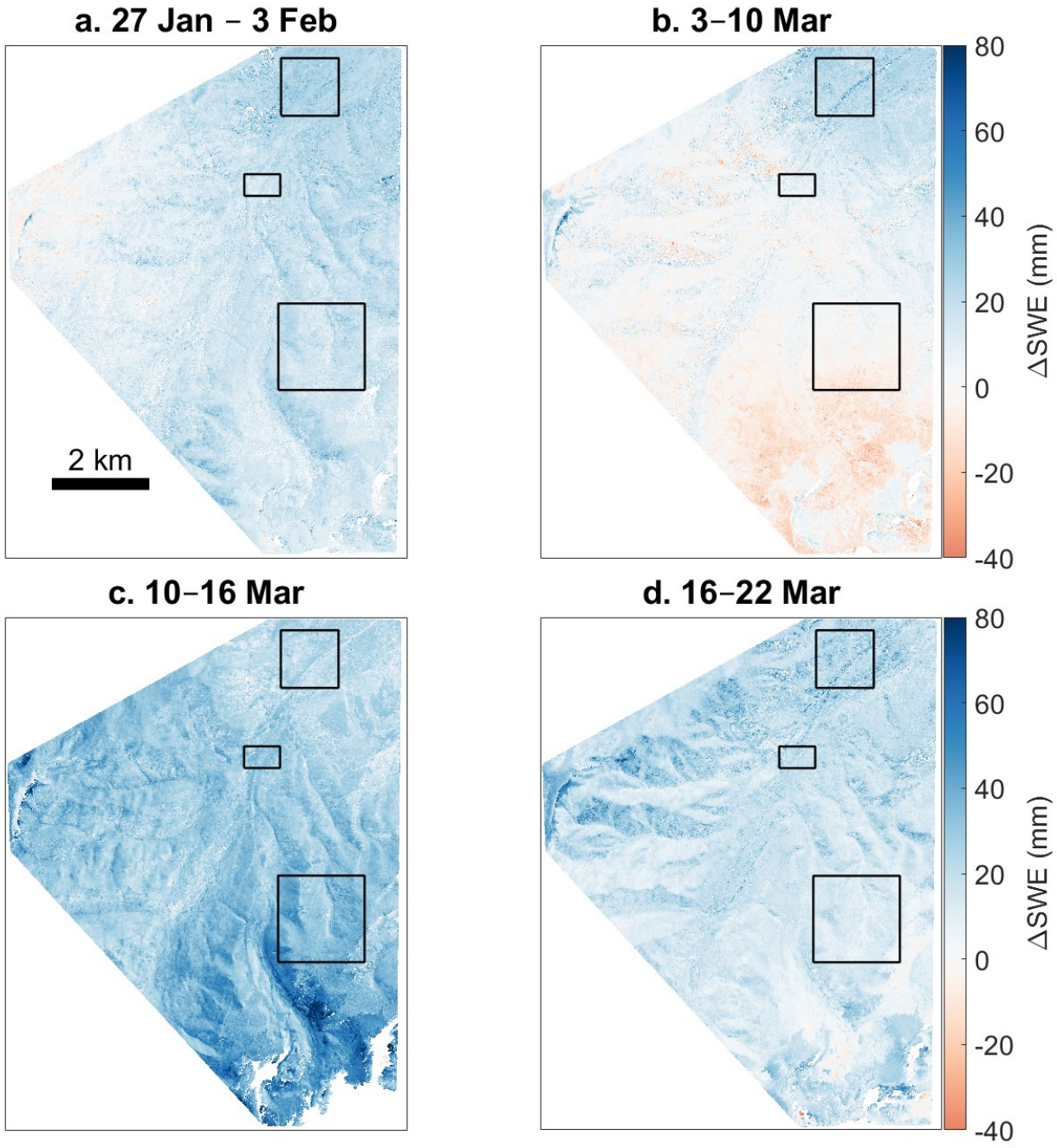

Figure C5: UAVSAR ΔSWE retrievals at the study site for each 233° InSAR pair. Field sites are shown with boxes. White denotes missing data in the figure due to issues with phase unwrapping.

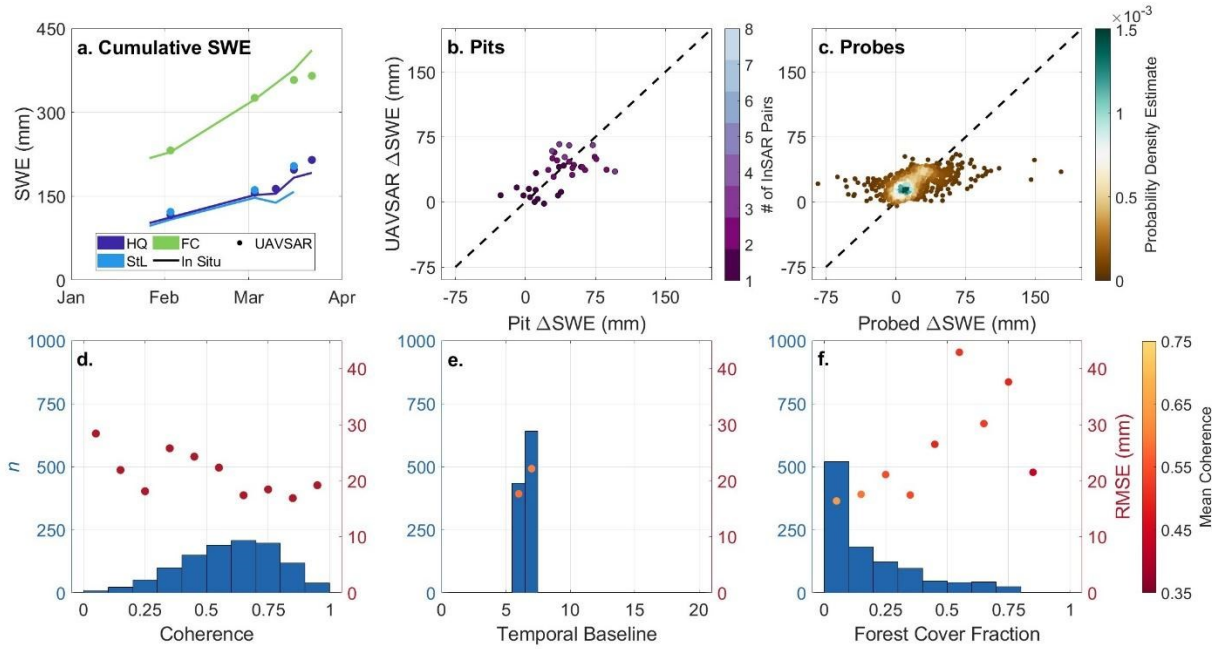

Figure C6: In situ evaluation of the 233° heading. (a) Mean SWE measured/estimated from snow pits, depth probes, and SNOTEL measurements compared with mean UAVSAR retrieved SWE for each field site. (b) UAVSAR ΔSWE evaluated against snow pit and SNOTEL ΔSWE measurements with points colored by the number of InSAR pairs that were summed for each comparison. (c) UAVSAR ΔSWE evaluated against ΔSWE estimated from probed depth measurements. Histograms and RMSE for each histogram bin for (d) coherence, (e) temporal baseline, and (f) forest cover fraction. Points on e and f are colored by the mean coherence calculated within the bin.

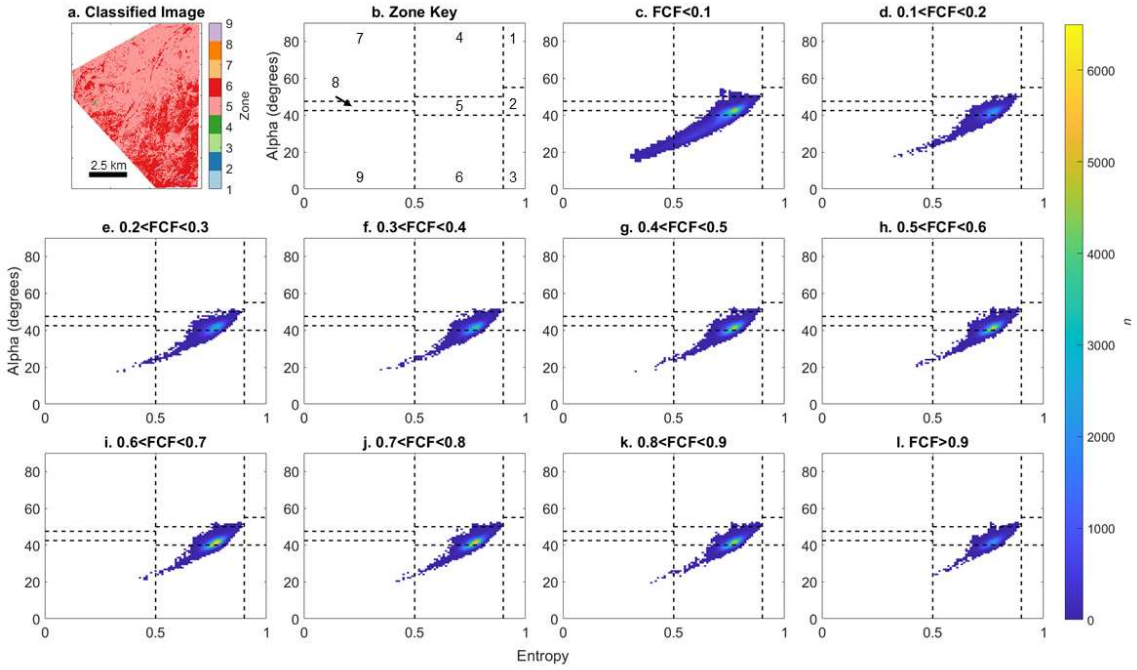

Figure C7: Polarimetric decomposition analysis. (a) FEF L-band SAR classification following Cloude & Pottier (1997). (b) Classification zones from Cloude & Pottier (1997) based on Alpha-Entropy characteristics. (c–l) Two-dimensional histogram plots of Alpha-Entropy distributions binned by FCF for UAVSAR incidence angles of 50–70°. Distributions fall entirely within zones 4, 5, 6, and 9. For reference, Zone 4 indicates radar double bounce (e.g., the signal reflects from the ground and then from a tree), Zone 5 indicates volume scattering (e.g., from vegetation), Zone 6 indicates a stronger ground reflection with some interference from the canopy, and Zone 9 indicates smooth land surfaces, where smooth is relative to the radar wavelength (Cloude & Pottier, 1997).

APPENDIX D: DATA AVAILABILITY

D.1 Chapter 2 and Appendix A Datasets

The National Snow and Ice Data Center has archived ground-penetrating radar datasets for Grand Mesa (Webb et al., 2019; https://doi.org/10.5067/G21LGCNLFSC5) and Cameron Pass (McGrath et al., 2021; https://doi.org/10.5067/U4Q3X27BMRR4; Bonnell et al., 2022; https://doi.org/10.5067/SRWGLYCB6ZC4), Airborne Snow Observatory lidar datasets (Painter, 2018; https://doi.org/10.5067/KIE9QNVG7HP0), snow pit measurements for Grand Mesa (Elder et al., 2018; https://doi.org/10.5067/Q0310G1XULZS) and Cameron Pass (Mason et al., 2023, 2024) and derived relative permittivity and snow density datasets (Bonnell et al., 2024; https://doi.org/10.5067/W0EJNWUZBYSL). Terrestrial lidar scan point clouds are archived with UNAVCO, Inc. (Williams, 2021; https://tls.unavco.org/projects/U-077/PS01/). Cameron Pass uncrewed aerial vehicle (UAV) lidar point cloud and bare earth digital elevation model and Ranch Creek UAV lidar point clouds and snow depth raster are archived with the U.S. Geological Survey (Bauer et al., 2023). Ranch Creek GPR surveys are archived at HydroShare (Bonnell & McGrath, 2023; https://doi.org/10.4211/hs.6f39721f1643428f84997f09ef75e2f8). SNOTEL station data is available online (USDA Natural Resources Conservation Service, 2023). Ranch Creek weather station data is available online (U.S. Geological Survey, 2023). iSnobal and AWSM model code can be downloaded from https://github.com/USDA-ARS-NWRC/awsm/tree/master.

D.2 Chapter 3 and Appendix B Datasets

The National Snow and Ice Data Center has archived ground-penetrating radar datasets (Bonnell et al., 2022; McGrath et al., 2021) and snow pit measurements (Mason et al., 2023,

2024). Probed snow depths are under review at the National Snow and Ice Data Center. Weather station data is publicly available online for the following stations: Joe Wright SNOTEL (https://wcc.sc.egov.usda.gov/nwcc/site?sitenum=551), Lake Irene SNOTEL (https://wcc.sc.egov.usda.gov/nwcc/site?sitenum=565), Willow Park SNOTEL (https://wcc.sc.egov.usda.gov/nwcc/site?sitenum=870), Phantom Valley SNOTEL (https://wcc.sc.egov.usda.gov/nwcc/site?sitenum=688), and CPWS (Kampf et al., 2022). Terrestrial lidar point clouds are available at UNAVCO Inc. (Williams, 2021). NASA UAVSAR datasets are available from UAVSAR or the Alaska Satellite Facility Distributed Active Archive Center (NASA UAVSAR, 2020, 2021). The Copernicus 30 m DEM, Copernicus Global 100 m Land Cover Dataset, and Sentinel-2 Level 2A imagery were accessed via Google Earth Engine (Gorelick et al., 2017). UAVSAR ΔSWE retrievals are archived with Dryad (https://doi.org/10.5061/dryad.mkkwh7189).

D.3 Chapter 4 and Appendix C Datasets

The National Snow and Ice Data Center has archived the following datasets: snow pits (Mason et al., 2023, 2024), lidar DEM (Adebisi et al., 2022a), lidar snow depths (Adebisi et al., 2022b), and lidar vegetation heights (Adebisi et al., 2022c). Probed snow depths are under review at the National Snow and Ice Data Center. NASA UAVSAR datasets are available from UAVSAR or the Alaska Satellite Facility Distributed Active Archive Center (NASA UAVSAR, 2021). UAVSAR ΔSWE retrievals are archived with Dryad (https://doi.org/10.5061/dryad.x3ffbg7tg).